EMPA20090748

Diss. ETH N° 18678

CHARACTERIZATION AND APPLICATION OF ACTIVE FIBER COMPOSITES

A dissertation submitted to

ETH ZURICH

for the degree of

Doctor of Sciences

presented by

MARCEL BIRCHMEIER

Dipl. Bau-Ing. ETH

born June 14, 1976

citizen of Rapperswil/SG

accepted on the recommendation of

Prof. Dr. Jürg Dual, examiner
Dr. Andreas J. Brunner, co-examiner
Dr. Daniel Gsell, co-examiner

2009

Acknowledgements

This work was carried out during my employment as a research assistant at the Laboratory of Mechanical Systems Engineering of the Empa Dübendorf and at the Institute of Mechanical Systems of the ETH Zürich. I would like to thank everyone who contributed in one form or another to this thesis, in particular:

Prof. Dr. J. Dual, my supervisor, for his encouragement in guiding my research and for providing a positive research environment.

Dr. A. J. Brunner and Dr. D. Gsell, my co-examiners, for reviewing this thesis and for their support and the interesting and helpful discussions.

Markus Juon and Patrick Rebecchi for writing their Semesterarbeiten and Tobias Lieb for doing an internship within the scope of my research project and thus contributing to this thesis.

Dr. Michel Barbezat, Lorenzo de Boni, Christian Dürager, Dr. Rolf Paradies, Marcel Rees, Kurt Ruf, Dr. Sandy Schubert, and Dr. Giovanni Terrasi, from Empa, for providing support in various kind and contributing to a positive working environment.

Laurent Aebi, Jürg Bryner, Andrea Cambruzzi, Dr. Stephan Kaufmann, Dr. Jacqueline Vollmann, and Heinz Widmer, from the Institute of Mechanical Systems of the ETH Zürich, for their theoretical and technical support as well as all other members of the Institute for creating a helpful and friendly atmosphere.

Roman Gätzi for providing the sandwich plates for the experimental part.

Barbara Freigang for checking the spelling.

And finally, Claudia Züger for being patient and for supporting and motivating me throughout the entire process.

Contents

Abstract **v**

Zusammenfassung **vii**

List of Symbols and Abbreviations **xi**

List of Figures **xiv**

List of Tables **xvii**

1 Introduction **1**
1.1 Motivation . . . 1
1.2 Aim of the Project . . . 3
1.3 Outline . . . 3

2 General Aspects **5**
2.1 Structural Health Monitoring . . . 5
2.2 Acoustic Non-Destructive Testing Methods . . . 6
2.3 Elastic Waves in Plates . . . 8
2.4 Piezoelectric Transducers . . . 12
2.4.1 Constitutive Relations . . . 12
2.4.2 Different Types of Transducers . . . 13
2.4.3 Active Fiber Composite . . . 16

3 Characterization of AFCs **19**
3.1 Introductory Remarks . . . 19
3.1.1 Concept . . . 19
3.1.2 Previous Work . . . 20
3.1.3 Transfer Function and Coherence . . . 24
3.2 Procedure for Simulations and Experiments . . . 25
3.2.1 Data Acquisition . . . 25
3.2.2 Separation of the Wave Modes . . . 27
3.2.3 Excitation Signals . . . 28
3.2.4 Data Handling . . . 28
3.3 Numerical Modelling . . . 30

3.3.1 Approach . . . 30
3.3.2 Assumptions . . . 30
3.3.3 Governing Equations . . . 32
3.3.4 Numerical Implementation . . . 35
3.3.5 Combination of the 2D and 3D Model . . . 39
3.3.6 Examples of the Simulations . . . 40
3.3.7 Sensitivity Analysis . . . 45
3.4 Experimental Investigation . . . 47
3.4.1 Materials . . . 47
3.4.2 Setup and Measurement . . . 48
3.4.3 Coherence Analysis . . . 53
3.5 Results and Discussion . . . 55
3.5.1 AFC as Emitter . . . 55
3.5.2 AFC as Receiver . . . 69
3.6 Summary . . . 77

4 Application of AFCs for Damage Detection 79
4.1 Introductory Remarks . . . 79
4.2 Methods and Experimental Setup . . . 80
4.2.1 Guided Wave Based Method . . . 80
4.2.2 Electro-Mechanical Impedance Method . . . 83
4.3 Materials . . . 85
4.3.1 Test Specimen . . . 85
4.3.2 Transducers . . . 86
4.4 Preliminary Investigations on a Sandwich Plate . . . 86
4.4.1 Wave Propagation . . . 87
4.4.2 Damage Detection . . . 89
4.4.3 Reversible Delamination . . . 96
4.4.4 Conclusion . . . 98
4.5 Final Experiment . . . 99
4.5.1 Arrangement and Measurement . . . 99
4.5.2 Results and Discussion . . . 100
4.6 Summary . . . 108

5 Conclusions and Outlook 109
5.1 Characterization of AFC . . . 109
5.2 Application of AFC . . . 110
5.3 Outlook . . . 112

A Material Parameters 115

B Overview of Performed Investigations 117

C Additional Figures from the Characterization **121**
C.1 AFC as emitter 121
C.2 AFC as receiver 126

D Additional Figures from the Application **127**
D.1 Transfer Function of an MFC 127
D.2 Time signals excited and measured with MFCs and disc transducers . 128
D.3 Transfer functions from transducer to transducer 132

Bibliography **135**

Curriculum Vitae **145**

List of Publications **147**

Abstract

Active fiber composites (AFCs) consist of one layer of piezoelectric ceramic fibers which are embedded in an epoxy matrix and sandwiched between two sets of interdigitated electrodes (IDE). The thin planar size and the conformability to even biaxially curved surfaces make AFCs suitable as transducer elements for structural health monitoring (SHM) applications with non-destructive testing methods (NDT) based on wave propagation. In the present work the transfer behavior of AFCs as emitter and receiver of transient elastic waves in isotropic plate-like structures is characterized. This is essential for conception and optimization of the AFC for specific applications. Further, the suitability of AFCs for damage detection in a model structure with two different NDT methods is demonstrated experimentally. Damage detection constitutes the first step of the damage identification process for a SHM system with AFCs.

For the characterization of the AFC, transfer functions defined as the ratio between the output and the input of a linear system in the frequency domain are numerically and experimentally determined for both the emitter and receiver separately. The system to be considered is an aluminum plate with a surface bonded AFC. If the AFC is used as emitter, the input corresponds to the electric voltage signal used for excitation and the output is the resulting surface velocity at specific points around the emitter. If it is used as receiver, the surface velocity of the incident wave from different directions and the resulting electric voltage at the electrodes of the AFC correspond to the input and output signals, respectively. Due to the anisotropic material behavior of the AFC caused by the unidirectionally aligned fibers and the IDE, the transfer functions differ depending on the direction of the excited or incident wave relative to the fiber direction of the AFC.

To investigate the dynamic behavior, the system consisting of the plate and the surface mounted AFC is modelled numerically according to the finite-difference time domain method. A two-dimensional (2D) plane strain model simulates the wave propagation in a cross section through the AFC and the plate at the plane of symmetry in fiber direction of the AFC. The model takes the electro-mechanical coupling of the piezoelectric material into account which allows for simulating the emitter and receiver behavior of the AFC. A three-dimensional (3D) model then considers only the plate itself but allows for investigating the wave propagation in any direction. The waves are excited at the surface of the plate by applying the same mechanical stresses as obtained between the AFC and the plate within the 2D model. Hence, the fully 3D wave field excited by a surface bonded AFC can be

simulated. The 3D model is used only for the investigation of the AFC as emitter.

In order to validate the results of the simulations, experiments are performed. The wave field at the surface of the plate excited or measured with the AFC is observed free of contact by using a heterodyne laser interferometer. AFCs with different lengths are applied. For both, the simulation and the experiment, transfer functions are determined for the two fundamental Lamb wave modes separately. The numerical calculations qualitatively and quantitatively agree well with the measurements.

The investigation shows that the transfer behavior of the AFC is highly frequency and directionally dependent. There are minima and maxima in the transfer functions depending on the relation between the length of the AFC and the length of the wave propagating in the plate. The latter is defined by the frequency as well as the wave propagation characteristic of the structure. The emitting and receiving capabilities are strongest in the fiber direction of the AFC. The reason for this is on the one hand the relation between the AFC's width and the wavelength. The wider the AFC compared to the wavelength, the more pronounced the directionality. On the other hand, the anisotropic material behavior of the AFC enhances this effect, and it is further responsible for the excitation of not only the two fundamental Lamb wave modes but also of shear horizontal waves.

The experiments for the damage detection are performed on an aluminum-hardfoam sandwich plate. First, the wave propagation in the sandwich plate and the influence of delaminations between face sheet and core on the waves are investigated. Further, a method is developed which allows for producing artificial and reversible delaminations and hence for switching between the undamaged and damaged states with reproducible results. This is necessary in order to investigate the performance of the transducer elements without having the influence of uncontrolable and non reproducible damages. For these experiments piezoelectric ceramic transducers are applied instead of AFCs.

The final experiment is then carried out with AFCs which are shortened to a specific length in order to optimize their transfer behavior. The two approaches for the delamination detection are the guided wave based method and the electromechanical impedance method. While the former method uses short wave pulses, the latter is based on harmonic vibrations. For both methods, the same AFCs are used as transducer elements but in different frequency ranges. Compared to the undamaged state, significant changes in the measured signals due to the artificial delamination can be obtained for both methods. Hence, AFCs are suitable for damage detection with two different methods which is of advantage in particular in SHM applications. The investigation shows that for the application of AFCs it is important to take the coupled transfer behavior of the surface bonded AFC into account in order to obtain useful and interpretable results.

Zusammenfassung

Aktive Faserverbund-Elemente (AFCs, aus dem Englischen 'Active Fiber Composites') bestehen aus einer Schicht piezoelektrischer Keramikfasern, die in eine Epoxid Matrix eingebettet und zwischen zwei Fingerelektrodenpaare platziert ist. AFCs eignen sich dank ihrer geringen Dicke und ihrer Biegbarkeit als Aktor- und Sensorelemente für die permanente Zustandsüberwachung von Strukturen (SHM, aus dem Englischen 'Structural Health Monitoring') mittels wellenbasierten zerstörungsfreien Prüfverfahren. Im ersten Teil der vorliegenden Arbeit wird das dynamische Übertragungsverhalten von oberflächenapplizierten AFCs als Sender und Empfänger von elastischen Wellen charakterisiert, die sich in einer isotropen Plattenstruktur ausbreiten. Diese Charakterisierung ist wichtig im Hinblick auf die Auslegung und Optimierung der AFCs für spezifische Anwendungen. Im zweiten Teil der Arbeit wird die Anwendbarkeit der AFCs zur Schadenserkennung in einer Modellstruktur experimentell aufgezeigt. Es werden zwei verschiedene zerstörungsfreie Prüfverfahren eingesetzt und bei beiden Verfahren übernehmen dieselben AFCs die Funktion der Sender und Empfänger. Das Erkennen einer Schädigung der Struktur entspricht der ersten Stufe im Schadensidentifizierungsprozess in einem SHM System.

Zur Charakterisierung werden Übertragungsfunktionen für den AFC sowohl als Sender wie auch als Empfänger von Wellen in einem numerischen Modell und im Experiment bestimmt. Die Übertragungsfunktion beschreibt das Verhältnis zwischen Ausgangs- und Eingangssignal eines linearen Systems im Frequenzbereich. Das hier untersuchte System besteht aus einer Aluminiumplatte mit einem oberflächenapplizierten, fest aufgeklebten AFC. Wird der AFC als Sender gebraucht, dann entspricht die elektrische Spannungsanregung dem Eingangssignal und das Ausgangssignal wird definiert als die resultierende Oberflächengeschwindigkeit an spezifischen Punkten um den AFC herum. Wird der AFC hingegen als Empfänger eingesetzt, so entspricht die Oberflächengeschwindigkeit der in einem beliebigen Winkel zur AFC-Faserrichtung einfallenden Welle dem Eingangssignal und die resultierende elektrische Spannung über den Elektroden des AFCs dem Ausgangssignal. Wegen dem anisotropen Materialverhalten des AFCs, verursacht durch die ausgerichteten Fasern und der Anwendung von Fingerelektroden, ergeben sich unterschiedliche Übertragungsfunktionen je nach dem, wo die resultierende Oberflächengeschwindigkeit gemessen wird, respektive, aus welcher Richtung die vom AFC zu detektierende Welle eintrifft.

Um das dynamische Verhalten zu untersuchen, wird das System bestehend aus Platte und angekoppeltem AFC mit Hilfe der Finiten-Differenzen Methode nu-

merisch modelliert. In einem zweidimensionalen (2D) Modell wird die Wellenausbreitung im ebenen Dehnungszustand in der Schnittebene quer zur Plattenebene in Richtung der Symmetrieachse in Faserrichtung des AFC simuliert. Dabei wird die elektro-mechanische Kopplung über den Piezoeffekt mitberücksichtigt, was die Simulation des AFC als Sender wie auch als Empfänger ermöglicht. Mit einem dreidimensionalen (3D) Modell, das nur die Platte ohne AFC beschreibt, wird dann die Wellenausbreitung in beliebigen Richtungen simuliert. Um die Wellen im 3D Modell anzuregen, werden dieselben mechanischen Spannungen an der Oberfläche der Platte aufgebracht wie sie zuvor im 2D Modell zwischen AFC und Platte berechnet und aufgezeichnet wurden. Auf diese Weise kann das komplette 3D Wellenfeld entsprechend einer Anregung mit dem AFC simuliert werden. Das 3D Modell wird nur für die Untersuchung des AFC als Sender verwendet.

Die Resultate der Simulation werden anhand von experimentell gewonnenen Daten überprüft. Dazu wird das vom AFC angeregte oder zu messende Wellenfeld auf der Plattenoberfläche mit einem Laserinterferometer berührungslos detektiert. Es werden AFCs mit verschiedenen Längen untersucht und die experimentell bestimmten Übertragungsfunktionen mit denen aus der Simulation verglichen. Dabei werden die beiden Lamb Wellenmoden separat betrachtet. Der Vergleich zwischen Simulation und Experiment zeigt sowohl eine qualitativ wie auch quantitativ gute Übereinstimmung.

Aus der Untersuchung folgt, dass das Übertragungsverhalten des AFCs stark frequenz- und richtungsabhängig ist. Je nach Verhältnis zwischen den Längen des AFCs und der in der Platte laufenden Welle ergeben sich Minima und Maxima in der Übertragungsfunktion. Die Wellenlänge wird dabei durch die Dicke und die Materialeigenschaften der Platte sowie durch die Frequenz bestimmt. Das Abstrahl- und Empfangsvermögen ist am stärksten in der Faserrichtung des AFCs. Auf der einen Seite kann dies mit dem Verhältnis zwischen der Breite des AFCs und wiederum der Wellenlänge erklärt werden: Je breiter der AFC im Vergleich zur Wellenlänge, desto stärker ausgeprägt ist die Richtungsabhängigkeit. Auf der anderen Seite ist auch das anisotrope Materialverhalten des AFC für diesen Effekt verantwortlich. Letzteres führt auch dazu, dass neben den beiden Lamb Wellenmoden auch ein Scherhorizontalwellenmode angeregt wird.

Die Modellversuche zur Schadenserkennung werden an Aluminium-Hardschaum Sandwichplatten durchgeführt. Zuerst wird die Wellenausbreitung in einer solchen Platte und der Einfluss von Ablösungen zwischen Deckschicht und Kern auf die sich ausbreitenden Wellen untersucht. Weiter wird eine Methode vorgestellt, mit der sich solche Schädigungen im Experiment genügend realitätsnah künstlich erzeugen lassen. Dies erlaubt mit reproduzierbaren Resultaten zwischen dem ungeschädigten und dem geschädigten Zustand der Struktur hin und her zu wechseln und somit das Verhalten der Aktor- und Sensorelemente ohne den Einfluss von unkontrollierbaren Schädigungen zu untersuchen. Für diese Experimente werden piezoelektrische Keramikplättchen anstelle von AFCs verwendet.

Für das abschliessende Experiment sind, mit Hilfe der Erkenntnisse aus der Charakterisierung, AFCs auf eine spezifische Länge gekürzt worden, um ihr Über-

tragungsverhalten für den vorgesehenen Einsatz zu optimieren. Zur Erkennung einer Schädigung, hier eine künstlich produzierte Ablösung, wird das Lambwellen-Verfahren und das elektro-mechanische Impedanz-Verfahren angewendet. Ersteres basiert auf der Ausbreitung von kurzzeitigen Wellenpulsen, letzteres auf harmonischen Schwingungen. Für beide Verfahren kommen die gleichen oberflächenapplizierten AFCs, jedoch in einem anderen Frequenzbereich, zum Einsatz. Es zeigen sich bei beiden Verfahren klare Unterschiede zwischen den Messungen im ungeschädigten und geschädigten Zustand der Modellstruktur. Dies bedeutet, dass dieselben AFCs für die Schadenserkennung mit verschiedenen Verfahren geeignet sind, was vor allem in SHM Anwendungen von Vorteil ist. Weiter zeigt die Untersuchung, dass das gekoppelte Übertragungsverhalten des AFCs mit der Struktur bei der Anwendung solcher Elemente mitberücksichtigt werden muss, damit brauchbare und interpretierbare Resultate generiert werden können.

List of Symbols and Abbreviations

Symbols

A	area of the electrode
a	geometry constant
C	capacitance
$\mathbf{C}$	elastic stiffness tensor
$\mathbf{C^E}$	elastic stiffness tensor at constant electric field
c_1	phase velocity of the primary wave (dilatational bulk wave)
c_2	phase velocity of the secondary wave (shear bulk wave)
c_g	group velocity
c_{min}, c_{max}	minimal and maximal phase velocity
c_p	phase velocity
$\mathbf{D}$	electric displacement field
$\boldsymbol{d}$	piezoelectric tensor
d_{core}	core thickness
d_P	plate thickness
d_{AFC}	thickness of the AFC
$\mathbf{E}$	electric field
E	elastic modulus
$\mathbf{e}$	unit vector
$\boldsymbol{e}$	piezoelectric tensor
f	frequency
G	shear modulus
$G(f)$	density function
$H(f)$	transfer function (for emitter)
$H^*(f)$	transfer function (for receiver)
h	half plate thickness
k	wave number
l_a	active length of the AFC
l_P	plate length
l_{tot}	total length of the AFC = total fiber length
n	number of repeated measurements
$\mathbf{n}$	unit vector
n	number of wave mode
n	direction normal to a plane

q_{IDE}	spacing between two fingers of the IDE
q_{sim}	electrode spacing within the simulation of the emitter
q^*_{sim}	electrode spacing within the simulation of the receiver
R	resistance
r	radial axis
$\hat{s}$	estimated confidence interval
T	finite record length
t	time
t	direction tangential to a plane
$\mathbf{u}$	displacement vector
u_r, u_φ, u_x	displacement components in r,φ,x-coordinates
u_x, u_y, u_z	displacement components in x,y,z-coordinates
V	voltage
$\mathbf{v}$	velocity vector
v_A, v_B, v_C	measured velocity components along beam A, B and C
v_r, v_φ, v_x	particle velocity components in r,φ,x-coordinates
v_x, v_y, v_z	particle velocity components in x,y,z-coordinates
w_a	active width of the AFC
w_p	plate width
w_{tot}	total width of the AFC
$X(f)$	discrete Fourier transform of $x(t)$
x	axis normal to the plate
$x(t)$	discrete time signal
Y	electrical admittance
$\bar{Y}^E$	complex Young's modulus of PZT at constant electric field
$Y(f)$	discrete Fourier transform of $y(t)$
y	axis in the plane of the plate and perpendicular to x
$y(t)$	discrete time signal
Z	electrical impedance
z	axis along the fiber direction of the AFC
$\hat{\gamma}$	estimated coherence
Δ	discret step
$\boldsymbol{\epsilon}$	strain tensor
$\boldsymbol{\varepsilon}^{\boldsymbol{\epsilon}}$	dielectric permittivity at constant strain
λ	wave length
λ	Lamé coefficient
λ_{min}	minimal wave length
μ	Lamé coefficient, shear modulus
ν	Poisson's ratio
ξ	scaling factor for the simulation of the emitter
ξ^*	scaling factor for the simulation of the receiver
φ	tangential axis
ρ	density

$\boldsymbol{\sigma}$	stress tensor
σ_{ij}	mechanical stress
Φ	electric potential
ω	angular frequency
$\mathcal{L}$	matrix of spatial derivative operators

Abbreviations

AE	Acoustic Emission
AFC	Active Fiber Composite
AU	Acousto Ultrasonic
DFT	Discrete Fourier Transform
DS	Damage state
EMI	Electro-Mechanical Impedance
FDTD	Finite-Difference Time Domain
FEM	Finite Element Methode
FFT	Fast Fourier Transform
FIT	Finite Integration Technique
GPIB	General Purpose Interface Bus
GW	Guided Wave
IP	In-Plane
IDE	Interdigitated Electrodes
MFC	Macro Fiber Composite
NDT	Non-Destructive Testing
OoP	Out-of-Plane
PZT	Lead-Zirconate-Titanate
SHM	Structural Health Monitoring
2D	two-dimensional
3D	three-dimensional

List of Figures

2.1 Dispersion curves for an aluminum plate 10
2.2 Displacement fields of Lamb waves 11
2.3 Different types of typical piezoelectric transducers used in NDT and SHM 14
2.4 Schematic of the deformations of an AFC during excitation 16
2.5 Schematic of an AFC 17

3.1 Schematic arrangement of the system AFC-plate 27
3.2 Typical input and output signals with time window 29
3.3 Schematics of the 2D and 3D model 31
3.4 Allocation of the variables on a staggered grid 36
3.5 Diagram of the simulation algorithm for the piezoelectric material . . 37
3.6 Simulated interfacial normal and shear stress distributions 41
3.7 Simulated total displacements at the surface of the quarter-plate excited by an AFC 41
3.8 Simulated surface velocities at $(r, \varphi) = (100, 15°)$ 42
3.9 Simulated displacement fields in a plate with and without surface bonded AFC used as receiver 43
3.10 Simulated surface velocities, AFC signal, and energies 44
3.11 Example of a simulated transfer function 45
3.12 Close-up view of bonded AFC and piezoceramic transducer 48
3.13 Experimental setup 49
3.14 Laser measurement of the IP and OoP velocity components by applying a Bauernfeind prism 51
3.15 Measured transfer function of the voltage divider 52
3.16 System for the experimental determination of the transfer function of the AFC as emitter 52
3.17 Example of the transfer and coherence function 54
3.18 Example of overlapped transfer functions 54
3.19 Radial IP and OoP surface velocities at $(r, \varphi) = (200, 0°)$ 56
3.20 Tangential IP surface velocity at $(r, \varphi) = (100, 30°)$ 57
3.21 IP surface velocities at $(r, \varphi) = (200, 0°)$, excitation with 400 kHz . . 58
3.22 Simplified situation of wavelength vs. AFC length in fiber direction . 59
3.23 Transfer functions of the AFC as emitter for $(r, \varphi) = (200, 0°)$ 60

3.24 Measured transfer functions of two similar AFCs used as emitter for $(r, \varphi) = (400, 0°)$ . . . 61
3.25 S_0 transfer functions of the AFC as emitter for $(r, \varphi) = (100/400, 0°\text{-}60°)$ . . . 63
3.26 A_0 transfer functions of the AFC as emitter for $(r, \varphi) = (200, 0°\text{-}30°)$ 64
3.27 Simplified situation of wavelength vs. AFC length in arbitrary direction 65
3.28 Simulated S_0 transfer functions of two AFCs used as emitter with different width . . . 66
3.29 Simplified situation of wavelength vs. AFC width in arbitrary direction 67
3.30 Frequencies of minima and maxima in function of the length of the transducer used as emitter . . . 68
3.31 S_0 transfer functions of the shortened AFC as emitter for $(r, \varphi) = (100/400, 0°\text{-}60°)$ . . . 69
3.32 A_0 transfer functions of the shortened AFC as emitter for $(r, \varphi) = (200, 0°\text{-}30°)$ . . . 70
3.33 Measured voltage signal from the AFC as receiver and surface velocities 71
3.34 Simulated and measured voltage signal from the AFC as receiver and surface velocities . . . 72
3.35 Measured voltage signal from the AFC as receiver, excitation with 400 kHz . . . 73
3.36 Transfer functions of the AFC as receiver in fiber direction . . . 74
3.37 Measured transfer functions of the AFC as receiver for several incident angles . . . 76
3.38 Simplified situation for the AFC as receiver . . . 77

4.1 Experimental setup for the investigations with the guided wave based method . . . 82
4.2 Experimental setup for the investigations with the eletro-mechanical impedance method . . . 85
4.3 Simulated total displacements in a cross section through the sandwich plate . . . 88
4.4 Simulated and measured surface velocities on a sandwich plate . . . 88
4.5 Schematic arrangement for the delamination detection with piezoceramic transducers . . . 90
4.6 Time histories and DFTs for the delamination detection with piezoceramic transducers . . . 91
4.7 Schematic arrangement for the delamination detection with MFCs . . 93
4.8 Time histories and DFTs for the delamination detection with MFCs . 95
4.9 Schematic arrangement for the detection of reversible delaminations . 97
4.10 Time histories for the detection of reversible delaminations . . . 98
4.11 Schematic arrangement for the delamination detection with AFCs . . 100
4.12 Time histories for the delamination detection with AFCs . . . 102
4.13 DFTs for the delamination detection with AFCs . . . 103
4.14 Time histories and DFTs for the delamination detection with piezoceramic transducers instead of AFCs . . . 105

4.15 Spectra of the electrical impedance for the delamination detection with AFCs and disc transducers 107

C.1 Measured transfer functions of AFC-1 used as emitter 121
C.2 Measured S_0 transfer functions of AFC-1 ($l_a = 31$ mm) used as emitter and coherence function 122
C.3 Measured A_0 transfer functions of AFC-1 ($l_a = 31$ mm) used as emitter and coherence function 123
C.4 Measured transfer functions of AFC-2 used as emitter 124
C.5 easured transfer functions of the shortened AFC-3 used as emitter . . 125
C.6 Measured S_0 transfer functions of AFC-1 ($l_a = 31$ mm) used as receiver and coherence function 126

D.1 Measured transfer functions of MFC-1 used as emitter 127
D.2 Results of the measurements from transducer MFC-1 to MFC-2 at 100 kHz 128
D.3 Results of the measurements from transducer MFC-1 to MFC-2 at 300 kHz 129
D.4 Results of the measurements from disc transducer P3 to P4 at 100 kHz130
D.5 Results of the measurements from disc transducer P3 to P4 at 100 kHz131
D.6 Measured transfer functions from the AFC-4 to the AFC-5 132
D.7 Measured transfer functions from the disc transducer P7 to P8 133

List of Tables

2.1 Material parameters for an AFC 18

3.1 Definition of input and output signals 26
3.2 Qualitative results of the sensitivity analysis 46

4.1 Overview of measurements for the delamination detection with AFCs 101

A.1 Material parameters for an AFC as used for the simulation 115
A.2 Material parameters for aluminum 115
A.3 Material parameters for the core material as used for the sandwich plates 116

B.1 Overview of geometric dimensions 117
B.2 Overview of positions of measurement and excitation 118
B.3 Overview of excitation signals 119

Chapter 1

Introduction

1.1 Motivation

Monitoring aerospace, civil, and mechanical engineering structures over their lifetime in order to improve reliability and availability and reduce life-cycle costs is of great interest. In recent years, the number of published works concerning the so-called structural health monitoring (SHM) increased rapidly. A SHM system, which is an integrated part of the structure to be controlled, should be able to detect, locate and evaluate a damage in the structure, estimate its severity and monitor its evolution with time.

A variety of non-destructive testing (NDT) methods for damage detection and evaluation has been developed and used (see, e.g., [74]), such as eddy current testing, radiography, thermography or ultrasonic testing to name just a few. However, not all NDT methods are well-suited for SHM due to high costs, high consumption of time, equipment and manpower, or due to safety aspects (e.g., the use of X-ray in an aircraft in service). Many different approaches for SHM are reported in the literature. One potential approach is based on the use of optical fiber sensors (see, e.g., [33]) for monitoring mechanical strains in the structure during operation. The sensors can easily be attached or integrated in, e.g., glass or carbon fiber reinforced composite structures. A single sensor enables measuring strains at several positions along the fiber and, moreover, is suitable for damage detection. Other promising approaches for SHM, in particular for monitoring plates or pipes, are based on NDT methods which use structural vibrations or propagating guided waves. These methods which will be considered in this thesis allow for monitoring large areas without the necessity of a time-consuming scanning process as it is required, e.g., for classical ultrasonic testing. As transducer elements, piezoelectric devices which can be permanently attached to or even integrated into the structure under control are well-suited since they can not only be used as sensors (or receivers) but also as actuators (or emitters) to excite waves and vibrations.

In most investigations for SHM applications with wave or vibration based methods (so called acoustic NDT methods), thin piezoelectric ceramic elements are used. However, these elements are brittle and can not directly be attached to curved

surfaces. Alternatively, piezocomposite transducers such as active fiber composites (AFCs) or the similar macro fiber composites (MFCs, see Sec. 2.4) can be applied. AFCs consist of one layer of piezoelectric ceramic fibers embedded in an epoxy matrix and sandwiched between two sets of interdigitated electrodes. They were initially developed by Bent and Hagood [9] for structural control. However, their thin planar size and their conformability to even biaxially curved surfaces make AFCs (as well as MFCs) suitable as transducer elements for SHM applications in plates, shells or pipes (see, e.g., [13], [39], [72], [79]).

Motivated by the existing know-how of manufacturing AFCs at the Laboratory of Mechanical Systems Engineering at Empa [35] and the know-how of elastic wave propagation at the Institute of Mechanical Systems at ETH Zürich, e.g., [20], [29], the topic of this thesis is the fundamental investigation of AFCs used as transducer elements for acoustic NDT methods. This investigation includes a characterization of the dynamic behavior of the AFC as well as an experimental application of AFCs for damage detection. AFCs – manufactured in-house – have been successfully used for NDT in separate laboratory experiments performed at Empa: they substituted conventional piezoelectric transducers in acoustic emission and acousto-ultrasonic applications ([6], [14]), they were applied for the electro-mechanical impedance method [5], and they were used as strain sensors in a low frequency range [49]. Therefore, different NDT methods for which the same AFCs are used as transducer elements will be combined within the experimental application. Since the methods are sensitive to different damage types, the performance of a SHM system could be improved without increasing the number of required transducers.

However, before AFCs can be applied for damage detection, their dynamic behavior must be characterized. Due to their design and manufacturing they have anisotropic material properties which lead to directionally dependent emitting and receiving capabilities. Hence, for a SHM system with AFCs, this characteristic must be taken into account. Only a few papers concerning this topic can be found in the literature. Raghavan and Cesnik [64] analytically described the excitation of elastic waves in an isotropic plate with a mechanical loading which represented the surface bonded AFC/MFC. Matt [47] analytically derived the response of an AFC/MFC to incoming Lamb waves from arbitrary direction. Within both investigations, the transducer-structure interaction as well as the coupled electro-mechanical behavior of the piezoelectric element is neglected. This is reasonable as long as the stiffness of the transducer is much smaller than that of the plate. However, this is not generally fulfilled.

For taking into account the complex electro-mechanical coupling, the transducer-structure interaction, and the anisotropy of the transducer, and in order to get quantitative results which are comparable with experiments, a numerical approach is best suited. In some works Lamb wave propagation caused by surface bonded piezoelectric transducers including the electro-mechanical coupling of the piezoelectric material is investigated ([46], [51], [65]). However, numerical investigations of surface bonded AFC/MFC used as emitter and receiver of transient waves have not been reported in the literature to the best knowledge of the author.

1.2 Aim of the Project

In any application of an AFC – or of other piezoelectric transducers – in SHM with acoustic NDT methods, the element has two fundamental functions. These are emitting and receiving elastic waves which propagate in the structure on which the element is applied. For conception and optimization of the AFC for specific applications, it is essential to understand the dynamic behavior of the element coupled to a structure. Hence, this thesis is focusing on two major aspects:

- **Characterization of AFCs** as anisotropic transducer elements for emitting and receiving elastic waves. This includes the development of a model which describes the electro-mechanical behavior and the interaction with waves propagating in a structure as well as an experimental validation of the results obtained from the model.

- **Experimental application of AFCs** for damage detection in a model structure. This builds the first step toward a SHM system with AFCs. Two different acoustic NDT methods are applied but with the same AFCs which are primarily optimized according to the findings of the former characterization.

1.3 Outline

The thesis is divided into three parts. The first presents some general aspects which are important for the following two parts: the characterization and the application of AFCs. At the end, conclusions and outlook for both topics are given.

- In chapter 2 a brief introduction to the topic of SHM and acoustic NDT methods is given. More specific literature for the following two parts is presented at the beginning of the corresponding chapter. Elastic waves in plates are introduced and the dispersion curves for an aluminum plate are shown. Further, piezoelectric transducers are presented, including the constitutive relations for piezoelectric materials, the description of different transducer types, and the specifications of the AFC itself and its manufacturing.

- In chapter 3 the procedure for characterizing the AFC as emitter and receiver of elastic waves in plates is first described and the concept of the transfer function is introduced. The numerical model is presented by listing all required equations and by describing the numerical algorithm. Examples of the simulation of the AFC as emitter and as receiver are presented. The experimental setup and the measurement procedure is explained. The results of both the numerical model and the experiments are then presented and discussed.

- In chapter 4 applications with AFCs and other piezoelectric elements used for damage detection in an aluminum sandwich plate are presented. Wave propagation in the sandwich plate and the influence of a delamination between face sheet and core on the wave propagation is investigated experimentally. The

concept of a artificial and reversible delamination is presented and experimentally realized. In a final experiment the AFC is applied for the detection of reversible delaminations in a sandwich plate with two different NDT methods, one is based on wave propagation, the other on structural vibrations. The results are presented and discussed.

Chapter 2

General Aspects

2.1 Structural Health Monitoring

Structural health monitoring (SHM) denotes an approach which allows for detecting and interpreting damages in aerospace, civil, and mechanical engineering structures or infrastructures in order to improve reliability and reduce life-cycle costs [34]. An SHM system is permanently attached to or even integrated into the structure and can be part of a smart or intelligent structure. The monitoring process is performed continuously or periodically during service or when the structure is taken out of service.

One reason for implementing a SHM system is of course the safety [74]. By monitoring the structure or important components of it, unexpected failure can be avoided since damages are detected and repaired before they become critical. In particular, structures made of fiber reinforced composites, e.g., with glass or carbon fibers, are susceptible to fail without any advance indication since the damages (or pre-existing defects) may be only barely visible because they are small or located underneath the surface.

However, the probably most important reasons for SHM are of economical nature [74]. A total failure of a structure may cause large costs. Further, if a damage is detected in an early stage, the costs for the repair will in general be smaller. Moreover, inspection and maintenance intervals can be optimized and the duration of the cost-intensive out-of-service time can be reduced as well as the manpower due to permanently installed sensors and fully or partly automated monitoring procedures. Further, a permanent monitoring may allow for using a structure in excess of its planed service life-time without loss of safety. All these aspects are related to an improvement of the availability of the structure. Another aspect is the factor of safety which has to be taken into account for dimensioning structural elements. If the structural integrity is known at any time during service due to the SHM system, lower safety factors could be applied [33]. This yields reduced dimensions of the structural elements and thus a reduction of the structure's weight which is of great interest not only for the aerospace industry.

There are several issues related to SHM: sensor technology and measurement

technique; monitoring strategy, e.g., sensor position or type of excitation (if needed); signal processing; signal interpretation; and hardware components, e.g., cables or power supply [33]. The process of the damage identification in SHM can be divided into four steps [88]:

- Existence/detection of a damage
- Localization of a damage
- Type of a damage
- Severity of a damage

The findings are needed for the estimation of remaining life-time. Many different methods and combinations of them are proposed in the literature to solve these tasks. Established NDT methods or newly developed solutions can be applied. For this thesis methods based on wave propagation and on structural vibrations are applied. A brief introduction to these methods is given in the next section. An overview on other potential methods for SHM as well as on different aspects of such a system for aerospace structures can be found in [74]. Due to the vast amount of literature over the last 30 years, the reader is referred to [18] and [88], which both give an introduction to SHM and build a starting point for further literature research. Because of the increased attention of SHM in the engineering community, several new conferences have been held in recent years that focus on SHM (e.g., the International Workshop on SHM, the European Workshop on SHM) and a peer-reviewed journal has been initiated (Journal of Structural Health Monitoring).

2.2 Acoustic Non-Destructive Testing Methods

Acoustic NDT addresses for this work any method which is based on structural dynamics in general (vibrations and wave propagation phenomena). However, the methods differ in some aspects:

- **Passive and active approaches**. Passive methods use only sensors while active methods use both actuators and sensors. Hence, the former depends on external excitations such as dynamic loadings, impacts, or crack initiation and growth. Most SHM systems must hence be switched on during these events (which may happen randomly) or the information will be lost. In contrast, an active system excites the structure by itself and allows for performing measurements independently of the moment when a damage occurs. Further, it becomes possible to measure a baseline (or reference) and compare it with data measured at a later time. Some methods can be applied passively or actively, e.g., the frequency response method (see text below) can use dynamic loadings of a structure in service or forces applied by actuators.

- **Time scale**. Some methods deal with harmonic or stationary states while others consider transient processes. A harmonic state – or vibration – is reached when the wave which starts to propagate at the beginning of an excitation is reflected a few times at the boundaries of the structure and the reflections superpose each other. In contrast, for wave based methods only the wave which arrives first at the measurement point is of interest. Hence, typically the first few milliseconds after the excitation have to be considered which requires measurement techniques with sufficiently high resolution.

- **Frequency range**. The applied frequency and the material and geometrical parameters of the structure define the wavelength. With increasing frequency the wavelength usually decreases and the material damping increases. Moreover, the higher the frequency the smaller the size of still detectable damages. Therefore, the frequency defines the sensitivity of the method as well as the area which can be monitored by one sensor.

In the following the most common methods are briefly explained. The guided wave based method and the electro-mechanical impedance method will be used for damage detection with AFC as presented in Chap. 4 where a more detailed description as well as a literature review can be found. The first four methods are based on elastic wave propagation while the other two are vibration based.

- **Acoustic emission (AE)** – passive, typical frequency range between 10 kHz and 1 MHz. When a material fractures, elastic energy is rapidly released which is known as acoustic emission. The energy propagates as a mechanical wave within the material and can be registered with sensors. The use of several sensors enables the localization of the source. Similarly, impacts (external loadings) can be detected and evaluated.

- **Guided wave based method (GW method)** – active, between 10 kHz and 1 MHz. Guided waves are elastic waves which propagate within a wave guide such as plates or pipes. They exist in several wave modes and are generally dispersive. Due to the wave guide and the relatively low frequencies, the waves can propagate long distances and are still sensitive to small discontinuities. Often, a pitch-catch configuration is applied, where waves are sent from one transducer (actuator or emitter) to a second one (sensor or receiver). In order to limit the number of excited propagating wave modes and to reduce the effects of the dispersion, an excitation signal within a relatively small frequency range (narrow band) is used. The well-defined propagation of the waves allows for tracing the waves and, hence, for improving the evaluation of the data.

- **Acousto-ultrasonics (AU)** – active, above 0.5 MHz. In contrast to the GW method, a multitude of guided wave modes is excited with a broad band excitation signal sent to an emitter. Due to the presence of several wave modes, the interpretation of the signals measured with a receiver is difficult. Hence, statistical methods are usually used for the data evaluation.

- **Ultrasonics** – active, typically above 1 MHz. Elastic waves are excited with high frequency pulses so the wavelengths are much smaller than the dimensions of the specimen. Hence, only bulk waves are excited whose propagation is well-defined and traceable since they are non-dispersive. Both, a pulse-echo configuration – the same transducer is used for emitting and receiving the waves – or a pitch-catch configuration are possible. Ultrasonics is one of the best established NDT methods with a wide range of applications.

- **Modal analysis** or **frequency response method** – active or passive, below 100 kHz. The dynamic behavior in a relatively low frequency range is investigated. Several vibration parameters such as eigenfrequencies, eigenmodes, or damping are evaluated. The excitation is achieved with actuators or by other dynamic loadings.

- **Electro-mechanical impedance method (EMI method)** – active, between 10 kHz and 500 kHz. The complex electrical impedance (ratio between applied, alternating voltage and the resulting current) of a piezoelectric element which is mounted to the structure is measured. Due to the electro-mechanical coupling over the piezoelectric effect the measured electrical impedance is influenced by the dynamic behavior of the structure. The frequencies are usually much higher than for the modal analysis. This leads to a better sensitivity to smaller defects, however, the area which can be monitored by a single transducer decreases.

There is a variety of transducers (actuators/sensors or emitters/receivers) available for the specific purposes. The most common are optical fiber sensors, piezoelectric transducers, laser techniques (including laser interferometry), strain gauges, electro-magnetic acoustical transducers (EMAT), micro-electro-mechanical systems (MEMS). In SHM systems, in particular when an active approach is chosen, often piezoelectric transducers are applied since the same element can be used as both actuator and sensor. A brief introduction to piezoelectricity and typical transducer types, including AFC, is given in Sec. 2.4.

2.3 Elastic Waves in Plates

In a linear-elastic plate with traction-free boundaries two different types of plane waves exist (e.g., [1], [67]). The first are the shear-horizontal (SH) modes and are built by the superpositions of reflected horizontally polarized shear waves (secondary waves or SH bulk waves). The second are the Lamb waves, analytically derived primarily by Horace Lamb [37]. They result from mode conversion phenomena and superpositions of reflected dilatational waves (primary waves or P bulk waves) and vertically polarized shear waves (secondary waves or SV bulk waves). Both types of plane waves exist only in certain modes and are described by the dispersion-relations, which relate the phase velocity with the wave number, or frequency, depending on the plate thickness and the material properties.

The dispersion-relation for the SH modes is given by [67]

$$\left(\frac{c_p}{c_2}\right)^2 = 1 + \left(\frac{n\pi}{2hk}\right)^2 \tag{2.1}$$

where $2h$ is the plate thickness, c_p the phase velocity and $k = \omega/c_p$ the wave number of the n-th SH mode ($n = 0, 1, 2, \ldots$), and ω the angular frequency. The phase velocity of the shear wave is defined as $c_2 = \sqrt{\mu/\rho}$ where μ is one of the two Lamé constants and ρ is the density. With $n = 0$, Eq. (2.1) results in $c_p = c_2$. Thus, the first mode is non-dispersive, while all other modes propagate dispersively. The displacements of the SH_0 mode are constant across the thickness.

The Lamb waves are divided into symmetric or longitudinal modes and antisymmetric or transversal modes. The dispersion-relation for the symmetric modes is given by [67]

$$\frac{\tan(\xi_2 h)}{\tan(\xi_1 h)} = -\frac{4k^2\xi_1\xi_2}{(k^2 - {\xi_2}^2)^2} \tag{2.2}$$

and for the antisymmetric modes by

$$\frac{\tan(\xi_2 h)}{\tan(\xi_1 h)} = -\frac{(k^2 - {\xi_2}^2)^2}{4k^2\xi_1\xi_2} \tag{2.3}$$

where ${\xi_1}^2 = {k_1}^2 - k^2$ and ${\xi_2}^2 = {k_2}^2 - k^2$. Further, the phase velocity of the dilatational wave is $c_1 = \sqrt{(\lambda + 2\mu)/\rho}$ where λ and μ are the Lamé constants. The wave numbers of the dilatational wave is $k_1 = \omega/c_1$ and of the shear wave $k_2 = \omega/c_2$.

The numerical solutions of Eq. (2.1) - (2.3) for an aluminum plate are given in Fig. 2.1. Also the group velocities, calculated with $c_g = d\omega/dk$, are shown. It can be seen that there is an infinite number of wave modes and for any given frequency at least the SH_0 mode and two Lamb wave modes, the S_0 and the A_0 mode, coexist.

For Lamb wave based damage detection it is advantageous to work with a single mode to keep the measured signals as simple as possible [2]. Thus, frequencies below the first cut-off frequencies of higher wave modes are often applied. Hence, for an aluminum plate with a thickness of 1 mm as used in this thesis, the frequencies must be below 1 MHz. Within this frequency range the S_0 mode propagates almost non-dispersively, while the A_0 mode is highly dispersive.

The displacement fields of the Lamb wave modes can now be derived with the solution of the dispersion-relations [67]. This is important since the displacement field is not linear across the thickness of the plate and it depends on the frequency. Figure 2.2 shows the displacement fields u_z (in propagation direction) and u_x (perpendicular to the plate) for the S_0 and A_0 mode for several frequencies. Further, the ratios of u_x and u_z at the surface of the plate are given since the wave field is measurable only at the surface. It can be seen that below 1 MHz the S_0 mode has almost in-plane (IP) surface displacements, while the out-of-plane (OoP) component is dominant for the A_0 mode.

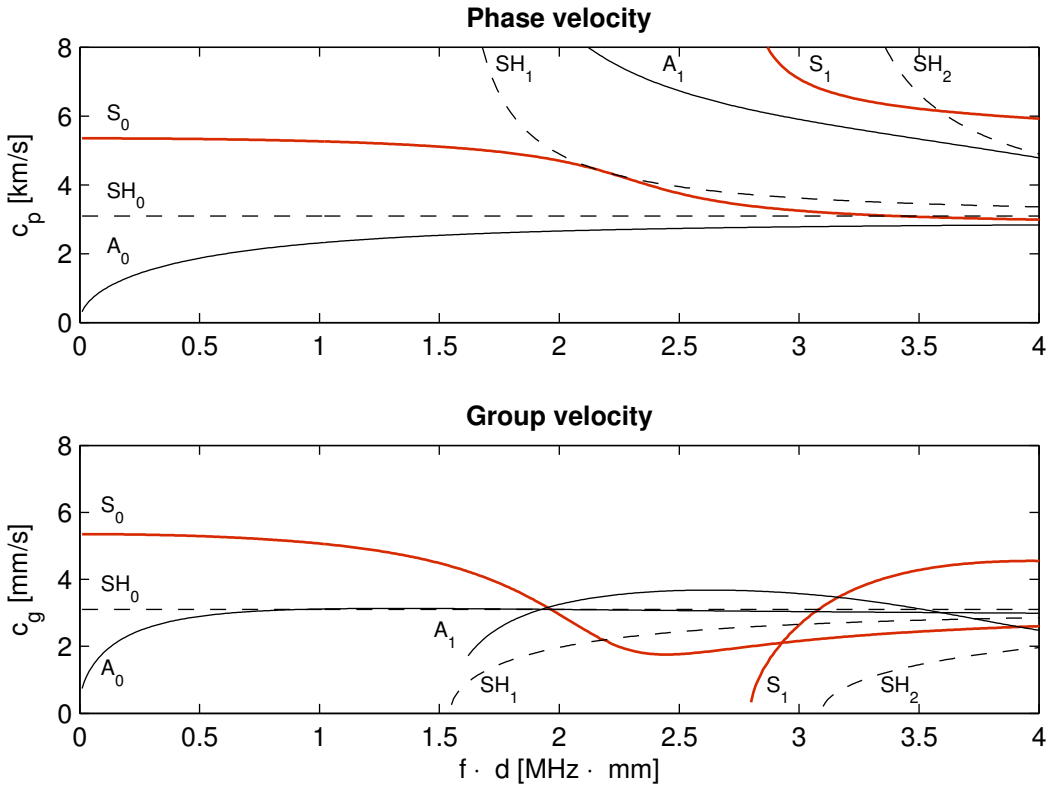

Figure 2.1: Dispersion curves for symmetric (red) and antisymmetric (black) Lamb wave modes and for shear-horizontal wave modes (dashed) for an aluminum plate of thickness d.

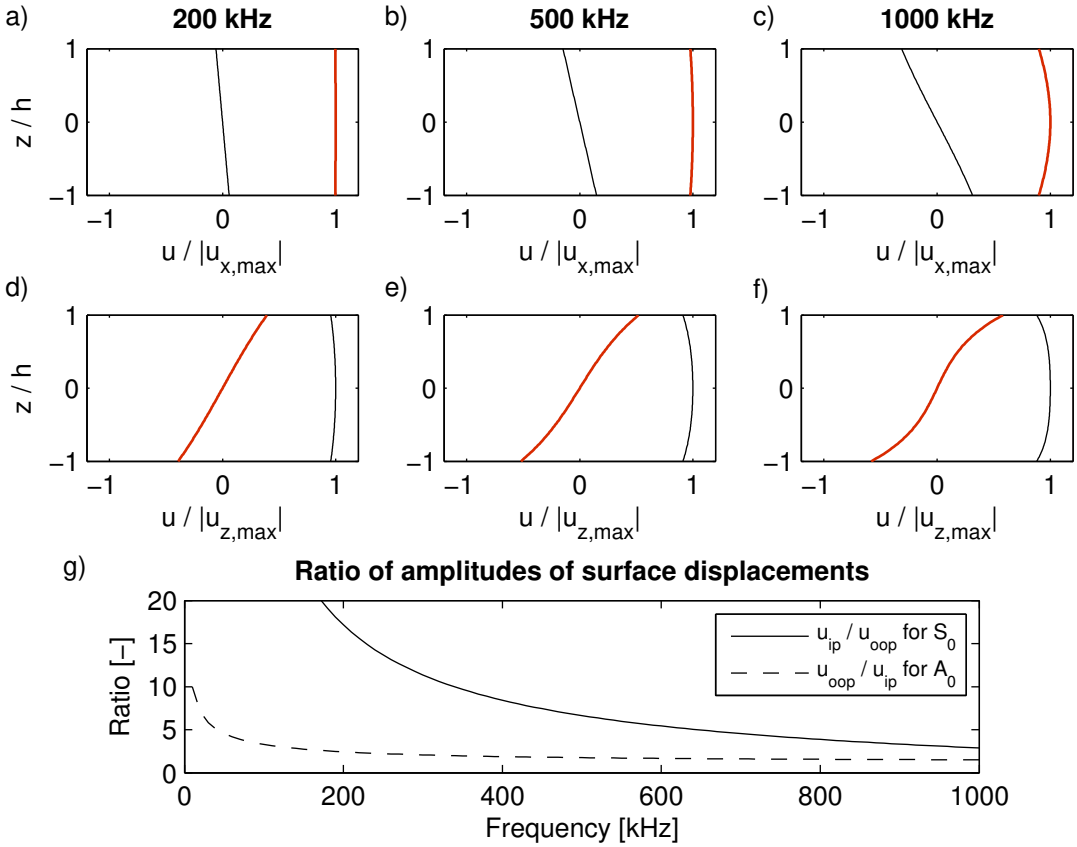

Figure 2.2: Normalized displacement fields of Lamb waves across the thickness ($2h$ = 1 mm) of an aluminum plate for different frequencies for the S_0 (a-c) and the A_0 mode (d-f). The displacement u_z (red) is in propagation direction and u_x (black) is perpendicular to the plate. g) Ratio of the amplitudes of the surface velocities u_{IP}/u_{OoP} for the S_0 mode (solid) and u_{OoP}/u_{IP} for the A_0 mode (dashed).

2.4 Piezoelectric Transducers

Piezoelectric transducers are widely used in practice to convert mechanical energy into electrical energy or vice versa. They are applied in microphones as well as in simple lighters. One of the probably best known applications is in the field of medical ultrasound, where piezoelectric devices are used to emit and receive ultrasonic waves. The main part of every transducer is of course the piezoelectric material, however, the performance is also a result of its design and construction.

2.4.1 Constitutive Relations

Piezoelectricity can be assumed as a linear material property that relates electric fields with mechanical deformations or vice versa [66]. The generation of surface charges (as a result of electrical polarization within the material) when the material is subjected to mechanical stresses is termed the piezoelectric effect. However, the inverse piezoelectric effect describes the deformation of the material when an electric field is applied. The effect exists only in materials without a central symmetry in its crystallographic structure. A very common material in practice, that is also used in this work, is lead-zirconate-titanate (PZT), which is a polycrystalline ceramic with a perovskite crystal structure (e.g., [80]). Below the so called Curie-temperature, the positive and the negative charge sites do not coincide, so each elementary cell has a built-in electric dipole in certain directions given by the crystal structure. Neighboring dipoles tend to align with each other and form domains with a net polarization. One single grain of the polycristal consists of one or more domains, and the angle between the directions of the polarization of two neighboring domains within a grain is 90° or 180°. Due to the polycrystalline structure of the ceramic, the polarizations are oriented randomly throughout the material and no macroscopic piezoelectric effect is exhibited. To get a piezoelectric effect, a strong external electric field can be applied after heating the material near but below the Curie-temperature. The domains will align with the external field, which is held constant during the following cooling. When the electric field is removed, the dipoles remain aligned and a net polarization and therefore a macroscopic piezoelectric effect can be observed. This process is called the polarization and influences the electrical properties as well as the mechanical ones. After the polarization, PZT shows a transversely-isotropic material behavior [66]. The main axis of the anisotropy is equal to the direction of the polarization within the material.

The linear constitutive relations of a piezoelectric material can be derived by modifying Hooke's law (generalized for 3D) for linear elastic material with a term describing the piezoelectric coupling effect [66]. This leads to

$$\boldsymbol{\sigma} = \mathbf{C}^{\mathbf{E}} \cdot \boldsymbol{\epsilon} - \boldsymbol{e} \cdot \mathbf{E} \tag{2.4}$$

where $\boldsymbol{\sigma}$ represents the stress tensor of rank two, $\mathbf{C}^{\mathbf{E}}$ the elastic stiffness tensor of rank four at constant electric field, $\boldsymbol{\epsilon}$ the strain tensor of rank two, $\boldsymbol{e}$ the piezoelectric tensor of rank three, and $\mathbf{E}$ the electric field. Also the relation $D = \varepsilon E$ for describing

electrical properties of dielectrics has to be generalized and modified due to the coupling effect and the anisotropy to

$$\mathbf{D} = \boldsymbol{e} \cdot \boldsymbol{\epsilon} + \boldsymbol{\varepsilon}^{\boldsymbol{\epsilon}} \cdot \mathbf{E} \tag{2.5}$$

where $\mathbf{D}$ is the electric displacement vector and $\boldsymbol{\varepsilon}^{\boldsymbol{\epsilon}}$ the dielectric permittivity tensor of rank two at constant strain. The constitutive relations can also be given in three other forms since there are four different choices for the free electrical ($\mathbf{D}$, $\mathbf{E}$) and mechanical ($\boldsymbol{\sigma}$, $\boldsymbol{\epsilon}$) variables, however, this form will be used for the modelling part presented in Chap. 3.

Using the conversion table for the indices as follows

11	22	33	23	13	12
1	2	3	4	5	6

and the convention that the $\mathbf{e}_3$-direction corresponds to the main axis of the anisotropy the Eq. (2.4) and (2.5) for the transversely-isotropic PZT can be rewritten in a single matrix form as

$$\begin{bmatrix} \sigma_1 \\ \sigma_2 \\ \sigma_3 \\ \sigma_4 \\ \sigma_5 \\ \sigma_6 \\ \hline D_1 \\ D_2 \\ D_3 \end{bmatrix} = \left[\begin{array}{cccccc|ccc} c_{11} & c_{12} & c_{13} & 0 & 0 & 0 & 0 & 0 & -e_{31} \\ c_{12} & c_{11} & c_{13} & 0 & 0 & 0 & 0 & 0 & -e_{31} \\ c_{13} & c_{13} & c_{33} & 0 & 0 & 0 & 0 & 0 & -e_{33} \\ 0 & 0 & 0 & c_{44} & 0 & 0 & 0 & -e_{15} & 0 \\ 0 & 0 & 0 & 0 & c_{44} & 0 & -e_{15} & 0 & 0 \\ 0 & 0 & 0 & 0 & 0 & c_{66} & 0 & 0 & 0 \\ \hline 0 & 0 & 0 & 0 & e_{15} & 0 & \varepsilon_{11} & 0 & 0 \\ 0 & 0 & 0 & e_{15} & 0 & 0 & 0 & \varepsilon_{11} & 0 \\ e_{31} & e_{31} & e_{33} & 0 & 0 & 0 & 0 & 0 & \varepsilon_{33} \end{array}\right] \cdot \begin{bmatrix} \epsilon_1 \\ \epsilon_2 \\ \epsilon_3 \\ 2 \cdot \epsilon_4 \\ 2 \cdot \epsilon_5 \\ 2 \cdot \epsilon_6 \\ \hline E_1 \\ E_2 \\ E_3 \end{bmatrix}$$

With $c_{66} = \frac{1}{2}(c_{11} - c_{12})$, ten independent material constants remain: five elastic, three piezoelectric and two dielectric constants. Typical values for PZT are given, e.g., in [66]. The piezoelectric constants define the three different kinds of coupling. The e_{33} or the e_{31} defines the coupling between an applied external electric field in the $\mathbf{e}_3$-direction, i.e. in the direction of the polarization, and the resulting mechanical stresses in the $\mathbf{e}_3$-direction (longitudinal effect) or $\mathbf{e}_1$-direction (transverse effect), respectively. The e_{15} defines the coupling between an applied electric field in the $\mathbf{e}_1$-direction, i.e. perpendicular to the direction of the polarization, and the resulting shear stresses in the $\mathbf{e}_1$-$\mathbf{e}_3$-plane, which is addressed as index 5 (shear effect).

2.4.2 Different Types of Transducers

There is a variety of piezoelectric transducer types which are optimized for the different fields of applications. The single components needed for any transducer are at least the piezoelectric element, the electrodes, and the wires for connecting the transducer with the excitation or measurement system. Depending on the application, material and its polarization, geometries, and the electrode design can be varied and specific mechanical or electronical components can be added. To highlight the specific characteristic of AFCs some typical transducer types used in NDT and SHM are presented here.

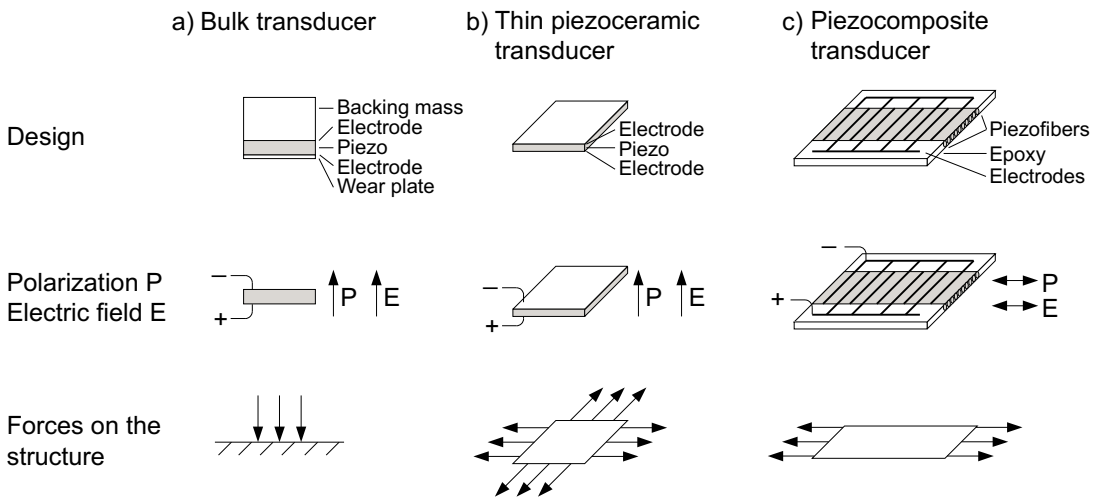

Figure 2.3: Schematics of typical transducer types used in NDT and SHM: a) bulk transducer, here polarized through the thickness, b) thin piezoceramic transducer, here a rectangular plate, and c) piezocomposite transducer, here an AFC made of piezoceramic fibers and with interdigitated electrodes.

Bulk Transducers

This type of transducer is often used for acoustic NDT methods like AE, AU, or classical ultrasonic testing. Beside the piezoelectric element and the electrodes on the front and back face, the probes usually also have a backing mass on the back face and a wear plate on the front face (see Fig. 2.3). The system of piezoelectric element and backing mass defines the resonance frequency and the damping of the element. The backing mass enhances the energy transfer to the test specimen. The wear plate protects the piezoelectric element from environmental impacts and, if needed, helps to achieve a better impedance match between piezoelectric element and specimen. The probe is reversibly coupled to the structure by applying a thin layer of couplant between the probe and the structure. If the piezoelectric element is polarized through the thickness, normal and shear stresses are generated during excitation (longitudinal and transverse effect, respectively). However, by using a specific couplant, only the normal stresses are transferred to structure. If the piezoelectric element is polarized in the plane, shear stresses are generated (shear effect) and then transferred to the structure. Since the coupled probe is relatively free from the structure, the behavior of the probe is mainly defined by its own dynamics [24]. There are narrow-band resonant devices or broad-band non-resonant devices. The probes are designed and optimized for specific applications and for the use in a well-defined frequency range. Since they are relatively expensive, large in their dimensions, and not designed for being permanently bonded to the structure, bulk transducers are not ideal for SHM applications.

Thin Piezoceramic Transducers

Contrary to the probes mentioned above this type of transducer (referred as piezoceramic transducer or within the experimental parts as disc transducer) consists only of a thin monolithic piezoelectric ceramic element and two electrodes on either side (see Fig. 2.3). The polarization is oriented through the thickness. These transducers are typically permanently bonded to the structure to be monitored. They have typical dimensions in the lateral directions of a few millimeters up to centimeters and in the thickness of around 1 mm. They are inexpensive and commercially available in a variety of shapes and sizes. Therefore, these elements are suitable for using them in SHM applications. Due to their small sizes and due to the strong coupling, they follow (and also influence) the dynamics of the structure [24]. During excitation normal and shear stresses are generated (longitudinal and transverse effect). Due to the bonding and a thickness which is much smaller than the wavelengths, the coupled electro-mechanical behavior is mainly described by the transverse effect. Hence, the transducer wants to expand and contract in both lateral directions and, in a simplified consideration, causes shear stresses on the structure's surface. These stresses are concentrated along the edges of the transducer and for opposite edges they have opposite signs.

Piezocomposite Transducers

The piezoelectric part of this type of transducer is composed of several piezoceramic elements embedded in a matrix system. The combination of the two materials leads to changed electro-mechanical properties and to a much better mechanical flexibility compared to the monolithic piezoceramic transducers which are brittle and thus susceptible to failures. Due to the large amount of possible combinations for piezocomposite transducers only the concept of the AFC is presented here (specifications and manufacturing details for the AFC are presented in the next subsection). A survey of other piezoelectric sensors and sensor materials can be found in Tressler et al. [80].

AFCs were initially developed by Bent and Hagood [9] as actuators for structural control. They consist of one layer of round piezoelectric ceramic fibers embedded in an epoxy matrix and sandwiched between two sets of interdigitated electrodes (IDE). Macro fiber composites (MFC), which were developed by Wilkie et al. [87], are almost identical to the AFC except from the manufacturing process which leads to rectangular ceramic fibers. Both types of elements have a thickness between 0.2 mm and 0.3 mm. Due to the perpendicular orientation of the electrode pattern to the fiber direction and due to the polarization procedure performed after manufacturing the element, i.e. with the aid of the IDE, the direction of the polarization in the piezoelectric material is aligned in fiber direction but with alternating sign for each section of the fiber between two oppositely charged electrode fingers. But since the electric field which is applied to the IDE for actuating the element is alternating in the same manner, an expansion or compression results over the whole length of the fiber. The same principle is valid also for the direct piezoelectric effect. Fig. 2.4

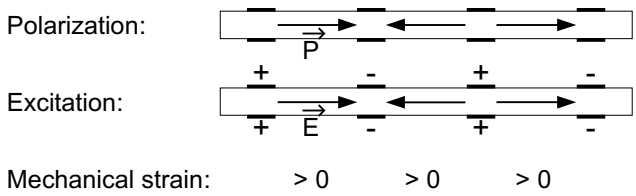

Figure 2.4: Simplified schematics of the polarization P, the electric field E used for excitation, and the resulting strain for an AFC with interdigitated electrodes.

shows this simplified situation where the more complex electric field and polarization underneath the electrode fingers are neglected. Due to the dominant alignment of the polarization in fiber direction, the electro-mechanical behavior in fiber direction is described by the longitudinal effect. Perpendicular to the fibers, the electro-mechanical behavior is described by the transverse effect. Additionally, also the mechanical properties are anisotropic due to the unidirectionally aligned ceramic fibers and the presence of the epoxy matrix between the fibers. Consequently, the performance of the AFC/MFC is much more pronounced in fiber direction than perpendicular to it.

Analogous to the thin piezoceramic transducer the dynamic behavior of the AFC or MFC is dominated by the dynamics of the structure when the element is permanently bonded to the structure. In a simplified consideration, the AFC/MFC causes shear stresses on the structure's surface but only at either end of the fibers. The thin planar size and the conformability to curved surfaces make AFCs/MFCs suitable as transducer elements for SHM applications ([13], [39], [64], [72], [79]).

2.4.3 Active Fiber Composite

The fibers of the AFC as used in this work are made of PZT-5A (commercial fibers from Smart Materials Corp., Sarasota, USA) and have a diameter of around 0.25 mm. They are embedded in a two-component epoxy resin (Araldite LY 564/-Aradur 2954 from Vantico AG, Basel, Switzerland). The IDE are screen-printed on Kapton foil (100 HN, 25 μm thick, supplied by Dupont, Mechelen, Belgium) with a silver paste (CB025 from Dupont). The following dimensions correspond to a standard design, which was applied for all AFCs used in this work (see Fig. 2.5). The fingers of the standard IDE have a width of around 0.2 mm and the electrode spacing is around 0.9 mm. The overlapping length of two oppositely charged electrode fingers is 20 mm and the distance between the two outer fingers is 31 mm, which results in an active area of $l_a \times w_a = 31$ mm $\times$ 20 mm. About 70 fibers are arranged regularly within these 20 mm. At the end of the production process the AFCs and, therefore, the fibers are cut to a length of around $l_{tot} = 34$ mm. The overall width of the AFCs is $w_{tot} = 40$ mm and the thickness is around $d_{AFC} = 0.3$ mm.

The production process started with the alignment of the unpolarized fibers in their original length (around 150 mm) on a plate with parallel grooves with the required spacing. The fibers were held together with adhesive tape placed at the

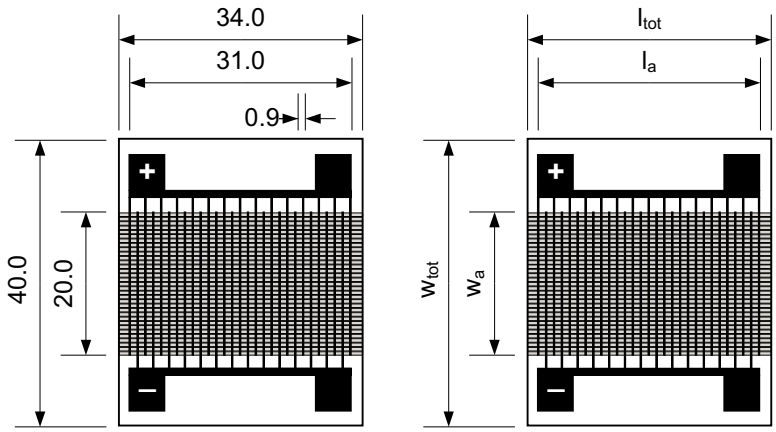

Figure 2.5: Schematic of an AFC manufactured at Empa with standard design (left, dimensions in [mm]) and the nomenclature of the dimensions (right). The active area is $l_a \times w_a$.

ends of the fibers. This fiber layer and the epoxy resin were then compounded between the two sets of electrodes and placed under a hydraulic press (ca. 0.2 bar). The AFC was cured at 120° C for 1 hour under the press and post cured at 160° C for 8 hours outside the press. Copper wires for connecting the electrodes were soldered to the contact points. The polarization was performed over the IDE with an applied electric voltage of 2.4 kV in an oven at 80° C for 20 minutes [35]. In order to exclude changes in the epoxy resin during polarization, the temperature was chosen far below the glass transition temperature of the epoxy resin (around 150° C) which was also below the Curie-temperature of the PZT material (around 335° C). Finally, the AFC was cut to the respective length and width. The AFC elements used for this work were produced in the laboratories at Empa.

The AFC theoretically shows orthotropic mechanical and electrical material behavior. However, the influence of the Kapton foil is negligible due to the relatively small thickness of the foil and the material properties which are comparable to those of the epoxy matrix. Therefore, a transversely-isotropic material behavior with its main axis aligned in fiber direction can be assumed. As for bulk PZT, ten independent material parameters are needed. The estimation of these parameters is not easy since there are no standard tests such as the ones used for piezoelectric bulk material. With a simple rule of mixture, some mechanical properties can be approximated [55]. Further, some experimental tests ([55], [49]) and finite element calculations [56] were performed at Empa to investigate the AFC's behavior. In Tab. 2.1 all parameters are listed. If a parameter is not known from experiments, it is assumed that in fiber direction the material behavior is dominated by the PZT fibers, while perpendicular to the fibers the epoxy matrix is dominant. Some parameters are assumed to be additionally reduced since the fibers are not equal to a bulk material. Here, the stiffness parameters are the elastic moduli E_{11} and E_{33}, the shear modulus G_{13}, and the Poisson ratio ν_{12} and ν_{13} and the piezoelectric constants d_{31}, d_{33}, and d_{51} since they are more common. A table with the material param-

Elastic moduli	E_{11}	[GPa]	8.5	see [55]
	E_{33}	[GPa]	21	from unpublished tensile tests performed at Empa
Shear modulus	G_{13}	[GPa]	3.1	see [55]
Poisson's ratios	ν_{12}	[-]	0.35	assumption
	ν_{13}	[-]	0.32	Poisson's ratio of the epoxy matrix
Piezoelectric constants	d_{31}	[pm/V]	-171	assumed to be equal to PZT-5A [66]
	d_{33}	[pm/V]	374	see d_{31}
	d_{15}	[pm/V]	470	assumption
Dielectric constants	ε_{11}	[-]	833	assumed as 10% less than the values for PZT-5A [66]
	ε_{33}	[-]	755	see ε_{11}
Density	ρ	[kg/m^3]	4700	see [55]

Table 2.1: Material parameters for an AFC (see also Tab. A.1 in App. A).

eters in the form as used in the constitutive relations in Sec. 2.4.1 is presented in Appendix A.

Chapter 3

Characterization of AFCs

3.1 Introductory Remarks

3.1.1 Concept

For any application of the AFC in the field of SHM with acoustic NDT methods, it is of importance to know how the AFC behaves when it is coupled to a structure and used as emitter or receiver of elastic waves or vibrations. Due to the small thickness of the AFC, the coupling and also the structure itself have major influences on the dynamic behavior of the AFC. Therefore, it is essential to investigate a system consisting of both, the AFC and the structure. For emphasizing the characteristic of the AFC, the structure is chosen as simple as possible. A linear elastic, isotropic aluminum plate is well suited for this purpose, also because plates are widely used in engineering applications. Further, by investigating the propagation of transiently excited waves, the influence of the eigenmodes of the plate can be neglected. Since vibrations result from superpositions of reflected waves from the boundaries, the length and width of the plate should be large compared to the length of the propagating wave packets, and the AFC should be positioned in the center of the plate. It is assumed that the AFC is perfectly coupled to the plate, i.e. the influence of the bonding layer is not considered.

For the characterization of the dynamic behavior of the surface bonded AFC, a numerical model is developed and experiments are performed to validate the model. The investigation is focused on the following aspects:

- How does the wave field in the plate excited by the AFC look like for different frequencies? What kind of modes are excited preferably and in which directions?
- How sensitive is the AFC for the different wave modes?
- How do the geometric dimensions of the AFC influence the results?

The system for the emitter has two symmetry axes through the center of the AFC, one in fiber direction and one perpendicular to it, and multiple modes will be excited. The system for the receiver might be asymmetric and only a single incoming

mode from an arbitrary direction will be considered. Therefore, the two fundamental functions of the AFC, emitting and receiving elastic waves, are investigated separately. Following the calibration methodology proposed by Veidt et al. [81] transfer functions are determined for the description of emitting and receiving capabilities of the AFC. The procedure for the determination is equal for both the simulations and experiments and is explained in Sec. 3.2. Most parts of the work have already been presented by the author in [10], [11] and [12].

3.1.2 Previous Work

Most of the work mentioned below concerns thin surface bonded piezoceramic transducers with an electrode on either side and a polarization through the thickness. Only a few papers can be found in the literature dealing with AFCs/MFCs and investigating their behavior as emitter and receiver of elastic waves. Although piezoceramic transducers differ from AFCs/MFCs, some findings are valid for both, at least in a two-dimensional consideration of a cross section through the plate and the AFC in its fiber direction.

Analytical Modelling

There is a variety of analytical approaches reported in the literature for investigating the generation of Lamb waves by piezoelectric transducers located on the surface of the plate and the resulting wave field within the plate. For all analytical models, the transducer is replaced by representative mechanical loading. One analytical approach is the normal mode expansion method [3] which uses infinite series of eigenmodes of Lamb waves for describing the wave field in the structure excited by surface mechanical loadings. Another analytical approach is the integral transform method for solving the boundary value problem [83]. In some work this method is combined with the Mindlin plate theory ([69], [82]). Giurgiutiu [23] developed a two-dimensional (2D) plane strain model based on the integral transform techniques and the Lamb wave equations. Raghavan and Cesnik presented a model based on three-dimensional (3D) linear elasticity for arbitrarily shaped piezoceramic transducers [63] and for AFCs/MFCs [64] and compared it with experimental results. Earlier works dealing with modelling AFC/MFC in a relatively low frequency range are presented by, e.g., Schulz et al. [72].

Giurgiutiu's 2D closed form solution for piezoceramic transducers assumes harmonic excitation with shear stresses on the surface of the plate concentrated at either end of the transducer and with opposite sign [23]. This consideration should be valid for the AFC in its fiber direction. The contributions from the symmetric modes to the IP surface displacement, u_z^S, at a distance z from the center of the transducer are given by

$$u_z^S(z,t) = -i\frac{l_a\sigma_0}{\mu}\sum_{k_S}\frac{\sin(k_S\frac{l_a}{2})}{k_S}\frac{N_S(k_S)}{D_S'(k_S)}e^{i(k_S z-\omega t)} \tag{3.1}$$

where σ_0 is the amplitude of the excitation, μ is the Lamé constant of the plate, k_S is the wave number of the corresponding S mode, and the term N_S/D'_S describes the Lamb waves in the plate. It can be seen from the term $\sin(k_S\frac{l_a}{2})$ that the excited Lamb waves show maximal amplitudes at frequencies where the transducer length is equal to odd multiples of half the length of the wave propagating in the plate. For even multiples, on the other hand, the amplitudes are minimal at corresponding frequencies. Thus, the frequencies of minima and maxima depend on the length of the transducer and the wave characteristic of the plate. Due to the different phase velocity and, therefore, different wavelength, maxima and minima occur at different frequencies for the S_0 and A_0 mode for a given transducer length. By choosing a specific transducer length, it seems feasible to generate one single mode preferably (so called Lamb wave tuning). This is desirable in order to develop a monitoring system as simple as possible since damage detection with Lamb waves can be very complex due to mode conversion phenomena ([39], [41]).

Raghavan and Cesnik [64] modeled the AFC/MFC as causing surface shear stresses concentrated at the ends of the fibers and uniformly distributed along the width of the transducer. The contributions of the symmetric modes to the IP component of the surface displacement oriented perpendicular to the fiber direction of the AFC, u_y^S, can approximately be given for the far field as a function of the distance r from the center of the transducer and of the angle φ from the fiber direction by

$$u_y^S(r,\varphi,t) \approx -i\frac{-4\sigma_0}{\pi\mu}\sum_{k_S}\sqrt{\frac{2\pi}{k_S r}}\frac{M_S(k_S)}{[D_{SH}D'_S(k_S)]}\cos\varphi \cdot \sin(k_S\frac{w_a}{2}\sin\varphi)\sin(k_S\frac{l_a}{2}\cos\varphi)e^{i(k_S r+\pi/4-\omega t)} \tag{3.2}$$

The term with the root describes the attenuation of the waves due to the circular radiation within the plate and indicates that the wave field tends to be circular crested in the far field. The following term describes the Lamb wave modes as well as the SH modes which are also excited by an AFC/MFC. The next three factors define the dependence of the surface displacements from the angle φ and the geometry of the transducer. Further, Raghavan and Cesnik [64] reported the so called shear lag effects (as primarly described by Crawley and de Luis [15]) wherein the force transfer occurs over a finite length close to the edge instead of exactly at the edge. They attribute differences between the analytical and experimental results to the use of uncoupled transducer-structure dynamics for their model. The application of the proposed analysis to cylindrical coordinates enables describing the behavior of circular transducers with IDE in tangential direction [70].

In order to account for the electro-mechanical behavior of the piezoelectric element and the transducer-structure interaction Moulin et al. [51] described a 2D model in which they couple the normal mode expansion method with the finite element method for obtaining the stresses applied to the structure caused by the piezoceramic transducer. They extended it in a later work to a pseudo-3D modelling for finite transducer dimensions [52]. Veidt et al. [81] proposed a theoretical-

experimental hybrid approach for characterizing the coupled transfer behavior of surface bonded piezoceramic transducers. The theoretical part based on Mindlin plate theory concerns the wave propagation (only the A_0 Lamb wave mode was considered) in the structure, while a laser interferometer is employed as a non-contact receiver to experimentally characterize the electro-mechanical transfer function of the piezoelectric transducer. They extended their approach to describe the overall input-output behavior of a SHM system with piezoceramic transducers as emitter and receiver [45].

For analytical solutions of thin piezoelectric transducers used as sensors for Lamb waves the influence of the transducer on the wave propagating in the structure is generally neglected. This is reasonable if the stiffness (elastic modulus times thickness) of the transducer is much smaller than that of the plate and if the transducer is of small size (e.g., [64]). For the AFC and aluminum plate as used for this work, these two conditions are not necessarily fulfilled. If the transducer itself is neglected, the response of the transducer can be related to the strain field on the surface of the plate given by the incident wave and averaged over the area of the sensor. Depending on whether the electric circuit of the measurement system is assumed as a short-circuit or an open-circuit, the electric voltage can be derived from the charges accumulated at the electrodes ([64] for MFC/AFC) or by the integration of the electric field within the transducer ([47] for MFC), respectively. For both solutions the constitutive relations for piezoelectric material are needed. According to the work of Matt [47] the electric voltage V^S caused by an S_0 mode propagating in the plate in a direction at an angle φ from the fiber direction of the MFC can be written as

$$V^S = \frac{S_{MFC} \cdot A_S}{A \sin\varphi \cos\varphi} \sin(k_S \frac{w_a}{2} \sin\varphi) \sin(k_S \frac{l_a}{2} \cos\varphi) \tag{3.3}$$

The factor S_{MFC} contains the constitutive relations of the MFC as well as the conversion of the surface strains from the propagation direction to the axes of the MFC. Further, A_S describes the surface strains of the symmetric Lamb waves and A corresponds to the area of the electrodes. The factors which define the influence of the geometric dimensions of the transducer on the electric voltage are similar to those within the solution for the emitter (see Eq. (3.2)).

The works of Raghavan and Cesnik [62] and of Matt and Lanza di Scalea ([38], [48]) present interesting results for the behavior of piezoceramic transducers used for Lamb wave detection. Both stated that the electric voltage response increases with decreasing sensor dimensions. This seems reasonable because the sensor represents an ideal strain sensor if its dimensions are much smaller than the length of the waves. This is true in general for infinitesimal sensor dimensions but also for decreasing frequencies and thus asymptotically increasing wavelength if sensors with finite dimensions are used. Theoretically, the response is maximal if the frequency tends toward zero, which is contrary to the emitter where the amplitudes of the emitted waves tend toward zero. As soon as the sensor is larger than a half wavelength, tuning effects as described by Giurgiutiu [23] for the emitter take place and reduce the sensor response and lead to maxima and minima in the transfer

behavior. Although the transfer behavior of the emitter differs from the response of the receiver, elastodynamic reciprocity conditions are valid [38]. A transducer used as emitter and electrically excited with a specific voltage signal will generally excite multiple modes propagating in the structure. The response of the same transducer used as receiver to an incoming wave field consisting of the same multiple modes would be equal to the specific voltage signal used for excitation.

Numerical Modelling

Numerical approaches allow for taking into account the coupled electro-mechanical nature of piezoelectric transducers and mechanical interaction between the transducer and the structure. This is important for a quantitative characterization and the practical design of AFC used in SHM systems and for understanding the details of signals measured with AFC. For the simulation of wave propagation phenomena the most common methods are the finite integration technique (FIT, [19], [71]), the finite element method (FEM, [7]) and the finite-difference time domain method (FDTD, [36]). An overview on additional methods and on recent numerical works on wave propagation for NDT is presented in [40]. Only a few publications investigate the Lamb wave propagation caused by piezoelectric transducers including the electro-mechanical coupling of the piezoelectric material ([46], [51], [65]). Greve et al. [28] and Nieuwenhuis et al. [54] compared Giurgiutiu's model [23] to finite element simulations of surface bonded piezoceramic transducers. They found that the frequencies for minima and maxima in the transfer function of the emitter occur at slightly lower frequencies as predicted theoretically. Furthermore, they investigated the response of the piezoceramic transducers to piezo-actuated waves and the results confirmed that the sensor behavior is different to that of the actuator. In most numerical investigations of wave propagation phenomena, the piezoelectric receiver is neglected and a representative value is considered, e.g., surface displacements, since the simulations with electro-mechanical coupling are time consuming. Numerical (and also analytical) investigations of surface bonded AFC/MFC used as emitter and receiver of transient waves and with the consideration of the electro-mechanical coupling have not been reported in the literature to the best knowledge of the author.

Due to the importance of including the electro-mechanical coupling and the transducer-structure interaction and due to the complex design of the AFC a numerical approach is best suited. For the work presented here, the 3D problem is divided into a 2D (including electro-mechanical coupling) and a 3D consideration (without electro-mechanical coupling) due to the limitation of the computational power. But the comparison with experimental results shows that the proposed approach is appropriate for the characterization of the AFC. For this work, the FDTD method was used due to its simplicity of applying it to the complex electro-mechanical governing equations and to the rectangular geometry of the considered system and due to the extensive knowledge and experience at the Institute of Mechanical Systems (e.g., [20], [29], [43]).

Experimental Investigations

Experimental investigations of Lamb wave propagation for damage detection/SHM abound in the literature. As proposed by Veidt et al. for the experimental investigation of the transfer behavior of piezoceramic transducers [81], single point laser interferometry for non-contact measurement of the propagating waves is used for the work presented here. The use of additional optical elements allows to measure all three components of the velocity vector at specific measurement points, which is required for obtaining all present wave modes. The principles of the measurement method used here has been developed over the years at the Institute of Mechanical Systems (e.g., [29], [43]). An overview on laser based Lamb wave detection methods is given in [76].

3.1.3 Transfer Function and Coherence

The transfer function $H(f)$, also called frequency response function, relates the input $x(t)$ and the output $y(t)$ of a linear system and is defined in the frequency domain as [8]

$$H(f) = \frac{G_{xy}(f)}{G_{xx}(f)} \tag{3.4}$$

where G_{xx} is the auto-spectrum density function and G_{xy} is the cross-spectrum density function given by

$$G_{xx} = \frac{2}{T}[X(f) \cdot \overline{X(f)}] \tag{3.5}$$

$$G_{xy} = \frac{2}{T}[Y(f) \cdot \overline{X(f)}] \tag{3.6}$$

for a finite record length T. $X(f)$ and $Y(f)$ represent the Fourier transforms of the input $x(t)$ and the output $y(t)$, respectively, and $\overline{X}$ describes the complex conjugate of X. Thus, the transfer function $H(f)$ describes the answer of the system to an unit excitation in the frequency domain.

If $x(t)$ and $y(t)$ are measured experimentally, noise is present in the signal and the density function and so the transfer function can only be estimated. In order to reduce the random errors, the measurements are repeated n times by assuming that the single experiment is independently repeatable. This allows for obtaining "smooth" estimates $\widehat{G}$ [8] of the density functions given by

$$\widehat{G}_{xx} = \frac{2}{nT} \sum_{i=1}^{n} X_i(f) \cdot \overline{X_i(f)} \tag{3.7}$$

$$\widehat{G}_{xy} = \frac{2}{nT} \sum_{i=1}^{n} Y_i(f) \cdot \overline{X_i(f)} \tag{3.8}$$

The transfer function is then estimated by

$$\widehat{H}(f) = \frac{\widehat{G}_{xy}(f)}{\widehat{G}_{xx}(f)} \tag{3.9}$$

The frequency spectra $X_i(f)$ of each input signal and $Y_i(f)$ of each output signal can be calculated with conventional fast Fourier transform (FFT) techniques.

To obtain the frequency range, where the output correlates to the input signal, the coherence function γ and the confidence interval s of the transfer function can be estimated as $\hat{\gamma}$ and $\hat{s}$, respectively, following [8]

$$\hat{\gamma}_{xy}^2(f) = \frac{\left|\widehat{G}_{xy}(f)\right|^2}{\widehat{G}_{xx}(f) \cdot \widehat{G}_{yy}(f)} \tag{3.10}$$

$$\hat{s}^2(f) = \frac{2}{m-2} \cdot F_{2,m-2,\alpha} \cdot (1 - \hat{\gamma}_{xy}^2(f)) \cdot \frac{\widehat{G}_{yy}(f)}{\widehat{G}_{xx}(f)} \tag{3.11}$$

where $F_{2,m-2,\alpha}$ is the α percentage point for the F distribution function for 2 and $m-2$ degrees of freedom, where m is equal to two times the number of repeated measurements n. The coherence is equal to one for all frequencies, if $n = 1$ or if there are no random errors like noise within the measurement. This is the case for the simulations presented in this work and thus, the coherence analysis is performed only for the experiments.

3.2 Procedure for Simulations and Experiments

Since the transfer function is used for the characterization of the AFC in general, the procedure for its determination as explained in this section is similar for both the numerical and the experimental investigation. For simplification and better identification, simulations and experiments are named with an abbreviation and the reader is referred to Tab. B.1 in App. B, where all geometric parameters are listed in detail. An overview of excitation and measurement positions and an overview of the used excitation signals with their parameters are also presented in App. B

3.2.1 Data Acquisition

Depending whether the AFC is used as emitter or receiver, the input and output signals of the system are defined differently. The definitions as used for both, the simulated and the experimentally estimated transfer functions, are listed in Tab. 3.1.

For the AFC as emitter, the output signal (surface velocity) was recorded at several points around the AFC but at a constant distance. For each point, the transfer function is different. However, by looking at all transfer functions in the same diagram, the radiation can be captured as a function of the frequency. Here, it is assumed that the wave field tends to be circular crested in the far field [64], i.e. in a distance of several wavelengths. For the AFC as receiver, waves were excited at several points around the AFC, i.e. the angle between the front of the incident wave and the fiber direction of the AFC and therefore the output signal changed. Again, this resulted in several transfer functions which allows to characterize the sensitivity as a function of the frequency and direction of the incident wave. The distance

	AFC as emitter	**AFC as receiver**
Input	electrical excitation signal sent to the AFC	undisturbed surface velocity of an incident wave mode at the position of the AFC
Output	surface velocity of the excited wave mode at specific points around the AFC	voltage signal measured with the AFC corresponding to the incident wave mode

Table 3.1: Definition of input and output signals for the determination of the transfer function. The IP or the OoP component of the surface velocity was used for the transfer function of the S_0 or the A_0 mode, respectively.

between excitation point and AFC of several wavelengths allows for assuming plane waves which arrive at the AFC.

It is important to mention that the different wave modes of a plate are not generated directly by the AFC or other transducers. Going into more detail, the transducer just transfers mechanical stresses to the surface of the plate, where elastic bulk waves are excited. After some reflections and mode conversions at the free surfaces of the plate, the modes are more and more developed. Therefore, it is necessary to measure the waves or the output of the system, respectively, at some distances from the source. Hence, the transfer function for the emitter as defined above not only includes the AFC-structure interaction but also the propagation characteristics of the plate, in particular the geometric and material damping between the source and the measurement point. This implies that by changing the distance between the AFC and the measurement point where the surface velocity is obtained, the amplitudes of the transfer function change too. This is different for the case of the AFC as receiver. Here, the input signal is defined as the velocity obtained at the plate surface just at the point where the center of the AFC would be, i.e. it describes the undisturbed wave as if no AFC would be present. The transfer function for the receiver includes again the influences of the AFC-structure interaction. However, by measuring the incident wave and by using the signal as the input of the system, the resulting transfer function does neither depend on the transfer behavior of the transducer used for exciting the waves nor on the distance between the transducer and the AFC.

Contrary to the simulations (see Sec. 3.3.6 for details), it was not possible in the experimental investigations to remove the bonded AFC from the plate for measuring the undisturbed wave. However, beside the assumption of complete isotropy of the aluminum plate, it was assumed that the applied piezoceramic disc transducers (see Sec. 3.4.1 for details) excited the waves with almost perfect rotation symmetry. This assumption was additionally controlled with measurements around the disc transducers. Due to the rotation symmetry of the wave field, the undisturbed wave can be measured in any direction as long as the distance was equal to the distance between the disc transducer and the AFC and as reflections from the plate boundaries did

not affect the wave packet of interest. Fig. 3.1 schematically shows the arrangement of the AFC, disc transducers, and the measurement points. A cylindrical coordinate system (r, φ, x) with the origin at the center of the plate and AFC is introduced. The angle φ starts at a line through the origin in the direction of the fibers of the AFC. It is mentioned here that for the measurement of the undisturbed wave excited by, e.g., the transducer located at (r, φ) = (200, 45°), the transducers located between 0° and 45° have been removed.

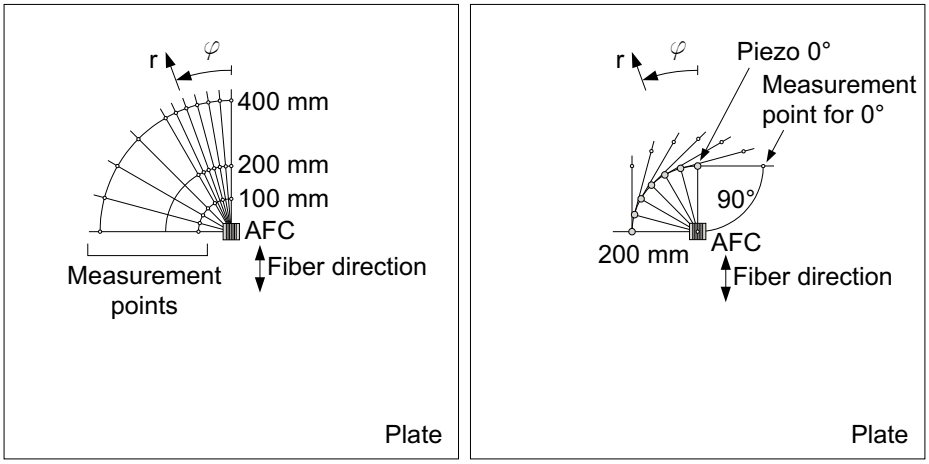

Figure 3.1: Schematic arrangement (not to scale, dimensions in [mm]) of the AFC, piezoceramic transducers, and measurement points for the investigation of the AFC used as emitter (left) and receiver (right). The x-axis of the cylindrical coordinate system (r, φ, x) is perpendicular to r and φ.

3.2.2 Separation of the Wave Modes

For the determination of the transfer function for both fundamental Lamb wave modes, it is necessary to identify each mode in the total wave field and to separate their signals. This was achieved in two ways. First, the waves were excited by a short-time and narrow band excitation pulse (see next section), which leads to a physical separation of the excited modes at some distance from the point of excitation due to the different group velocities. The minimal distance depends on the duration and frequency content of the excitation signal, the latter determines the group velocity of the wave packets. Second, two components of the surface velocity were considered. The radial IP component corresponding to the S_0 wave packet was used for the transfer function of the S_0 mode since the displacements of a surface particle are almost in the plane (see Fig. 2.2). The transfer function for the A_0 mode, however, was determined with the OoP component corresponding to the A_0 wave packet because the largest surface displacements are normal to the plate.

3.2.3 Excitation Signals

When choosing the duration and frequency content of the excitation signal and also the positions of excitation and measurement points, the dispersive character of the A_0 mode and possible reflections at the free boundaries of the plate must be taken into account to achieve a proper separation (see [85], [86]). Due to the limitations given by the available computational hardware (see also Sec. 3.3.5) the geometric dimensions of the aluminum plate were not identical for the simulation and the experiment. Hence, different excitation signals were required for the simulation and the experiment. In order to reduce the effects of the dispersion of the A_0 mode and to achieve the separation, the short-time excitation signal should have a relatively narrow frequency content. This can be achieved with two different types of signals: a sinusoidal tone burst and a linear frequency sweep, both modulated with a Hanning window. For simplification, the first is just called tone burst signal, the second just linear sweep. The use of a linear sweep which starts with the lower frequency has the advantage that the A_0 mode pulse is contracted in time when arriving at the measurement point due to the dispersion – the waves with lower frequencies propagate slower than those with higher frequencies. Another reason for using a linear sweep is the energy, which is distributed between the two limiting frequencies, while for the tone burst signal the energy is concentrated around the center frequency. Thus, the use of the linear sweep resulted in a better signal-to-noise ratio over its frequency range which improved the coherence within the experiments. However, the linear sweep was used only for the experimental investigation of the AFC as emitter, while for all simulations and the experiments for the AFC as receiver tone burst signals were applied. For determining the transfer function over the total frequency range of interest, several excitation signals with overlapping frequency content were needed, otherwise a proper separation of the wave modes could not be achieved. The entire frequency range was chosen from around 20 kHz up to 600 kHz and 800 kHz for the simulations and experiments, respectively, which is a reasonable range for SHM with the guided wave based method.

3.2.4 Data Handling

A Tukey window (often called a cosine-tapered window, see [31]) was superposed on the input and output signal for extracting the wave packet of interest. This was necessary to neglect the influence of the other wave modes and of reflections. By choosing the parameters for the time window it had to be ensured that the wave packet of interest was not affected. Fig. 3.2 shows typical time signals and window functions for the determination of the S_0 transfer function for both the AFC as emitter (left diagrams) and receiver (right diagrams). No window was used for the excitation or input signal, respectively, when the AFC was used as emitter, since the signal was already modulated with a Hanning window. For the case of the AFC as receiver, identical windows were applied for both the input and output signal for determining the transfer function. After the multiplication of the time signals with the window functions, the transfer function was calculated as described

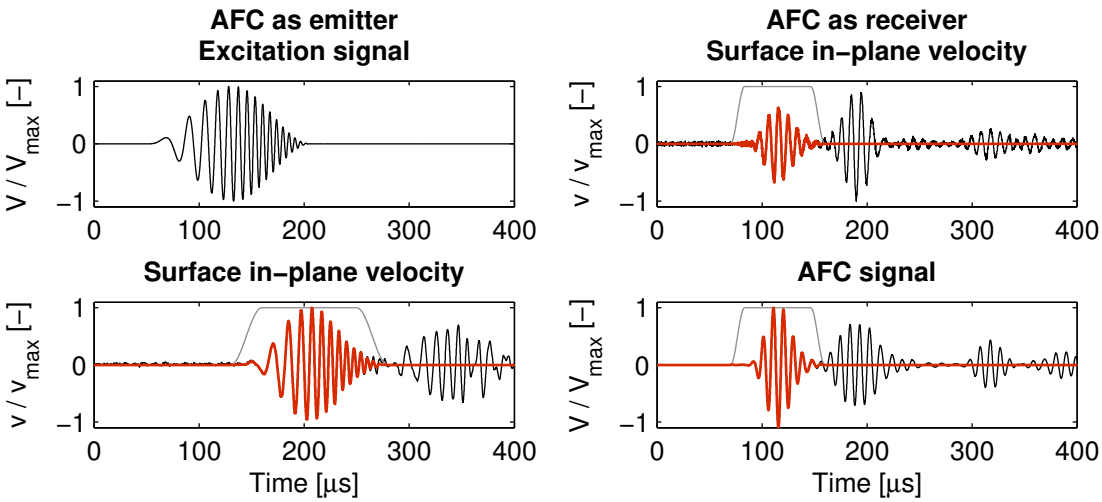

Figure 3.2: Example of typical input (upper diagrams) and output signals (lower diagrams) for the determination of the S_0 transfer function of the AFC used as emitter (left) and receiver (right): original signals (black) and signals (red) after modulation with a time window (gray).

above in Sec. 3.1.3 for both the simulated and experimentally recorded data. By applying the FFT to the time signals (data sets), the resolution in the frequency domain is defined by the number of data points and the sampling rate. Since both parameters were not equal for all data sets, the resolution varied which would yield confusing diagrams if more than one transfer function is depicted. Thus, the FFTs were performed with a constant number of data points much higher than that of the recorded data sets, namely with 2^{16} and 2^{18} points for the experiments and the simulation, respectively. For this so called zero padding [32], the additional data points were set to zero. The frequency resolution was reduced to 152 Hz and 381 Hz for the experiment and simulation, respectively, and the transfer functions appeared as curves which enabled a better identification of individual transfer functions.

Exciting the system (AFC and plate) with several excitation signals results in a respective number of single transfer functions, where each is only valid in the relevant frequency range. The overall transfer function was then determined by compounding the single transfer functions. For the overall transfer function it does not matter which excitation signal was used since the behavior of the system is assumed to be linear within the range of frequencies and amplitudes as used here. The relevant frequency range within the simulation would be equal to the frequency content of the particular excitation signal since there is no noise. However, not the whole frequency range was considered, i.e. frequencies with low amplitudes in the Fourier spectrum of the excitation signal were not taken into account. The relevant frequency range for the experimentally estimated transfer function for the AFC as emitter was related to the range for which the coherence was higher than 0.95 (an example will be given in Sec. 3.4.3). Due to poor signal-to-noise ratio for a few measurements, the frequency ranges for some particular transfer functions were extended to the range where the

coherence was higher than 0.8 (see Fig. C.2). For the investigation of the AFC as receiver, where tone bursts were used for excitation, the frequency range was set to a fixed range around the center frequency (see Tab. B.3). All signal processing was carried out with MATLAB® routines.

3.3 Numerical Modelling

3.3.1 Approach

The wave propagation in the aluminum plate and the transfer behavior of the AFC surface bonded to the plate were investigated in two different numerical models (see also Fig. 3.3):

- A two-dimensional (2D) model simulates the wave propagation in a cross section through the AFC and the plate at the plane of symmetry in fiber direction of the AFC. It corresponds to a state of plane strain. The model takes the electro-mechanical coupling of the piezoelectric material into account which allows for simulating the emitter and receiver behavior of the AFC. For the investigation of the AFC as emitter, the excitation was achieved by applying an electric potential to the electrodes of the AFC. If the AFC is used as receiver, external mechanical loadings were applied for exciting waves which then propagated in the plate.

- A three-dimensional (3D) model then considers only the structure itself but allows for investigating the wave propagation in any direction. The 3D model was used only for the investigation of the AFC as emitter. The excitation was achieved by applying mechanical stresses at the surface of the plate for that area which corresponded to the active area of the AFC. The stresses were taken as the interfacial stresses between the AFC and the plate and were calculated and recorded in the 2D model.

The following description from Sec. 3.3.2 to 3.3.4 refers to the 2D model which includes the piezoelectric element with the electro-mechanical coupling. However, the governing equations in Sec. 3.3.3 are presented generally in 3D. The numerical algorithm for the 3D model is exactly the same as for the aluminum plate in the 2D model. The plate in the 3D model is described with the fully 3D equations of elasticity. In Sec. 3.3.5 the combination of the 2D and 3D model is then described. All simulations were carried out with MATLAB®.

3.3.2 Assumptions

Since the present wavelengths are much larger than the dimensions of the IDE, the complex electrode design of the AFC can be simplified in the 2D model with respect to simulating similar global deformations within the AFC with and without IDE. Therefore, the two electrodes are set on the front side of the piezoelectric

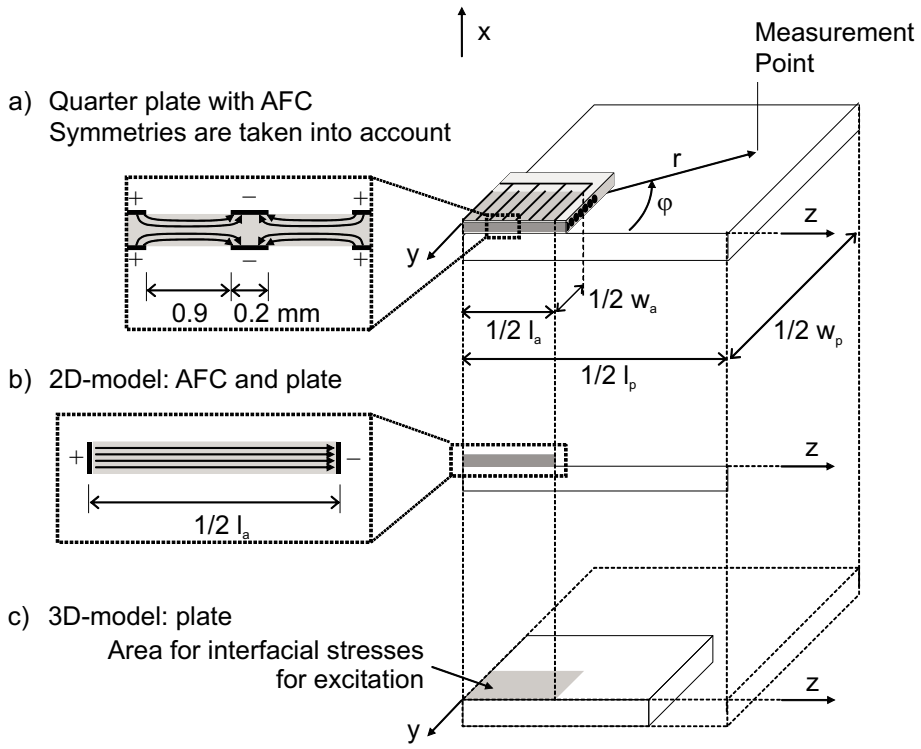

Figure 3.3: Schematics (not to scale) of a) a quarter of the surface bonded AFC and the aluminum plate with respect to the symmetries and a detail of the electric field within the AFC, b) the 2D model with a detail of the electric field as assumed for the simulation, and c) the 3D model with the area where the stress distribution for the excitation is applied (see Sec. 3.3.5 for details).

element (see Fig. 3.3). The length of the modeled AFC and, hence, the electrode spacing, corresponds to the active length l_a of the AFC in the experiment. The different spacing q between the electrodes in the simulation and the experiment leads to a different ratio of the electric field E within the piezoelectric material and the electric voltage V at the electrodes ($V = E \cdot q$). However, for a quantitative comparison of the simulation with the experiment, the electric field has to be equal for both. Consequently, the electric voltage within the simulation has to be adjusted as follows. If the AFC is simulated as an emitter, the voltage for excitation has to be multiplied by the factor $\xi = q_{sim}/q_{IDE}$, where $q_{sim} = \frac{l_a}{2}$ (only the half of the active length due to the symmetry) and q_{IDE} corresponds to the spacing between two fingers of the IDE (0.9 mm for the standard design). For the AFC as receiver, the electric field as calculated in the simulation corresponds to that obtained within the experiment. Therefore, the simulated electric voltage at the electrodes has to be divided by $\xi^* = q^*_{sim}/q_{IDE}$, where $q^*_{sim} = l_a$. It is mentioned in advance that the model is linear since all equations used are linear. This allows for performing a simulation with an excitation with a normalized amplitude and multiplying the results afterwords by the required factor.

The AFC in the model is assumed to be homogeneous. This seems reasonable, since the present wavelengths are much larger than the dimensions of the electrodes and the cross section of the fibers. The material is linear and transversely-isotropic in the elastic, dielectric and piezoelectric parameters since the Kapton foil is neglected. The properties are chosen similar to the global properties as listed in Tab. 2.1 on page 18. The aluminum plate is assumed to be linear elastic, isotropic and homogeneous (elastic modulus E = 68.9 GPa, Poisson's ratio $\nu = 0.33$, density $\rho = 2700$ kg/m^3, according to the plate used for the experimental investigations).

The coupling between the piezoelectric element and the structure is assumed to be ideal without the presence of any bonding layer. This is reasonable since the layer is thin compared to the thickness of the AFC and the matrix of the AFC and the adhesive consist both of epoxy resin. Energy dissipation in the piezoelectric material and in the aluminum is neglected. Symmetries are taken into account for the simulation of the AFC as emitter to reduce the simulation time. There are no symmetries for the case of the AFC as receiver.

3.3.3 Governing Equations

To fully describe the dynamical behavior of a linear elastic material, the equation of motion, the kinematic and the constitutive relations are needed. Due to the rectangular form of the AFC a cartesian coordinate system is introduced for both the 2D and 3D model. The x-axis is normal to the plane of the plate and the z-axis is aligned along the fiber direction of the AFC. The origin is on the interface AFC-plate in the center of the AFC (see Fig. 3.3).

By neglecting external body forces, the stress equations of motion are given as:

$$\rho \cdot \ddot{\mathbf{u}} = \nabla \cdot \boldsymbol{\sigma} \tag{3.12}$$

where ρ is the density, $\mathbf{u}$ the displacement vector and $\boldsymbol{\sigma}$ the stress tensor (see also Sec. 2.4.1). The stresses $\boldsymbol{\sigma}$ and the strains $\boldsymbol{\epsilon}$ are related by the linear kinematic relations

$$\boldsymbol{\epsilon} = \mathcal{L} \cdot \mathbf{u} \tag{3.13}$$

where $\mathcal{L}$ is a matrix of spatial derivative operators given as

$$\mathcal{L} = \begin{bmatrix} \frac{\partial}{\partial x} & 0 & 0 \\ 0 & \frac{\partial}{\partial y} & 0 \\ 0 & 0 & \frac{\partial}{\partial y} \\ 0 & \frac{1}{2}\frac{\partial}{\partial z} & \frac{1}{2}\frac{\partial}{\partial y} \\ \frac{1}{2}\frac{\partial}{\partial z} & 0 & \frac{1}{2}\frac{\partial}{\partial x} \\ \frac{1}{2}\frac{\partial}{\partial y} & \frac{1}{2}\frac{\partial}{\partial x} & 0 \end{bmatrix} \tag{3.14}$$

The constitutive relations for piezoelectric material (see Eq. 2.4 and 2.5) are

$$\begin{aligned} \boldsymbol{\sigma} &= \mathbf{C}^{\mathbf{E}} \cdot \boldsymbol{\epsilon} - \boldsymbol{e} \cdot \mathbf{E} \\ \mathbf{D} &= \boldsymbol{e} \cdot \boldsymbol{\epsilon} + \boldsymbol{\varepsilon}^{\boldsymbol{\epsilon}} \cdot \mathbf{E} \end{aligned}$$

and for non-piezoelectric material are

$$\boldsymbol{\sigma} = \mathbf{C} \cdot \boldsymbol{\epsilon} \tag{3.15}$$

The stiffness tensor $\mathbf{C}$ for isotropic, linear elastic material is given as

$$\mathbf{C} = \begin{bmatrix} \lambda + 2\mu & \lambda & \lambda & 0 & 0 & 0 \\ \lambda & \lambda + 2\mu & \lambda & 0 & 0 & 0 \\ \lambda & \lambda & \lambda + 2\mu & 0 & 0 & 0 \\ 0 & 0 & 0 & \mu & 0 & 0 \\ 0 & 0 & 0 & 0 & \mu & 0 \\ 0 & 0 & 0 & 0 & 0 & \mu \end{bmatrix} \tag{3.16}$$

where λ and μ are the Lamé constants.

Due to the coupling of electrical and mechanical fields, two other equations for the piezoelectric material must be satisfied. First, the divergence of the electric displacement $\mathbf{D}$ must vanish

$$\nabla \cdot \mathbf{D} = 0 \tag{3.17}$$

since there are no free charges within the piezoelectric element [66]. Second, the quasi static potential equation

$$\mathbf{E} = -\nabla \Phi \tag{3.18}$$

where $\mathbf{E}$ is the electric field vector and Φ the electric potential (scalar field), is valid, because the electric waves propagate by a factor of 10^4 to 10^5 faster than the mechanical waves [66].

Beside the governing equations boundary conditions must be satisfied. It is assumed that the model is surrounded by vacuum. This leads to the following mechanical boundary conditions which must be fulfilled for all times. The indices 'n' and 't' define the normal direction to the corresponding surface and the tangential direction, respectively, i.e. in the 3D model the t-direction is associated with two tangential directions perpendicular to each other:

- free boundary conditions

$$\begin{aligned} \sigma_{nn} &= 0 \\ \sigma_{nt} &= 0 \end{aligned} \tag{3.19}$$

- symmetry conditions

$$\begin{aligned} u_n &= 0 \\ \sigma_{nt} &= 0 \end{aligned} \tag{3.20}$$

- interfacial conditions

$$\begin{aligned} u_n^{AFC} &= u_n^{Plate} \\ u_t^{AFC} &= u_t^{Plate} \\ \sigma_{nn}^{AFC} &= \sigma_{nn}^{Plate} \\ \sigma_{nt}^{AFC} &= \sigma_{nt}^{Plate} \end{aligned} \tag{3.21}$$

If the AFC is used as receiver, external mechanical stresses are applied on one edge of the aluminum plate to excite plane propagating wave modes:

- conditions for exciting a S_0 mode

$$\begin{aligned} \sigma_{nn} &= \begin{cases} \sigma(t) & \text{if } t < t_{excitation} \\ 0 & \text{else} \end{cases} \\ \sigma_{nt} &= 0 \end{aligned} \tag{3.22}$$

  where $\sigma(t)$ corresponds to the excitation.

- conditions for exciting an A_0 mode

$$\begin{aligned} \sigma_{nn} &= 0 \\ \sigma_{nt} &= \begin{cases} \sigma(t) & \text{if } t < t_{excitation} \\ 0 & \text{else} \end{cases} \end{aligned} \tag{3.23}$$

  where $\sigma(t)$ corresponds to the excitation.

For the piezoelectric material electrical boundary conditions are additionally needed to get the complete solution. These conditions depend on whether the AFC is used as emitter or as receiver. For the latter, an electrical open-circuit is assumed:

- electrically free boundary conditions, where no electrode is defined

$$D_n = 0 \tag{3.24}$$

- symmetry conditions needed for the AFC as emitter or electrically grounded electrode needed for the AFC as receiver (left electrode of the AFC in Fig. 3.3)

$$\Phi = 0 \tag{3.25}$$

- electrical excitation at the electrode needed for AFC as emitter (right electrode)

$$\Phi = \begin{cases} \phi(t) & \text{if } t < t_{excitation} \\ 0 & \text{else} \end{cases} \tag{3.26}$$

  where $\phi(t)$ is the excitation signal.

- equipotential condition at the right electrode needed for AFC as receiver

$$\begin{aligned} \Phi &= \text{constant} \\ \int_A D_n \cdot dA &= 0 \end{aligned} \tag{3.27}$$

  where A is the area of the electrode.

At last, the initial conditions for the entire piezo element and the aluminum plate are set as

$$\begin{aligned} \mathbf{u}(t)|_{t=0} &= 0 \\ \dot{\mathbf{u}}(t)|_{t=0} &= 0 \\ \boldsymbol{\sigma}|_{t=0} &= 0 \\ \Phi(t)|_{t=0} &= 0 \end{aligned} \tag{3.28}$$

Due to the plane strain state assumed for the 2D model, all terms with $(\dots)_y$ and $\frac{\partial}{\partial y}(\dots)$ can be set to zero.

3.3.4 Numerical Implementation

The principle of the FDTD method is to approximate the partial derivatives of the above mentioned equations with central finite differences. For this, the spatial continuum is discretized into a grid with cells of the dimension Δx, Δy and Δz. Further, the time continuum is divided into time steps Δt. A staggered grid is used for the spatial domain. In other words, the derivative of a variable is set halfway between the two grid points where the variable itself is defined. An allocation of the variables as shown in Fig. 3.4 follows. If a variable is needed between two grid points, its value has to be averaged. In the time domain, however, a staggered grid is not required for a stable algorithm [30]. The governing equations and boundary conditions have to be fulfilled in each grid cell and for each time step which leads to a number of linear equations equal to the number of the degrees of freedom.

The finite differences for the approximation of the first and second derivatives can be derived with the help of the Taylor expansions with an error of second order. This will lead to a second order accurate algorithm in space and time. Hence, the approximated derivatives of a function $f(s)$ at $s = s_0$ are given for a staggered grid as

$$\left.\frac{\partial f(s)}{\partial s}\right|_{s=s_0} = \frac{f(s_0 + \Delta s/2) - f(s_0 - \Delta s/2)}{\Delta s} + O(\Delta s^2) \tag{3.29}$$

and

$$\left.\frac{\partial^2 f(s)}{\partial s^2}\right|_{s=s_0} = \frac{f(s_0 + \Delta s) - 2 \cdot f(s_0) + f(s_0 - \Delta s)}{\Delta s^2} + O(\Delta s^2) \tag{3.30}$$

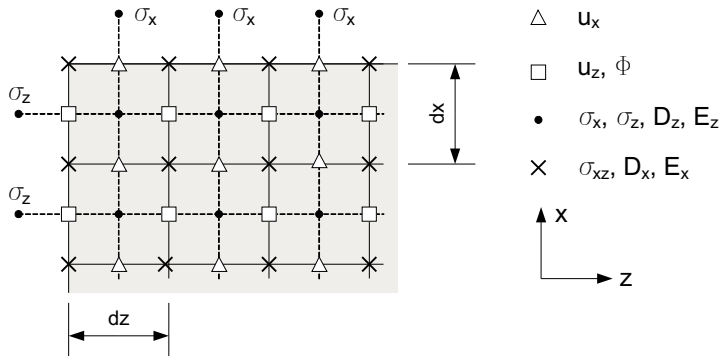

Figure 3.4: Allocation of the displacement, stress, and electrical components on a staggered grid for the piezoelectric element within the 2D model. The depicted section corresponds to the left upper corner of the cross section through the piezoelectric element.

It has to be mentioned that Eq. (3.30) is valid whether the grid is staggered or not. A consequence of the use of a staggered grid is the introduction of so called ghost points. These points are placed outside the geometric boundary of the element in a distance of half of the cell size. They help to fulfill the boundary conditions and are, hence, only needed for variables, which are not directly located on the boundary. A more detailed description of the discretization and the order of accuracy of the algorithm can be found in the work of Gsell [29] and Leutenegger [43], respectively.

For both the 2D and 3D model the algorithm (see Fig. 3.5) starts with the definition of all required parameters, the initialization of the variables and the discretization of the structure. After the stability check (see page 38) the time loop is carried out wherein all time dependent variables are calculated for each time step.

The time loop starts with the calculation of the electric potential within the piezoelectric material. For it, Eq. (3.18) and (3.13) are substituted into the constitutive relation Eq. (2.5) before Eq. (3.17) is applied. This leads to a Poisson's equation for the electric potential Φ. The substitution of the partial derivatives according to Eq. (3.29) and (3.30) yields an implicit linear system of equation of the form

$$\mathbf{A} \cdot \widetilde{\Phi} = \mathbf{b} \tag{3.31}$$

The time invariant Matrix $\mathbf{A}$ depends only on the dimensions, material parameters and the mechanical and electrical boundary conditions of the piezoelectric element, the latter differs depending on whether the element is used as emitter or receiver. The size of the matrix $\mathbf{A}$ is $m \times m$, where m is equal to the product of the numbers of grid points along the length and thickness of the AFC. For simple geometries $\mathbf{A}$ is well-conditioned and Eq. (3.31) can be solved by a matrix inversion, which must be calculated only once at the beginning of the simulation. The vector $\widetilde{\Phi}$ represents the electric potential to be solved for. The vector $\mathbf{b}$ then contains material parameters, boundary conditions and the actual displacement field $\mathbf{u}$ within the element. It contains also the given electric potential at the electrodes if the AFC is used as

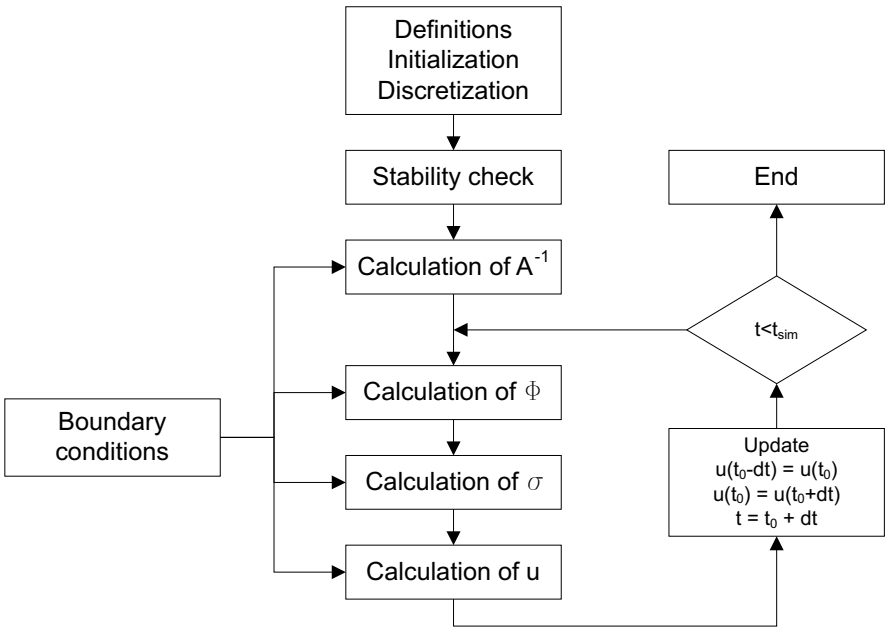

Figure 3.5: Diagram of the major steps of the algorithm for the 2D model with consideration of the electro-mechanical coupling within the piezoelectric material.

emitter (Eq. (3.26)). For fulfilling the equipotential boundary condition (Eq. (3.27)) when the AFC is used as receiver, the dielectric displacements D_z on the boundary are needed. This is achieved by a linear extrapolation in z-direction with the values at the two inner points where D_z is defined (see Fig. 3.4). Special attention is also needed for fulfilling the interfacial conditions between the piezoelectric element and the aluminum plate to guarantee the correct coupling.

The next step in the algorithm is the computation of the mechanical stress components of the piezoelectric element in terms of the actual displacements and the electric potential. From Eq. (3.13) and Eq. (2.4) an explicit linear equation is obtained as

$$\boldsymbol{\sigma} = \mathbf{C}^{\mathbf{E}} \cdot \mathcal{L} \cdot \mathbf{u} + \boldsymbol{e} \cdot \nabla\Phi \tag{3.32}$$

The mechanical stress components of the aluminum plate are derived from Eq. (3.13) and (3.15) as

$$\boldsymbol{\sigma} = \mathbf{C} \cdot \mathcal{L} \cdot \mathbf{u} \tag{3.33}$$

By substituting the partial derivatives with the central differences and by applying the mechanical boundary conditions, which include the coupling between the piezoelectric element and the plate, all stress components within each grid cell are determined. If the AFC is used as receiver, the mechanical boundary conditions for one edge of the plate contains the external mechanical stresses used for exciting the required wave mode (see Eq. (3.22) and (3.23)).

The discretized equation of motion, Eq. (3.12) for both the piezoelectric element and the plate, can then be solved for the displacements at the time $t = t_0 + \Delta t$ in terms of the actual displacements ($t = t_0$), the old displacements ($t = t_0 - \Delta t$) and

the actual stresses.

At the end of the time step, the displacements are updated for the next time step as depicted in Fig. 3.5. The loop stops as soon as the given duration of the simulation is reached.

The stability check contains two criteria for the discretization parameters in space (Δx, Δy and Δz) and time (Δt) which must be satisfied in order to guarantee accurate solutions and numerical stability of the algorithm. First, there must be enough spatial grid cells within the shortest wavelength λ_{min} appearing in the simulation. A commonly used value for a sufficient spatial sampling rate is given by

$$\frac{\lambda_{min}}{max(\Delta x, \Delta y, \Delta z)} \geq 8 \tag{3.34}$$

The shortest wavelength is obtained within the piezoelectric material. It is derived from $\lambda_{min} = c_{min}/f_{max}$, with $c_{min} = \sqrt{min(c_{ij})/\rho}$ as the minimal phase velocity calculated with the smallest component c_{ij} (with $ij = 11, 33, 44, 66$) of the stiffness tensor $\mathbf{C^E}$ and with f_{max} as the highest frequency within the simulation. It was obtained from simulations that for a stable algorithm the sampling rate has to be increased to more than twenty grid points per minimal wavelength, which is recommended also in the literature (see [29]). One reason for it is the numerical dispersion, a spatial aliasing error which causes phase and group velocities to become functions of the discretization parameters [43]. Another reason is the insufficient number of grid points over the relatively small thickness of the AFC when Eq. (3.34) is applied. The grid size in the 3D model can be enlarged due to the absence of the piezoelectric material. The phase velocity c_2 of the shear bulk wave in the aluminum is used here for calculating the minimal wavelength. Again, more than twenty grid points per minimal wavelength are chosen. For all simulations presented in this work the spatial discretization parameters are set to $\Delta x = \Delta z = 0.05$ mm for the 2D model (AFC and plate) and $\Delta x = \Delta y = \Delta z = 0.2$ mm for the 3D model.

The second criterion concerns the time step Δt. The time step has to be smaller than the time needed by the physical wave to propagate from one grid point to the next. For cartesian coordinates the criterion is derived by [19] as

$$\Delta t \leq \frac{1}{c_{max} \cdot \sqrt{\frac{1}{\Delta x^2} + \frac{1}{\Delta y^2} + \frac{1}{\Delta z^2}}} \tag{3.35}$$

where c_{max} is equal to the phase velocity c_1 of the dilatational bulk wave in aluminum. It can be seen that by decreasing the spatial discretization for obtaining a more accurate algorithm, the temporal discretization has to be decreased too, which results in an extension of the time needed for computing. The time step was set to 5 ns and 10 ns for the 2D and the 3D simulations, respectively.

A possibility to test the accuracy of the algorithm is to observe the total energy during the simulation. Since any energy dissipation and radiation into surroundings is neglected in the model, the total energy must remain constant with time after excitation. The total energy for non-piezoelectric material is the sum of the kinetic

and potential energy densities integrated over the entire volume of the structure. For piezoelectric material it is more complex due to the coupling of mechanical and electrical energy and the augmentation of the potential energy by the presence of piezoelectricity [66]. For the simulations presented here, the total energy is computed only for the aluminum plate (see example in Sec. 3.3.6). However, this is sufficient because of the coupling of the piezoelectric element with the aluminum plate: an augmentation, e.g., of the total energy of the piezoelectric element would have an influence on the total energy of the plate since the energy would be radiated into the plate and thus would indicate instability.

3.3.5 Combination of the 2D and 3D Model

As mentioned in Sec. 3.3.1 the 3D model depicts only the aluminum plate and the piezoelectric element is neglected. One reason why the AFC is not modelled in 3D is the huge number of grid cells needed. Due to the discretization criteria mentioned in the former section and the small thickness of the AFC, a very fine grid would be necessary. With the relatively large length and width of the AFC the number of cells and, in particular, the inversion of the matrix $\mathbf{A}$ needed for the calculation of the electric potential would exceed the limit given by the available computational hardware.

To achieve an excitation of the 3D model which corresponds to the excitation by the AFC, the interfacial normal stresses σ_{xx} and shear stresses σ_{xz} between the AFC and the plate as obtained within the 2D simulations are used. The stresses are recorded and saved during the 2D simulations, thus the 3D simulations can be performed consecutively. The time dependent stress distributions are applied at the surface of the plate for the entire area, which corresponds to the active area of the AFC. It is assumed that the presence of the two edges of the AFC parallel to the z-direction has only a small influence on these stress distributions in the y-direction. Hence, the stresses are constant in this direction. Further, it is assumed that the shear stresses σ_{xy} perpendicular to the fiber direction can be neglected. This seems appropriate due to the presence of the epoxy matrix between the piezoelectric fibers, which are aligned in the z-direction.

The cell size for the 3D model can be enlarged compared to the 2D model since the discretization criteria are still fulfilled for the aluminum. This helps to reduce the number of grid cells or enables to simulate larger structures. Changing the cell size requires an adaption of the discrete interfacial stress distributions in order to fulfill the equilibrium of the forces. This can be handled by multiplying the interfacial stress components from the 2D simulation with the 2D cell size, building the sum over the length of a 3D cell, and dividing it through the length of the 3D cell. This also guarantees that extreme peaks, particularly at the edge of the piezoelectric element, are not lost due to the choice of a wider grid.

Even with the enlargement of the cell size and the consideration of symmetries, it was not possible to simulate the plate with similar dimensions as used in the experiments due the limited number of cells. Therefore, the length and the width of the

3D model are reduced compared to the experiment. As a result, the wave field will be different after reflections occur at the free boundaries of the plate. A possibility to avoid the unwanted reflections in the simulation would be the implementation of absorbing boundary conditions. In the present work, such conditions were not used due to the high effort needed for programming the code in 3D, in particular at the corners of the plate. Instead, the dimensions of the plate are chosen as large as possible and adequate excitation signals are applied, which enables obtaining useful results.

3.3.6 Examples of the Simulations

AFC as Emitter

Within the first example (2DE1-3DE1, see Tab.B.1) the AFC used as emitter had a thickness of 0.3 mm and an active area with a length of 31 mm and a width of 20 mm. The Aluminum plate had a thickness of 1 mm, a length of 1,500 mm and 500 mm in the 2D and 3D model, respectively, and a width of 300 mm (all dimensions without symmetries). The AFC was placed in the center of the plate. The material parameters for the AFC are listed in Tab. 2.1.

The excitation was achieved by defining the electric potential at the electrodes of the AFC in the 2D model. The signal corresponded to a 3.5 cycle sinusoidal tone burst modulated by a Hanning window with a center frequency of 200 kHz. This frequency is far below the first cut-off frequencies of higher wave modes, i.e. only the S_0, A_0 and the SH_0 mode can exist.

The interfacial normal and shear stresses transferred from the AFC to the plate during excitation as calculated in the 2D model are shown in Fig. 3.6 for one specific time step. At this time, the AFC is expanded maximally and the shear stresses at the plate surface transferred from the AFC are in positive z-direction. Simultaneously, pressure at the edge of the AFC can be obtained due to the bending stiffness of the expanding AFC. Normal and shear stresses are concentrated as expected at the edge of the AFC.

The interfacial stresses were then applied at the surface of the plate of the 3D model for the entire area, which corresponds to the active area of the AFC. Fig. 3.7 qualitatively shows the total displacements $u = \sqrt{u_x^2 + u_y^2 + u_z^2}$ at the surface of the plate for several time steps simulated now with the 3D model. By showing the total displacements, all propagating modes appear and can be identified by looking at the main direction of the particle velocity at a single point (see Fig. 3.8) and by comparing the group velocities with the theoretical values. The fastest wave packet with the largest wavelength is the S_0 mode. The direction of the particle velocity is mainly radial and IP, i.e. in propagation direction, as it can be seen in Fig. 3.8. The diagonally radiated wave packet corresponds to the SH_0 mode with tangential IP velocities. In the y- and z-direction, the SH_0 mode does not exist because of the symmetry conditions. In a direction of about 50° from the fiber direction of the AFC, the amplitudes of the SH_0 mode are minimal. The reason for this is the destructive interference of the waves which are mainly excited at either end of the

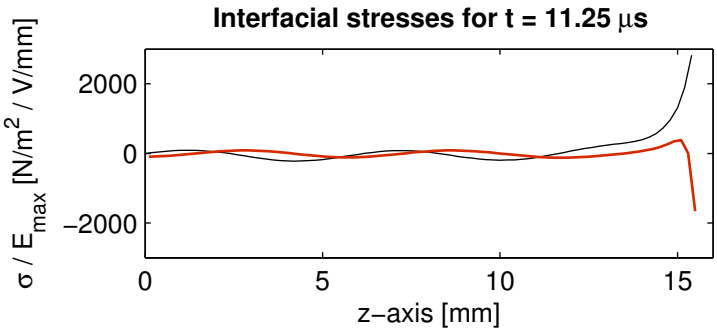

Figure 3.6: Interfacial normal (red) and shear (black) stress distributions between the AFC and the aluminum plate along one half of the AFC length during electrical voltage excitation (3.5 cycle sinusoidal tone burst, Hanning window, center frequency of 200 kHz) calculated with the 2D model (2DE1, see Tab. B.1). The stresses are scaled by the maximal electric field during excitation. At the time $t = 11.25$ μs, the AFC is expanded maximally.

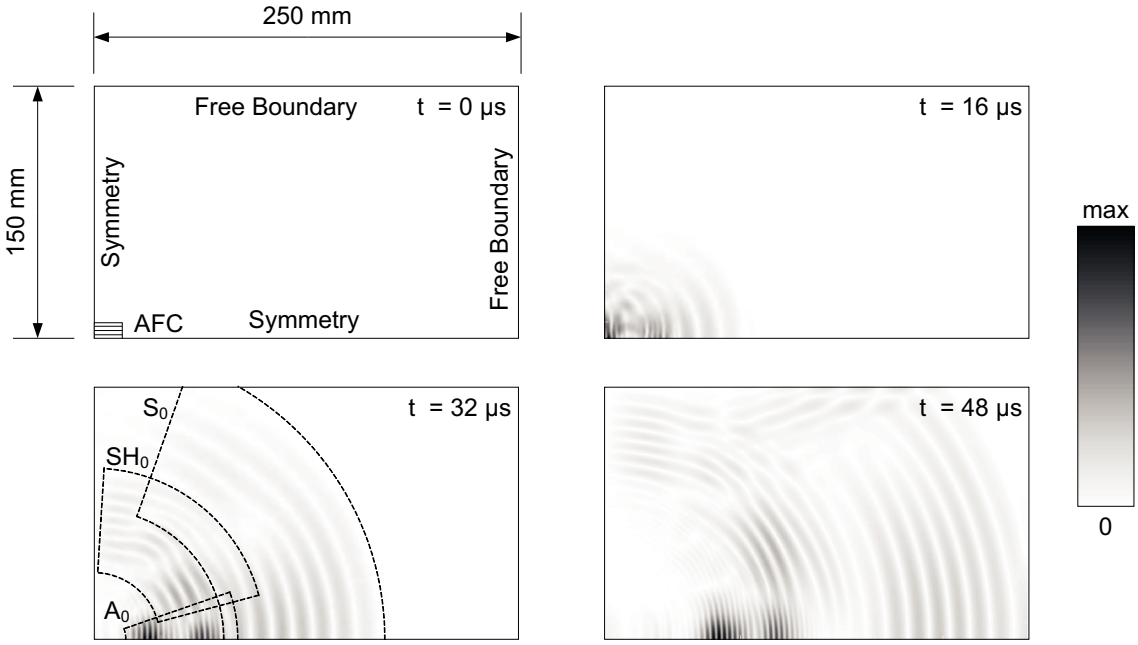

Figure 3.7: Total displacements at the surface of the quarter-plate for different time steps simulated by the 3D model (2DE1-3DE1). The rectangle at the lower left corner of the picture at $t = 0$ μs indicates the position and the fiber direction of a quarter of the AFC used as emitter, where the normal and shear stresses for excitation were applied. The excitation corresponded to a 3.5-cycle sinusoidal tone burst in a Hanning window at a center frequency of 200 kHz.

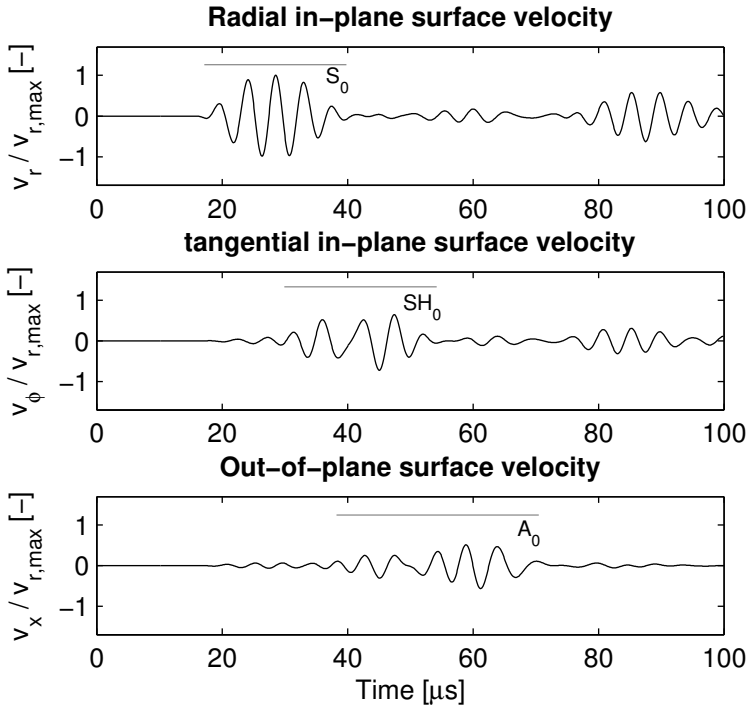

Figure 3.8: Radial IP (top), tangential IP (middle), and OoP (bottom) surface velocities at $(r, \varphi) = (100, 15°)$ for the 3D simulation (2DE1-3DE1) as shown in Fig. 3.7.

AFC due to the typical stress distribution. The wave with the smallest wavelength corresponds then to the A_0 mode with mainly OoP velocities. Two A_0 mode wave packets can be seen. This is reasonable since the two wave packets which are mainly excited at the two ends of the AFC are not completely superposed due to the small wavelength and the short duration of the excitation. Further, the second A_0 wave packet has larger amplitudes than the first one. On the one hand, the two wave packets have not to be identical since the first one has travelled only in an area of the plate with free boundary conditions while the second one has passed the area below the AFC. On the other hand, the dispersion results in a distorted wave form which has not to be symmetric anymore and, hence, the superposition of the two packets neither. A comparison between simulated and experimentally estimated results will be presented in Sec. 3.5.

AFC as Receiver

The second example (2DR1) treats the AFC as a receiver. Again, the length and the thickness of the AFC were 31 mm and 0.3 mm, respectively, and the thickness of the Aluminum plate was 1 mm. The length of the plate was now 700 mm and the AFC was placed 200 mm from the left edge of the plate, where external mechanical stresses were applied for exciting waves (see Fig. 3.9). The length of the plate was chosen as small as possible for reducing the simulation time, but in such a way

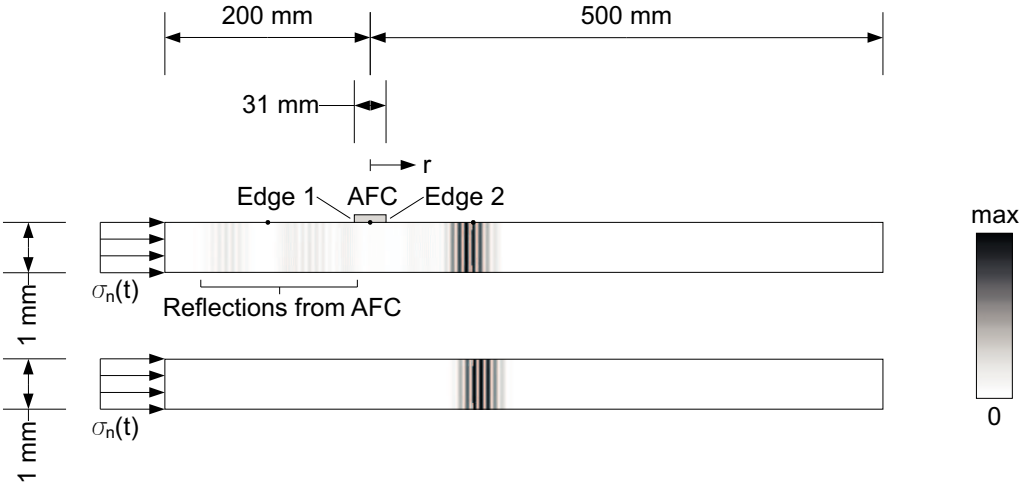

Figure 3.9: Total displacements calculated with the 2D model (2DR1) in a cross section of an aluminum plate with (top) and without (bottom) surface bonded AFC used as receiver 64 μs after the initiation of the excitation. The S_0 mode was excited at 400 kHz (5 cycle tone burst with a Hanning window) by applying normal stresses on the left front side of the plate. The three small dots on the surface of the plate (top) indicates the position where the surface velocities are recorded (see next figure). The plate's thickness is enlarged for better visualization.

that any reflections of waves did not disturb the sensing process of the wave packet, which arrives first at the AFC. It was therefore also of advantage to excite only one single mode. Within this example, normal stresses acting on the left front side of the plate were used to excite the S_0 mode. By applying shear stresses, an A_0 mode would be excited. The excitation signal corresponds to a 5-cycle sinusoidal tone burst modulated by a Hanning window with a center frequency of 400 kHz.

Beside this model, which takes the AFC into account, a similar simulation without the AFC was performed. This model allows for simulating the undisturbed deformation fields of the propagating wave. The comparison of the two models enables to investigate the influence of the AFC on the wave propagation in the plate. Fig. 3.9 shows the total displacements of both simulations, with and without the AFC, after the wave packet passes the AFC. Reflections at the AFC can clearly be seen. Further, the wave velocity of the incoming wave packet was slightly decreased underneath the AFC. Therefore, a small time delay compared to the undisturbed propagation can be observed for the transmitted S_0 wave packet.

The consideration of the time histories of the particle velocities at several points along the surface of the plate enables the identification of the reflected and converted wave modes (see Fig. 3.10). It is obvious that reflections and conversions occur at both edges of the AFC, where the mechanical boundary conditions for the plate change immediately. Hence, there are two reflected S_0 and two reflected A_0 modes. The two transmitted A_0 modes superpose each other and appear as one wave packet. The reflections and conversions explain why the duration of the wave pulse observed

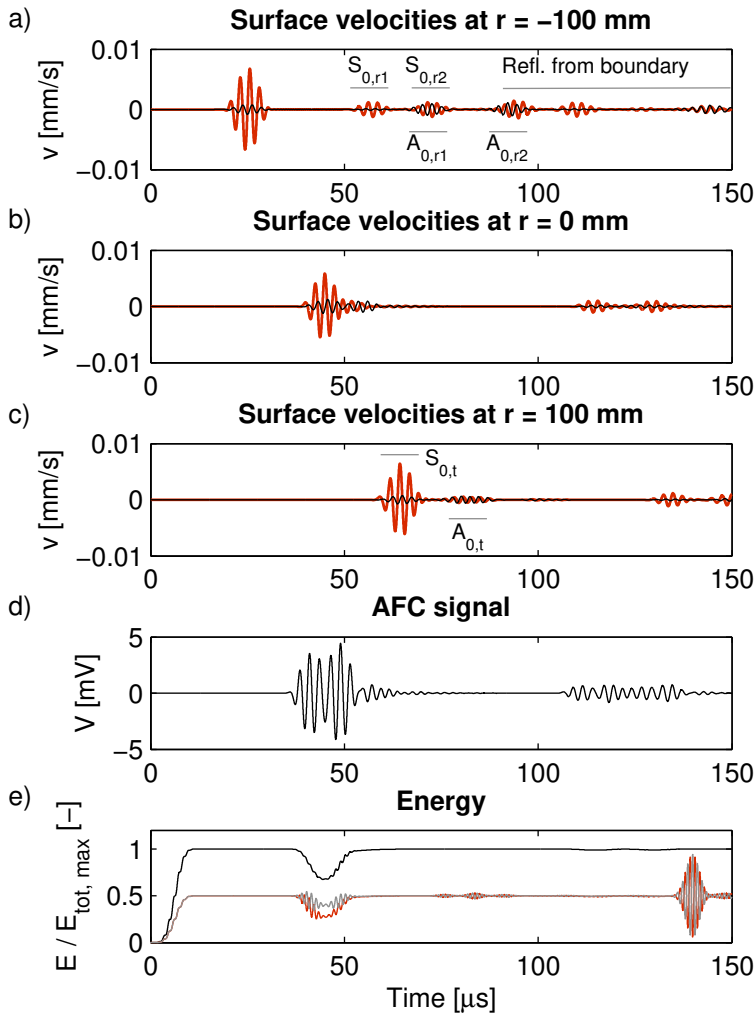

Figure 3.10: Results from the simulation with the 2D model (2DR1) with surface bonded AFC: a)-c) IP (red) and OoP (black) surface velocities 100 mm in front of the AFC, at the center of the AFC, and 100 mm behind the AFC, respectively, d) AFC voltage signal, and e) total, potential, and kinetic energy (black, gray, and red, respectively). A S_0 mode was excited at 400 kHz (5 cycle tone burst with a Hanning window). The indices 'r1' and 'r2' indicates the reflected waves from the two edges of the AFC, the index 't' denotes the transmitted waves.

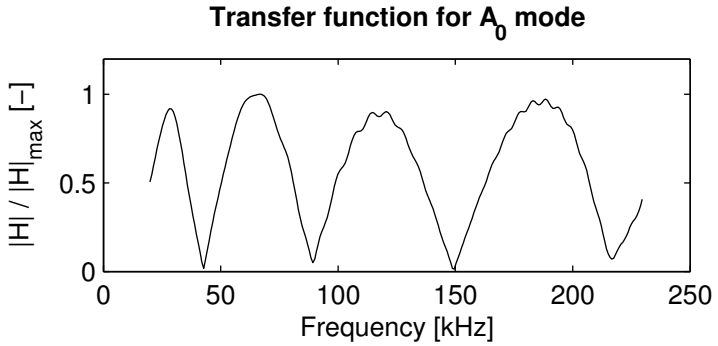

Figure 3.11: Example of a transfer function of the AFC as emitter for the A_0 mode simulated with the 2D model (2DE1). The excitation signal was a linear frequency sweep from 5 kHz to 250 kHz (see Tab. B.3) and the OoP surface velocity was recorded at $(r, \varphi) = (400, 0°)$.

in the time history of the electric voltage is much longer than the original incoming wave. Although the reflections and conversions have much smaller amplitudes than the transmitted S_0 mode, two well marked wave pulses with comparable maximal amplitudes can be seen in the electric voltage signal. The time difference between the two packets corresponds to the time needed by the wave for travelling along the length of the AFC. Conclusively, changes in the electric voltage occur mainly when the wave packet passes the edges of the AFC. The appearance of two wave packets can only be seen if the length of the incoming wave packet is small compared to the length of the AFC. The total energy of the aluminum plate is shown in the same figure. After the excitation the total energy remains constant as long as no wave packet passes the AFC. The energy transferred to the AFC (from 35 μs to around 70 μs) is completely radiated back into the plate. Reflections of waves at the edges of the plate lead to the variations in the kinetic and potential energy while the total energy remains constant (from 135 μs to 144 μs).

3.3.7 Sensitivity Analysis

The model as programmed here has several free variables. Beside all geometric dimensions the material parameters enter the simulation. Therefore, the sensitivity of the result due to variations of each parameter was investigated in the 2D model. It is obvious that by varying the geometric dimensions, in particular the length of the AFC and the plate thickness, the results differ due to the changed ratio of the length of the propagating wave modes and the length of the AFC. More interesting is to vary the stiffness, piezoelectric and dielectric parameters of the AFC. For this reason, a 2D simulation of the AFC as emitter (2DE1) was performed first with standard parameters (see Tab. 2.1) before individually changing each parameter and running the simulation again. Each parameter was reduced and augmented within the range of 10% to the standard value.

To point out the changes in the results, the transfer functions of the emitter

in the frequency domain were determined separately for the S_0 and the A_0 mode. Fig. 3.11 shows a typical transfer function for the A_0 mode with the minima and maxima as expected from theory (tuning effects [23]). By varying parameters, deviations were obtained for the amplitude of the transfer function and for the position of the minima and maxima. The evaluation shows that for most parameters by looking at any frequency, the deviations are almost linear over the range of variation. Also the sign of the deviations remains the same over the considered frequency range. There are some exceptions but their deviations are negligible. However, a quantification which is valid for the whole frequency range was not possible due to the complex electro-mechanical coupling behavior and the dispersive character of the Lamb waves. Thus, the influence of each parameter was evaluated only qualitatively. Tab. 3.2 summarizes the results for the case that the specific parameter is augmented. A positive sign means an increase in the amplitude or the shift to higher frequencies for the minima and maxima, respectively. One single sign or '±' represents negligible deviations, for the latter no trend can be recognized.

			Amplitude		Frequency shift	
Parameter	Standard value		S_0	A_0	S_0	A_0
E_{11}	8.5	[GPa]	+	−	+	+
E_{33}	21	[GPa]	+++	+++	++	+++
G_{13}	3.1	[GPa]	±	+	−	−
ν_{12}	0.35	[-]	±	+	±	+
ν_{13}	0.32	[-]	+	+	+	++
d_{31}	-171	[pm/V]	−	−	−	−
d_{33}	374	[pm/V]	+++	+++	++	++
d_{15}	470	[pm/V]	−	+	−	−
ε_{11}	833	[-]	±	−	±	+
ε_{33}	755	[-]	±	−	−	−−
d_{AFC}	0.3	[mm]	+++	+++	−−−	++
ρ_{AFC}	4700	[kg/m^3]	−−	−−	−−−	−−−

Table 3.2: Qualitative sensitivity of the amplitude of a maximum and the frequency of a minimum in the transfer function due to an augmentation of 10% of single parameters of the 2D model. A positive sign indicates an increase in the amplitudes or a shift to higher frequencies, respectively. The more signs the higher the influence of the respective parameter.

There are two material parameters of the AFC which have a major influence on the results, the elastic modulus E_{33} and the piezoelectric constant d_{33}, both in the fiber direction. This seems reasonable because the length is much larger than the thickness of the AFC. Since the values of these two parameters, in particular d_{33}, are not known exactly, one has to keep in mind the findings presented here when comparing the results from simulations with the experimental measurements.

The simulation is also sensitive to changes of the thickness and density of the AFC. However, these parameters can be determined with considerable accuracy.

3.4 Experimental Investigation

3.4.1 Materials

The aluminum plate (alloy: 5005-H14) was quadratic with a length of 1,500 mm. It was chosen as large as possible in order to maximize the time until reflected waves from the boundaries arrive at the measurement points. The thickness was 1 mm. Since aluminum plates with dimensions like these are produced with a rolling process, the isotropy in the plane was experimentally controlled with a standard tensile test. It turned out that the plate is isotropic with an elastic modulus of 68.9 GPa and a Poisson's ratio of 0.33. For the measurements, the aluminum plate was mounted vertically with cords fixed at the two upper corners to achieve free boundary conditions.

Two similar AFC elements with standard design (indicated as AFC-1 and AFC-2, see Tab. B.1) and one AFC with a reduced length (AFC-3) were investigated. The active length of the shortened AFC was set to 20 mm in order to excite one single mode at a specific frequency (see Sec. 3.5.1 for details). Similar to the standard AFC with a total and an active length of 34 mm and 31 mm, respectively, the difference of the total and the active length for the shortened AFC was set to 3 mm, which yields a total length of 23 mm. A standard AFC was shortened on one side with a circular saw with a diamond blade. To achieve an active length of 20 mm, one finger of the IDE on the shortened side was electrically isolated by drilling a small hole through it. The total and active width of all AFCs was 40 mm and 20 mm, respectively.

Each AFC was glued on the front side of a separate aluminum plate with similar dimensions. The AFC was permanently bonded in the center of the plate with the fibers oriented parallel to one side of the plate with a commercial two component adhesive (Araldite® standard or Araldite® rapid from Vantico AG, Switzerland). To obtain a constant and thin bonding layer, the AFC was pressed on the plate during curing with a constant weight (around 1 kg). For the electrical contact, a BNC-connector is soldered to the two short copper wires, which contact the electrodes of the AFC. Further, the ground was also connected with the aluminum plate.

For generating waves in the plate for the investigation of the AFC as receiver, circular piezoceramic transducers (type PZ26 from Ferroperm-Piezoceramics, Denmark) with a polarization through the thickness were used. The dimensions were 5 mm or 10 mm in diameter and 1 mm in thickness. According to manufacturer's specifications their first resonance frequency in the plane was expected at 220 kHz and 440 kHz for a diameter of 10 mm and 5 mm, respectively, and through the thickness at 2 MHz for both for free boundary conditions. Electrical impedance measurements showed that the planar resonance of the 10 mm disc bonded to the plate occurred at 260 kHz which seems reasonable since the bonding leads to a stiff-

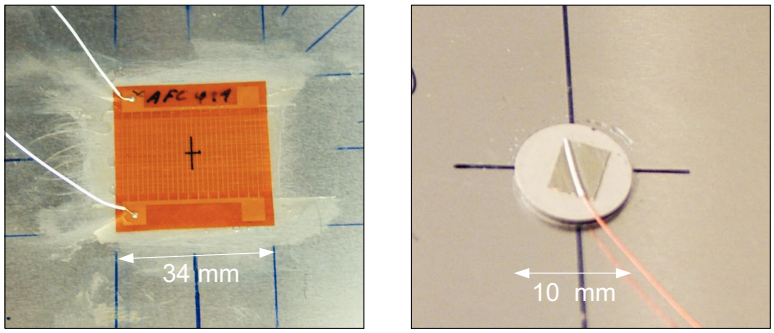

Figure 3.12: Close-up view of the AFC (left) and the piezoceramic disc transducer (right) bonded to the aluminum plate.

ening. The resonances should virtually not influence the measurement of the transfer function of the AFC, since the transfer function was normalized with the amplitudes of the incident wave, which were independently measured with the laser interferometer. However, when exciting the piezoceramic transducer at the frequency of the planar resonance, it vibrated for a longer duration. Thus, the excited S_0 and A_0 wave packets were elongated and not separated anymore, which prevented the proper measurement of the transfer function. This was the case in particular for the 10 mm piezoceramic disc when evaluating the transfer function of the A_0 mode. Therefore, the smaller disc was applied which allowed for estimating the transfer function up to 450 kHz. However, it was used only for measuring the A_0 transfer function while the larger disc was used for the measurement of the S_0 transfer function due to higher amplitudes of the excited waves. The ceramic discs were bonded with a commercial two component adhesive (Araldite® rapid) to the backside of the plate, where they constituted no obstacle for the laser measurements on the front side. The electrical contact was achieved by bonding a copper wire (0.2 mm in diameter) on the top electrode with a conducting adhesive aluminum tape. The wire was then connected over co-axial cable with the amplifier. The bottom electrode constituted the ground and was connected over the aluminum plate and a copper wire with the shield of the co-axial cable. No conducting additives were added to the adhesive to ensure the electrical contact between the bottom electrode and the plate, because it turned out that a thin bonding layer and the existing roughness of the surfaces were sufficient.

3.4.2 Setup and Measurement

The experimental setup for both investigations, AFC as emitter and as receiver, is shown in Fig. 3.13. It consisted of the plate with the piezoelectric elements, the laser interferometer and electronic devices. Some components were computer-controlled by using LabVIEW® (National Instruments) and the IEEE 488 Interface (General Purpose Interface Bus, GPIB).

- The signal for excitation was generated in the computer with LabVIEW® as a vector of discrete values with sufficiently high resolution in time. The

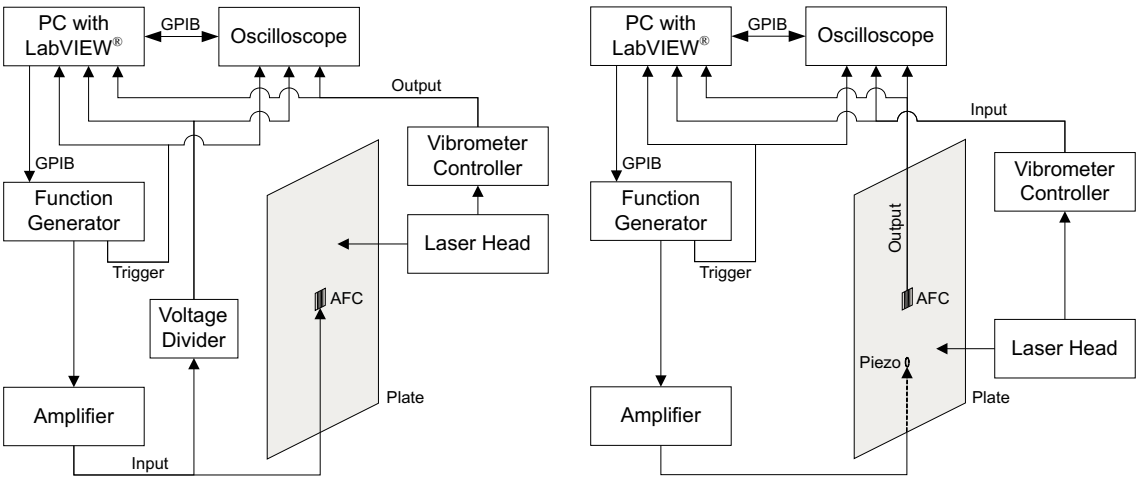

Figure 3.13: Schematics of the experimental setup for the investigation of the AFC as emitter (left) and reciever (right).

vector was then loaded via GPIB to the function generator (type 33120A from Agilent). The function generator converted the vector into an analogue voltage signal with an amplitude of ±2 V maximum and a trigger frequency of 5 Hz. The trigger signal was used for synchronizing excitation and measurement.

- The voltage signal was amplified by a factor of 100:1 by a voltage amplifier (type 7500 from Krohn-Hite) before being applied to the AFC or piezoceramic transducers.

- To record the excitation, the amplified signal was also sent through a voltage divider (see text below).

- For non-contact measurement of the surface velocities, a heterodyne laser interferometer (type OVF 505 from Polytec) and a Bauernfeind prism (see text below) were used. A laser measurement with an incident angle smaller than 90° required the use of retro-reflecting foil, which was positioned at the measurement point. The thin foil was also used for measurements perpendicular to the plate although the reflectivity of the aluminum surface would be sufficient.

- The laser head was installed on a positioning system (from Aerotech), which allowed to move the measurement point all over the plate. The navigation was computer-controlled with LabVIEW®.

- The vibrometer controller (type OVF 5000 from Polytec) demodulated the signal of the laser head and generated a voltage signal, which was proportional to the measured surface velocity. The direction of the velocity coincided with the direction of the laser beam. The sensitivity of the interferometer was set to 25 mm (s V)$^{-1}$ and allowed for recording frequencies up to 1.5 MHz.

- For the digitization an analog-digital converter with two channels for simultaneous recording (type NI PCI-5922 from National Instruments, here called NI-card) was used. An anti-aliasing filter was already implemented within the NI-card. For the case of the AFC as emitter, the excitation signal and the signal from the laser measurement were recorded, for the case of receiver, the two channels were used for the laser signal and the signal from the AFC. The vertical range of the NI-card was maximal ±5 V with a resolution of 18 bits, the sampling frequency was set to 10 MHz and the record length to 5'000 or 10'000 samples (data points). Each measurement was repeated 100 times ($n = 100$) and the data from both channels were stored for each repeated measurement separately. This was required for the analysis of the coherence. The NI-card was controlled with LabVIEW® and triggered by the function generator.

- All signals were additionally guided to an oscilloscope (type DL1640 from Yokogawa) for visualization. Due to failures of the NI-card, it was necessary to use the oscilloscope for the data acquisition of some measurements, whereby the sampling rate was set to 10 MHz and the record length to 5'000 records. The vertical resolution with 8 bits was worse than that of the NI-card but still sufficient. LabVIEW® and the GPIB enabled the communication over the computer, which simplified the control and data transfer. Since only the averaged signal could be stored by the oscilloscope, a coherence analysis could not be carried out for these measurements. The oscilloscope was triggered by the function generator.

As mentioned in Sec. 3.2 several measurements at the same point but with an excitation signal with changing frequency content had to be performed. For this, a routine was programmed in LabVIEW®. It allowed for defining the parameters for the needed excitation signals and for the data acquisition in advance and controls then the whole measurement process. The positioning system, however, was not implemented in the routine, i.e. the movement of the laser head from one measurement point to the next had to be separately controlled.

To improve the signal-to-noise ratio, the amplitudes of the excitation signal sent to the AFC or to the piezoceramic transducer were chosen as high as possible. However, since the transfer behavior of the amplifier and the voltage divider was not constant over the whole frequency range, the amplitudes of the different excitations had to be adjusted according to the limitation given by the NI-card.

The laser interferometer measured only the velocity component in the direction of the laser beam. Thus, three measurements from linearly independent directions but at the same point would be required to determine the complete velocity vector. These measurements could be performed consecutively since the single experiment was repeatable. For the estimation of the transfer function of the A_0 mode the OoP component v_x was needed. This component could be directly measured by guiding the laser beam perpendicularly to the plate (beam A in Fig. 3.14). The IP component in the r-direction, which was needed for the S_0 transfer function, was

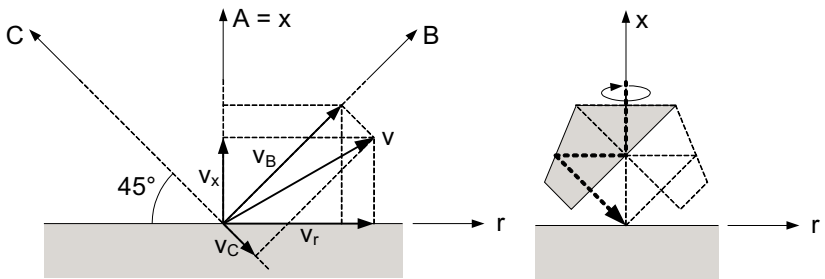

Figure 3.14: Relation between the velocity components measured with the laser interferometer (beam A without and B and C with Bauernfeind prism) and the components in r- and φ-direction (left) and the principle of a Bauernfeind prism (right).

determined from the two measurements along beam B and C. A Bauernfeind prism was used, which deflected the laser beam in such a manner that the incidence angle was 45°. The measurement point remained at the same position, even if the prism was rotated around the direction A. When the beam B and C were lying in the r-x-plane, the velocity components v_r and v_x can be expressed in terms of the measured components as

$$\begin{aligned} v_r &= \tfrac{\sqrt{2}}{2}(v_B - v_C) \\ v_x &= v_A = \tfrac{\sqrt{2}}{2}(v_B + v_C) \end{aligned} \tag{3.36}$$

Note that the measured component v_C as shown in the Fig. 3.14 has opposite sign than v_B. The reason for directly measuring the component v_x, although it can be determined from v_B and v_C, is the better signal-to-noise ratio since reflections of the laser beam within the Bauernfeind prism were avoided. Further, a mismatch between the directly measured and calculated signal indicated inaccurate measurements. The same procedure can be applied for determining the φ component, wherein the beams B and C have to lie in the φ-x-plane.

Since the aim of the experiments was the determination of the transfer function of the AFC one had to ensure that other components of the measurement system did not influence the result. For the AFC as emitter the physical quantities of interest were the excitation voltage signal (input) and the surface velocity (output). Between these quantities and the data acquisition, the voltage divider and the laser interferometer were inserted. According to the manufacturer's specification, the transfer function of the laser interferometer has a constant value of one over the entire frequency range of interest. The applied voltage divider, however, was not ideal for the frequency range of interest and showed a non-constant transfer behavior (see Fig. 3.15) which has to be taken into account for determining the transfer function of the AFC. The transfer function of the voltage divider was measured by sending harmonic sinusoidal voltage signals $x(t)$ with an amplitude of 4 V peak-to-peak and varying frequency (generated by the function generator mentioned above) through the voltage divider. Both signals, the input $x(t)$ and the output $x^*(t)$ were guided to an oscilloscope where the peak-to-peak amplitude was measured for

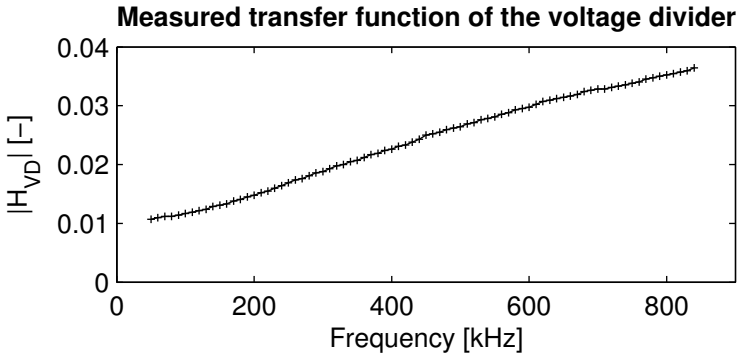

Figure 3.15: Measured transfer function of the voltage divider.

each frequency. The desired transfer function $H_{AFC}(f)$ of the AFC can then be calculated by multiplying the measured transfer function $H_m(f)$ with the transfer function $H_{VD}(f)$ of the voltage divider (see Fig. 3.16).

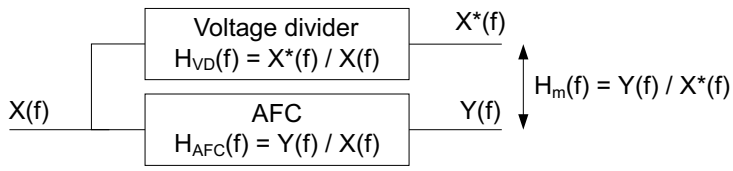

Figure 3.16: System for the experimental determination of the transfer function of the AFC as emitter. H_m is the measured transfer function, H_{AFC} the one to be determined.

Since the multiplication was performed element-wise, it was necessary that both functions had the same frequency resolution. To achieve this, the measured transfer function of the voltage divider was approximated with a polynomial of degree four. This allowed for calculating its value with sufficient precision at any frequency within the valid range.

For the AFC as receiver the surface velocity (input) and the voltage at the electrodes of the AFC (output) were of interest. The latter could be influenced by the impedance of the measurement circuit (cables and oscilloscope/NI-card). For a correct measurement, the condition $i\omega RC \gg 1$ must be fulfilled, where R and C are the resistance and the capacitance, respectively, of the measurement system. This is only approximately the case for the system used here (oscilloscope and NI-card in parallel and co-axial cable result in $R = 500$ kΩ and $C = 200$ pF) and the voltage as measured with the oscilloscope or NI-card deviates from the correct voltage at the electrodes of the AFC. However, the deviation of about 3% at 50 kHz and less than 1% above 200 kHz is small and, hence, negligible. Further, the lower limit of detectable frequencies given by the time constant $\tau = RC$ (here, C contains also the capacitance of about 700 pF of the AFC in parallel) is around 2 kHz and therefore much below the considered frequency range.

During the experiments, the voltage signal measured with the AFC as receiver was superposed by a harmonic sinusoidal voltage signal with a frequency of 50 Hz

caused by the power supply of the measurement instruments and induced over the electrical ground. This yielded a nearly constant offset of the recorded signal since its duration (0.5 ms) was much shorter than the period of the 50 Hz signal (20 ms). Although the offset had no influence on the transfer function in the considered frequency range, it was subtracted from the original data before further signal processing. Another possibility to cut out the frequencies of the disturbance would be inserting a high-pass filter between AFC and data acquisition.

3.4.3 Coherence Analysis

The coherence $\hat{\gamma}$ and the confidence interval $\hat{s}$ (see Eq. (3.10) and (3.11)) were estimated for all measurements as long as each repetition was stored separately. The results are presented here for one typical measurement for the determination of the transfer function of the A_0 mode (ExpE1, see Tab. B.1). The AFC was used as an emitter and the excitation signal, or input signal, respectively, corresponded to a linear frequency sweep with a Hanning window from 5 kHz to 200 kHz. The OoP component of the surface velocity (output signal) was measured at $(r, \varphi) = (400, 0°)$. The measurement was repeated one hundred times ($n = 100$) and the confidence interval $\hat{s}$ was calculated with a percentage point for the F distribution of $\alpha = 99\%$. Fig. 3.17 shows the amplitude spectrum of the transfer function with the confidence interval and the coherence function. The frequency range for which the coherence is higher than 0.95 extends from 20 kHz to 191 kHz. In this range, the confidence interval is very small, i.e. the measurements are well repeatable and also the noise is rather small. The peaks above 191 kHz are not significant since the coherence is poor.

When the single transfer functions, each reduced to the respective frequency range, were compounded to the overall one, the overlapping parts should theoretically lie in the confidence interval of each other. However, this is not always the case as shown in Fig. 3.18 on the left side. The reason is the application of the Tukey window to the output time signal for extracting the wave packet of interest and the fact that the different wave modes are not always completely separated for each excitation signal: If the duration of the window is chosen too long, there are contributions of other wave modes within the signal, and if it is chosen shorter, it will affect the wave of interest, in particular at the beginning and the end of the window where the amplitudes are depressed. In both cases, the transfer function will show small deviations from the optimal result.

One can generally say that the coherence was sufficient within the respective frequency range for all performed measurements for the AFC as emitter as well as for the AFC as receiver. However, some measurements for the S_0 transfer function of the receiver showed a coherence of only 0.8. Significant variations in the signal-to-noise ratio of the laser measurements are supposed to be responsible for it. Nevertheless, the overall transfer function corresponded to a reasonable graph. Due to the good results, the coherence function and the confidence interval are not presented anymore in the figures of the following section. Further examples for the AFC as emitter and

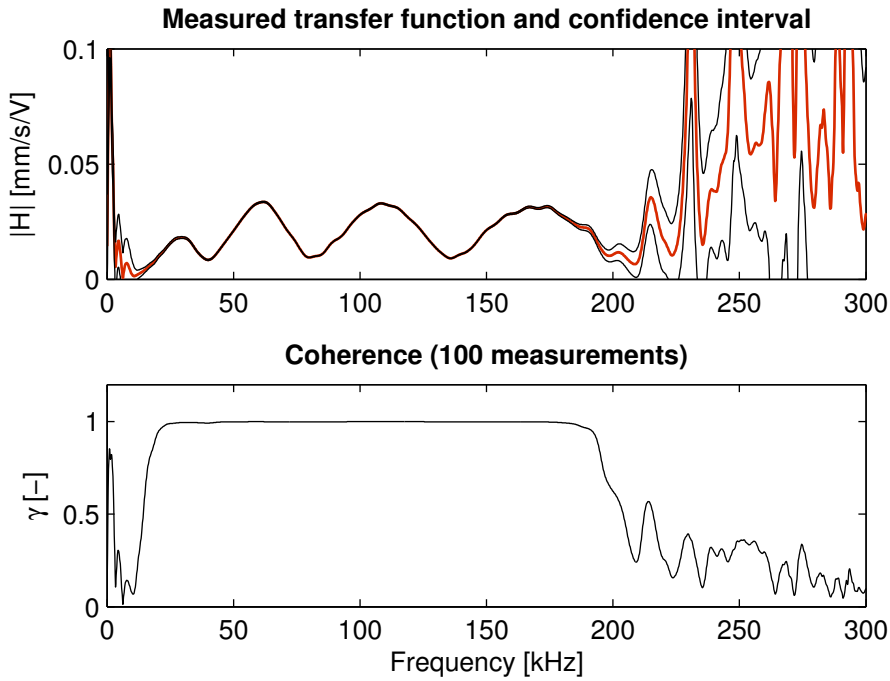

Figure 3.17: Example of the measured transfer function of the AFC as emitter (top, red) with the estimated confidence interval $\hat{s}$ for $\alpha = 99\%$ (top, black) and the estimated coherence function $\hat{\gamma}$ (bottom) for hundred repeated measurements. The excitation signal was a linear frequency sweep from 5 kHz to 200 kHz (see Tab. B.3) and the OoP surface velocity was measured at $(r, \varphi) = (400, 0°)$. The relevant frequency range ($\hat{\gamma} > 0.95$) for the transfer function is from 20 kHz to 191 kHz.

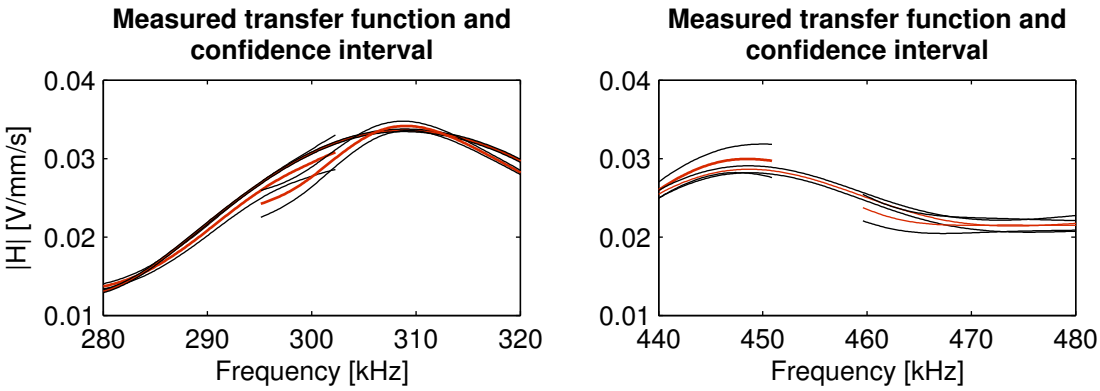

Figure 3.18: Examples of overlapping parts of the partial transfer functions (red) with the confidence interval (black).

receiver can be found in App. C.

3.5 Results and Discussion

The results are presented at the same time for both, the simulations and the experiments. Except of the scaling by the factor ξ or ξ^* which was needed due to the different electrode spacing within the simulation and the experiment (see Sec. 3.3.2 for details), the results of the simulation are represented as calculated. Hence, if not other stated, they can be quantitatively compared with the experimental data. Further, since the excitation for the simulation and the experiment started not at the same time, the experimentally measured signals were shifted in time in such a way that the excitation signal fitted that of the simulation (exceptions are stated). The time shift was not needed for the determination of the transfer functions. All data from the experimental investigation which are presented below correspond to the averaged data sets. For simplification, the amplitude spectra of the transfer function is just called transfer function.

For the experiments of the AFC as emitter two elements with standard design (AFC-1, AFC-2) and one with a reduced length (AFC-3) were investigated (see Tab. B.1). If not otherwise stated, the results for the standard AFC are generally from the experiments with AFC-1. However, for the experiments of the AFC as receiver only AFC-2 was investigated.

3.5.1 AFC as Emitter

Time Domain

Fig. 3.19 shows time histories of the radial IP and OoP component, v_r and v_x, of the simulated (2DE1-3DE1) and experimentally measured (ExpE1) surface velocities at $(r,\ \varphi) = (200,\ 0°)$. The AFC (standard design, $l_a = 31$ mm) was excited for both, the simulation and the experiment, with a frequency sweep from 5 kHz to 250 kHz (see Tab. B.3). The S_0 mode in the simulation was disturbed after 140 μs due to the reflected waves from the free boundaries of the plate. Also contributions of the IP components of the overlapping A_0 mode were present and interfere with the S_0 mode. On the other hand, the OoP component of the A_0 mode was not affected substantially by the S_0 modes since the OoP components of the S_0 modes are negligible within these frequency range. The effect of the dispersion can clearly be seen in the distorted wave form of the A_0 mode. The faster wave components which were excited at the end of the frequency sweep superpose the slower ones. Hence the wave packet is contracted in time which can be seen in its shorter duration compared to that of the excitation signal.

By looking at the radial IP component of the surface velocity, it can be seen that the amplitudes of the S_0 wave packet decreased 50 μs after the arrival time and reach a minimum after 85 μs although the duration of the excitation signal took 150 μs. The reason can be found in the transfer behavior of the AFC itself,

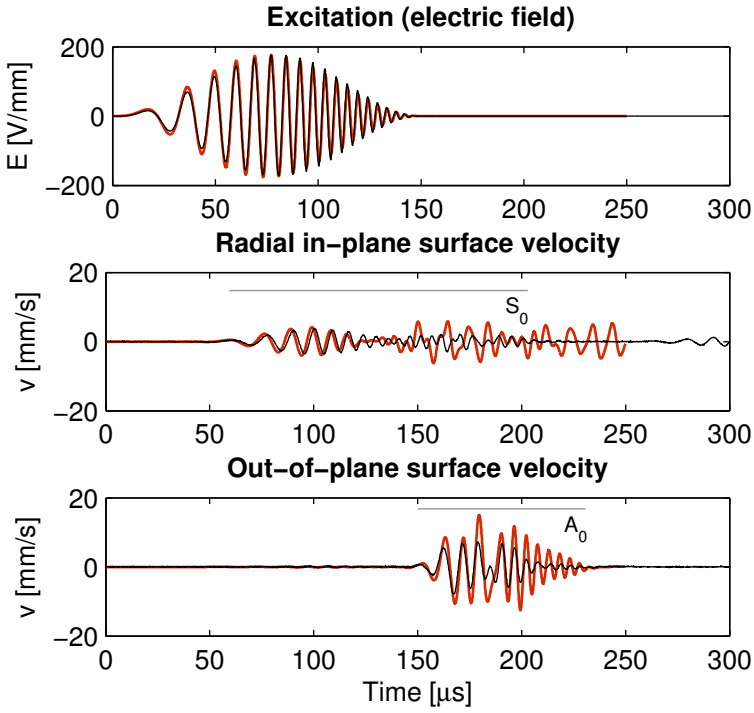

Figure 3.19: Simulated (red) and measured (black) time histories of the voltage signal used for the excitation of the AFC (linear sweep from 5 kHz to 250 kHz, top), the radial IP (middle), and the OoP (bottom) surface velocities at $(r, \varphi) = (200, 0°)$.

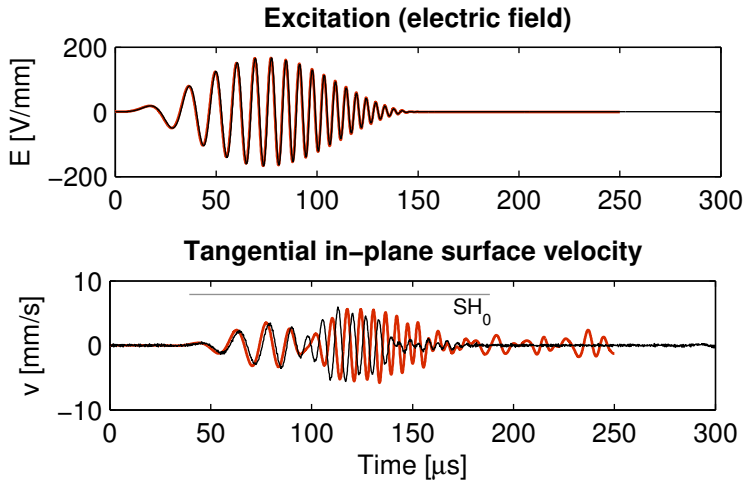

Figure 3.20: Simulated (red) and measured (black) time histories of the voltage signal used for the excitation of the AFC (linear sweep from 5 kHz to 250 kHz, top) and the tangential IP surface velocity (bottom) at $(r, \varphi) = (100, 30°)$.

i.e. at the corresponding frequency the energy is only poorly transmitted to the plate. Since the excitation signal changes its frequency linearly, the frequency of the minimum can be estimated by looking at the time scale. For the sweep as used here with a duration of 150 μs, 85 μs corresponds to a frequency of about 150 kHz. Consequently, a minimum in the transfer function is expected at this frequency, which will be shown later.

Good agreement was achieved between the simulated and experimentally measured data regarding the arrival times and the wave form. However, the amplitudes are higher in the simulations for both modes particularly due to the absence of any energy dissipation in the 2D and 3D model. Further, it is known from the sensitivity analysis that the elastic modulus E_{33} and the piezoelectric constant d_{33} have a major influence on the amplitudes. In particular, the d_{33} might be responsible for the differences since its value was assumed to be equal to that of PZT bulk material. A decrease of 10% will yield a reduction of the amplitudes by about 10%.

Beside the two Lamb wave modes a SH_0 mode was excited by the AFC as already shown in the example of the simulation (see Sec. 3.3.6). This mode could also be obtained in the experiments. The time histories of the tangential surface velocity component at $(r, \varphi) = (100, 30°)$ is given in Fig. 3.20. The simulated time history was disturbed after 100 μs due to reflected waves. Contrary to the S_0 mode, the decrease in the amplitudes started already 40 μs after arrival time. The wave form as well as the arrival time are in good agreement between simulation and experiment.

Fig. 3.21 shows the time history of the IP component of a S_0 mode at $(r, \varphi) = (200, 0°)$. The excitation was a tone burst with a Hanning window with 3.5 and 4 cycles for the 2D simulation (2DE1) and the experiment (ExpE1), respectively, at a center frequency of 400 kHz. As could already be seen in the example of the simulation in Sec. 3.3.6, two wave packets appeared, each excited at one of the edges

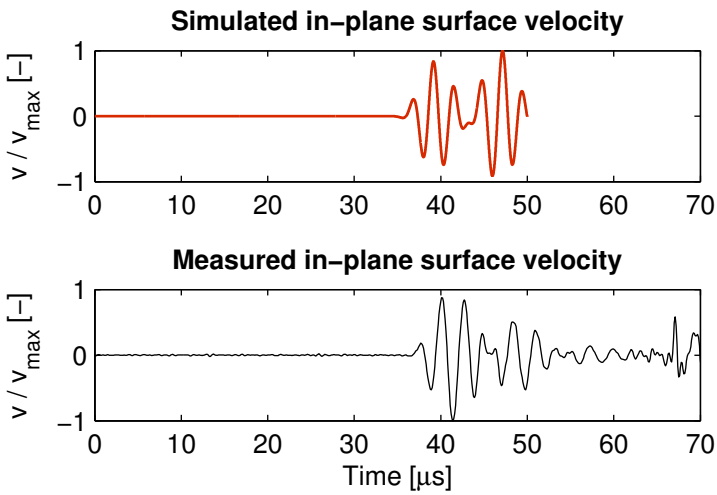

Figure 3.21: Simulated (top) and measured (bottom) time histories of the IP surface velocity at $(r,\ \varphi) = (200,\ 0°)$. The AFC was excited with a tone burst with a Hanning window with a center frequency of 400 kHz.

of the AFC where the interfacial stress distribution ends up with a peak. The time shift between the two packets of about 6.6 μs corresponded to the time needed for the S_0 mode to propagate over the length of the AFC. Since the time shift was equal for both, the simulation and the experiment, it can be concluded that the simulated stress distributions represent well the situation within the experiment. Thus, in a simplified consideration for the x-z-plane one can assume that the waves are excited at two point sources located at the surface of the plate (see Fig. 3.22), which corresponds to the model of Giurgiutiu [23]. The excited waves, here the S_0 mode, propagate in both the positive and the negative z-direction and the two waves from the two sources which propagate in the same direction interfere with each other. Here, the duration of the 400 kHz 4-cycle tone burst is too short, so the two packets are not superposed completely. This consideration explains also the existence of the minima and maxima in the transfer functions as already stated by Giurgiutiu [23]. Because the two point forces at either end of the AFC are in opposite z-direction, the two waves which propagate in the same direction are in opposite phase. Thus, if the given active length of the AFC is an even multiple of half the wavelength, the waves will interfere destructively leading to a minimum in the transfer function at the corresponding frequency. If it is an odd multiple, constructive interference will result in maximal amplitudes. This tuning effect is caused by the factor $\sin(k\frac{l_a}{2})$ in Eq. (3.1), where k corresponds to the wave number of the considered mode. Fig. 3.22 schematically shows the case for constructive interference when the wavelength is two thirds of the active length l_a of the AFC.

Similar measurements but with excitation amplitudes from 50 V to 200 V showed that the behavior of the AFC is approximatly linear in this voltage range. This confirms the use of linear constitutive equations in the model. 200 V are much below the electric potential used for the polarization process. But by increasing the

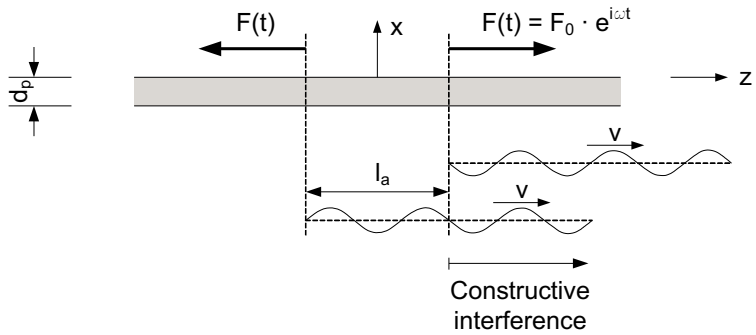

Figure 3.22: Simplified situation of wavelength λ versus active length l_a of the AFC in fiber direction for harmonic excitation according to the model of Giurgiutiu [23].

amplitudes even higher, non-linear effects become manifest. However, with regard to future applications in SHM, the amplitudes should be as small as possible to avoid the need for high voltage amplification, i.e. it is reasonable to neglect non-linear effects.

Frequency Domain

A quantitative comparison of simulated (2DE1-3DE1) and experimentally estimated (ExpE1) transfer functions are depicted in Fig. 3.23. The surface velocities were recorded at $(r, \varphi) = (200, 0°)$. As expected from the analytical model of Giurgiutiu [23] (factor $\sin(k\frac{l_a}{2})$ in Eq. (3.1)), the transfer functions show typical minima and maxima. The first peak of the S_0 transfer function (around 80 kHz) corresponds to a length of the propagating wave within the aluminum plate which is twice the length of the AFC. Theoretically, there are no other maxima expected at lower frequencies. The amplitudes tend to zero due to destructive interference of the two waves excited at either end of the AFC at frequencies where the length of the AFC is shorter than half a wavelength. The first minimum is around a frequency of 158 kHz for both, the simulation and experiment, which is close to the roughly predicted value from the consideration of the time signal. The first peak of the A_0 transfer function as shown in the figure theoretically corresponds to the second maximum, where the length of the AFC is one and a half times the wavelength. It has to be mentioned that the amplitude of this peak is not represented correctly due to the choice of the window function used for the transfer function calculations. It is expected from theory that the first maximum would occur at 2.5 kHz. The problem of determining the transfer function at frequencies below 20 kHz was the low group velocity of the A_0 mode that prevented separating the corresponding wave packet from all reflected wave packets.

The frequencies for the minima and maxima were well predicted by the simulation for the S_0 mode within the shown frequency range. Relatively large deviations can be seen for the analytical solution described by the factor $\sin(k\frac{l_a}{2})$ in Eq. (3.1). This can be attributed to the electro-mechanical coupling and the transducer-structure interaction which both are neglected in the analytical model. For the A_0 mode, the

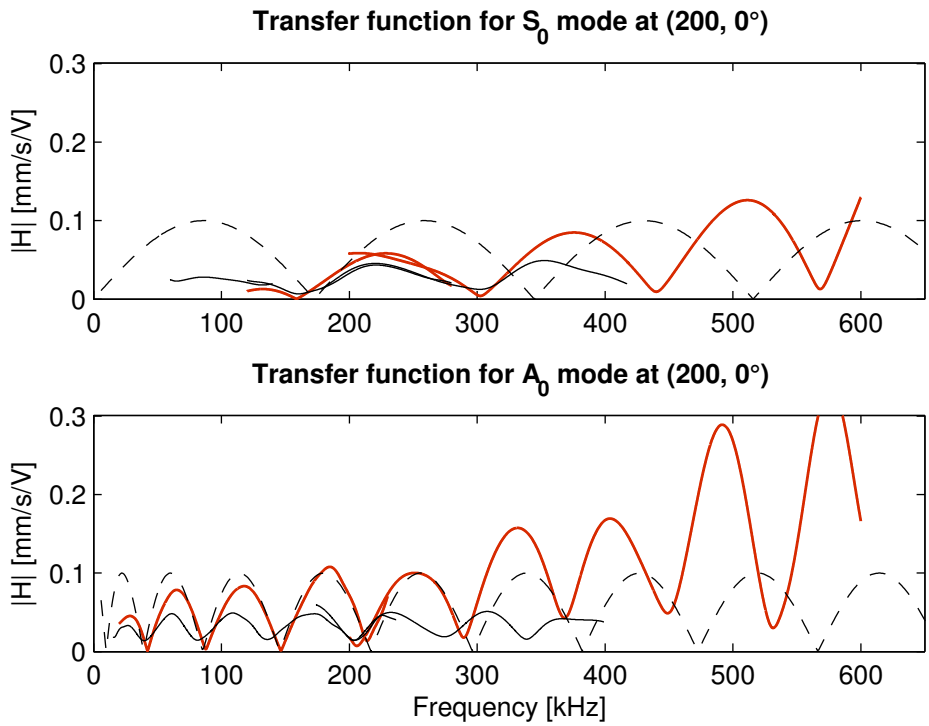

Figure 3.23: Simulated (red) and measured (black) transfer functions of the AFC as emitter for the S_0 mode (top) and A_0 mode (bottom). The surface velocities were recorded at $(r, \varphi) = (200, 0°)$. Factor $\sin(k\frac{l_a}{2})$ (dashed, arbitrary units) according to the model of Giurgiutiu [23].

analytical solution is almost similar to the simulated results up to 200 kHz. It seems that there is a systematic deviation between the simulated and the experimentally estimated transfer function. A possible reason for this could be the chosen length l_a of the AFC in the simulation since this parameter is directly coupled to the frequencies of minima and maxima over the respective wavelength. With increasing length of the AFC, the transfer function is contracted and the minima and maxima are shifted to lower frequencies. As expected from theory and as obtained in simulations with varying active length, this contraction is more pronounced for the A_0 mode than for the S_0 mode. Consequently, an enlargement of the length l_a in the simulation would lead to a better agreement with the experiments. This would mean that the effective active length of the AFC in the experiment is somewhere between the theoretical active length l_a and the total length l_{tot} of the fibers. This is contrary to the shear lag effect as obtained by Raghavan and Cesnik [64] for the MFC. Within their investigation, the active and total lengths were equal which was not the case for the AFC used for this work. The findings shown here have to be taken into account when dimensioning the length of an AFC with a required transfer behavior.

As already shown in the time signals, the amplitudes were higher for the simulation. This is attributed to the chosen material parameters for the AFC (in particular

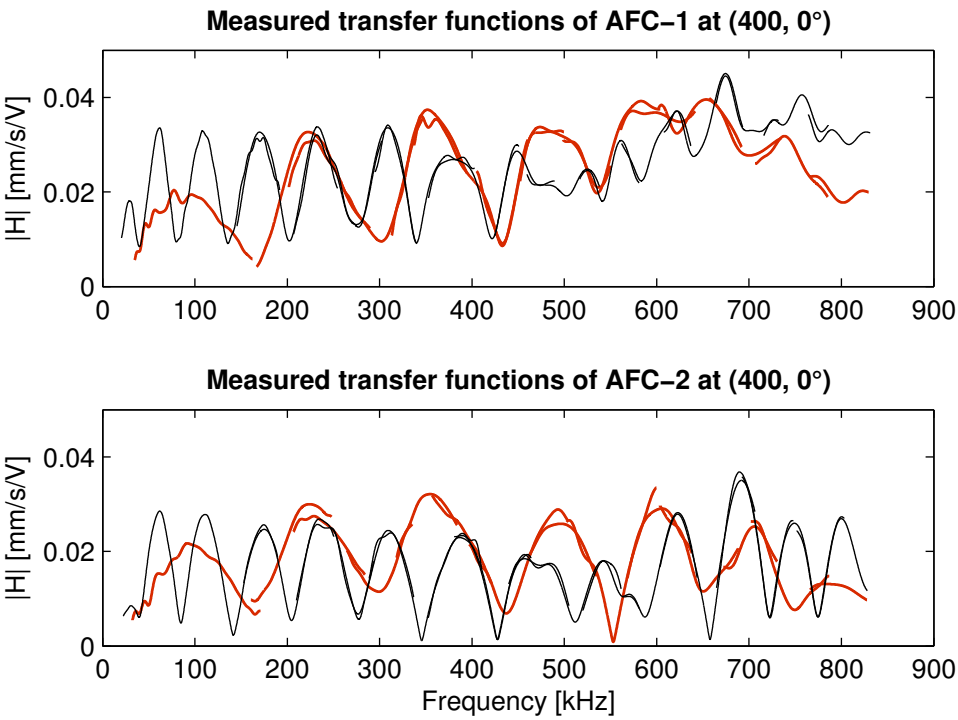

Figure 3.24: Measured transfer function of two AFC as emitter with standard design for the S_0 mode (red) and the A_0 mode (black). The surface velocities were measured at $(r, \varphi) = (400, 0°)$.

the elastic modulus E_{33} and the piezoelectric constant d_{33}) and the absence of any energy dissipation within the model. Further, the amplitudes of the maxima in the transfer function increase with increasing frequency for the simulation, while for the experimental results, the amplitudes of the maxima remain almost constant. First, it has to be pointed out that for a harmonic wave with constant displacement amplitudes, the velocity amplitudes would increase with increasing frequency. Second, the energy of the excited wave is more focused on the fiber direction at higher frequencies as it will be explained later on in this section. This yields higher amplitudes at higher frequencies for the transfer function in fiber direction. A possible reason why the maximum amplitudes for the experiment do not increase might be the material damping since its influence increases with increasing frequency, in particular within the epoxy matrix of the AFC and of the bonding layer, which show slightly visco-elastic material behavior.

Fig. 3.24 shows experimentally estimated (ExpE1) transfer functions for two similar AFCs with standard design over a frequency range up to 800 kHz. While the amplitudes are similar for both AFCs for the S_0 mode, the amplitudes for the A_0 mode are smaller for the second AFC (lower diagram). The difference of about 0.006 mm (s V)$^{-1}$ is almost constant between 80 kHz and 300 kHz. Good agreement is also achieved regarding the frequencies of the minima and maxima up to 450 kHz for both the S_0 and the A_0 transfer function. Above this frequency the regularity

seems to be disturbed, in particular for the first AFC (upper diagram). Small variations in the AFCs due to the manufacturing process (hand made) and in the bonding layer might be the reasons for it. For the second AFC it seems like the A_0 transfer behavior is the result of the superposition of two transfer functions each determined with a slightly different transducer length. This is probably due to the fact that the total and active length of the fibers are not identical. Since a change in the length yields a frequency shift of the minima and maxima and since this shift is small at lower frequencies (see also Fig. 3.30), the peaks can be recognized as double peaks only above 450 kHz. However, this behavior was not obtained within the experiments with the first AFC. Even if the database from the investigation of only two AFCs is small, it can be concluded that above 450 kHz the transfer behavior gets more and more unpredictable with the model presented here.

The quasi-periodic variation within the first peak of the transfer function for the S_0 mode is an artifact of the measurement procedure. On the one hand, it occurs due to the applied window function and it can be minimized by the use of well-chosen parameters for the time window. On the other hand, some small contributions from reflected waves excited in the previous measurement might be present in the measured IP signal of the surface velocity. Since the trigger rate (5 Hz) for repeating the measurements was chosen too high, these waves were not completely damped out before the following measurement had been started. This explains, why the disturbance is obtained only at lower frequencies where the damping is smaller than at higher frequencies. It is mentioned that the contributions of the previous measurement were hardly observable in the time signal due to the poor signal-to-noise ratio when measuring with the Bauernfeind prism. Nevertheless, the trend of the overall transfer function is well represented.

The simulated (2DE1-3DE1) and experimentally estimated (ExpE1) transfer functions for several points around the AFC are shown in Fig. 3.25 and 3.26 for the S_0 and A_0 mode, respectively. For the S_0 mode the surface velocities were recorded at $r = 100$ mm and 400 mm for the simulation and experiment, respectively, while for the A_0 mode the distance was $r = 200$ mm for both. The reason for the different distances are the reduced geometric dimensions within the simulations where reflections at the free boundaries make it difficult to obtain useful data for the S_0 mode at a distance of 200 mm and for varying angles. Therefore, the results can be compared only qualitatively. The angle φ varies from 0° to 60° in steps of 15° for the S_0 mode and from 0° to 30° in steps of 5° for the A_0 mode. Due to the decreasing amplitudes of the wave modes with increasing angle φ from the fiber direction and thus the decreasing signal-to-noise ratio, the transfer functions could not be estimated over the entire frequency range within the experiments. In particular, this holds for the S_0 mode due to the use of the Bauernfeind prism for determining the IP surface velocity. It has to be mentioned again that the peak of the A_0 transfer function at 28 kHz is not correctly represented due to the choice of the time window function.

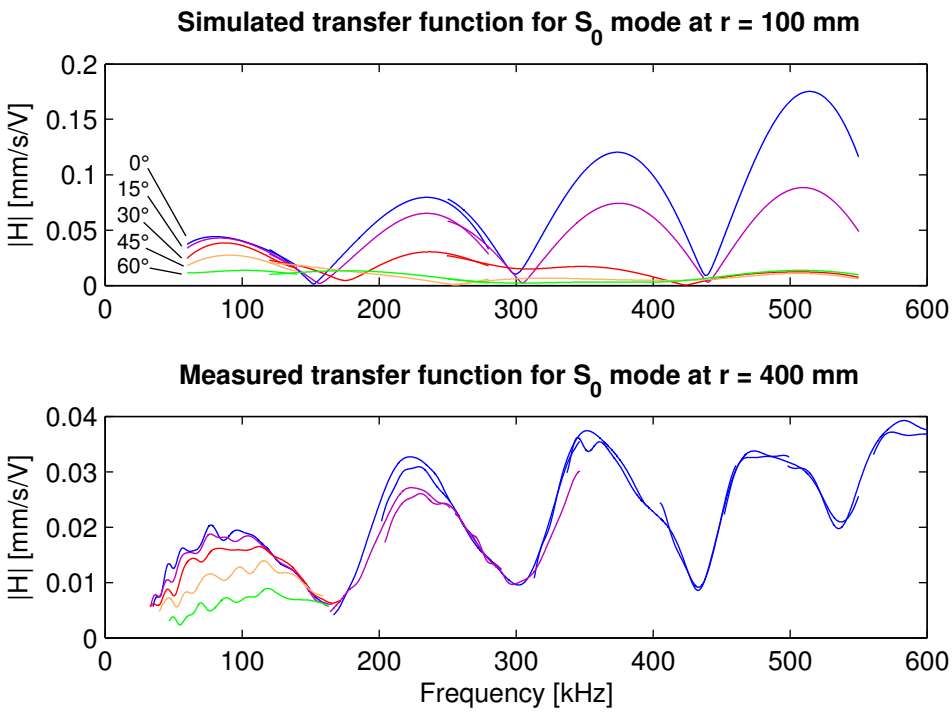

Figure 3.25: Simulated (top) and measured (bottom) transfer functions of the AFC as emitter for the S_0 mode. The surface velocities were recorded at $(r, \varphi) = (100, 0°\text{-}60°)$ for the simulation and at $(r, \varphi) = (400, 0°\text{-}60°)$ for the experiment. The measured transfer functions at $\varphi \geq 30°$ were estimated up to only 170 kHz.

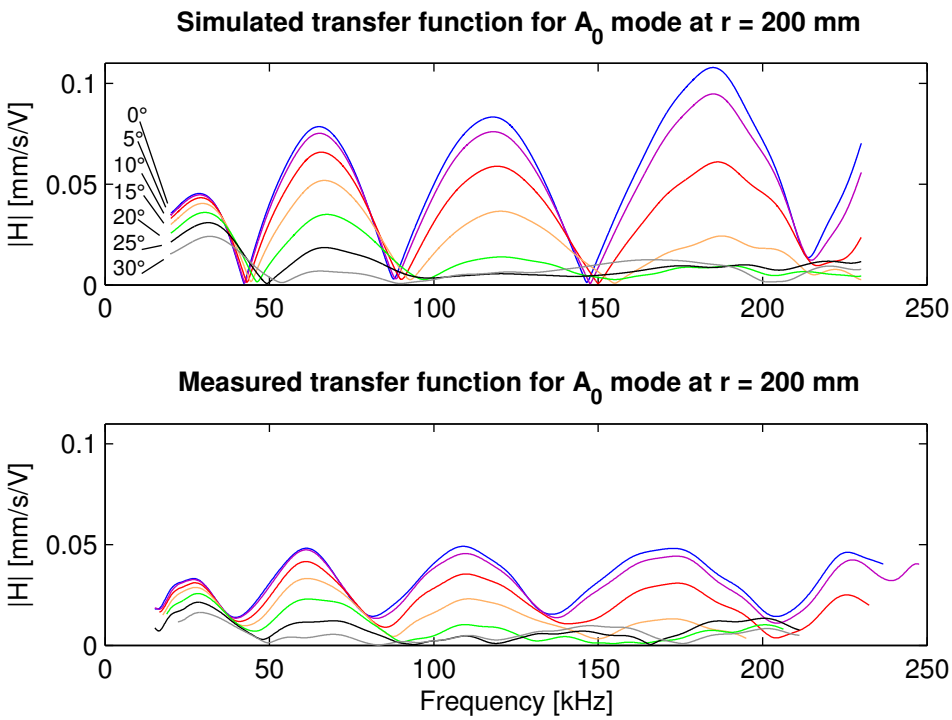

Figure 3.26: Simulated (top) and measured (bottom) transfer functions of the AFC as emitter for the A_0 mode. The surface velocities were recorded at (r, φ) = (200, 0°-30°) for both, the simulation and the experiment.

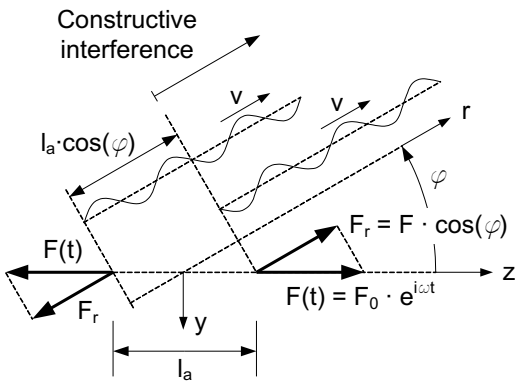

Figure 3.27: Simplified situation of wavelength λ versus active length l_a of the AFC in arbitrary direction for harmonic excitation.

The A_0 mode is more focused on the fiber direction of the AFC at a given frequency than the S_0 mode as could already be seen in the example of the simulation (see Sec.3.3.6). This is also depicted in the transfer functions, e.g., when looking at a frequency around 120 kHz. At an angle of $\varphi = 15°$, the amplitude for the S_0 mode is almost the same as for $\varphi = 0°$. But for the A_0 mode, the amplitude reduces to 43% for both the simulation and the experiment. Considering the trends with increasing frequency, it can clearly be seen that the waves are more and more focused on the fiber direction for both wave modes. The focusing effect is related to the ratio of the wavelength to the width of the AFC as it will be explained below. Further, due to the focusing effect, it is obvious that the amplitudes in fiber direction must increase within the simulation where any energy dissipation is neglected.

With increasing angle φ the first peaks seem to be shifted to higher frequencies. This effect can be explained again by considering two IP point forces acting in z-direction but with opposite sign (see Fig. 3.27). The distance between the two point sources corresponds to the active length l_a of the AFC. By looking at the y-z-plane and harmonic waves which travel in the positive r-direction at an angle φ from the z-direction, the following effects can be obtained for the far field ($r \to \infty$). The distance between the two sources in r-direction is $l^* = l_a \cdot \cos(\varphi)$, i.e. the required wavelengths for constructive or destructive interference decreases with increasing angle φ and therefore the minima and the maxima are shifted to higher frequencies. Further, it is expected that in a certain direction for a given frequency the two waves will interfere destructively. One example can be found in the simulated transfer functions for the A_0 mode at a frequency of 46 kHz where at $\varphi = 20°$ a minimum occurs, while for larger angles, the amplitudes increase again. It is obvious that the smaller the wavelength, the smaller the angle between the z-direction and the direction r of the first minimum. These effects are decribed by the term $\sin(k\frac{l_a}{2}\cos\varphi)$ in the analytical solution (see Eq. (3.2)) derived by Raghavan and Cesnik [64]. Further, for exciting Lamb waves in r-direction, only the r component of the point force can be taken into account. Consequently, the amplitudes decrease with increasing angle φ. This effect can clearly be obtained in the simulation as

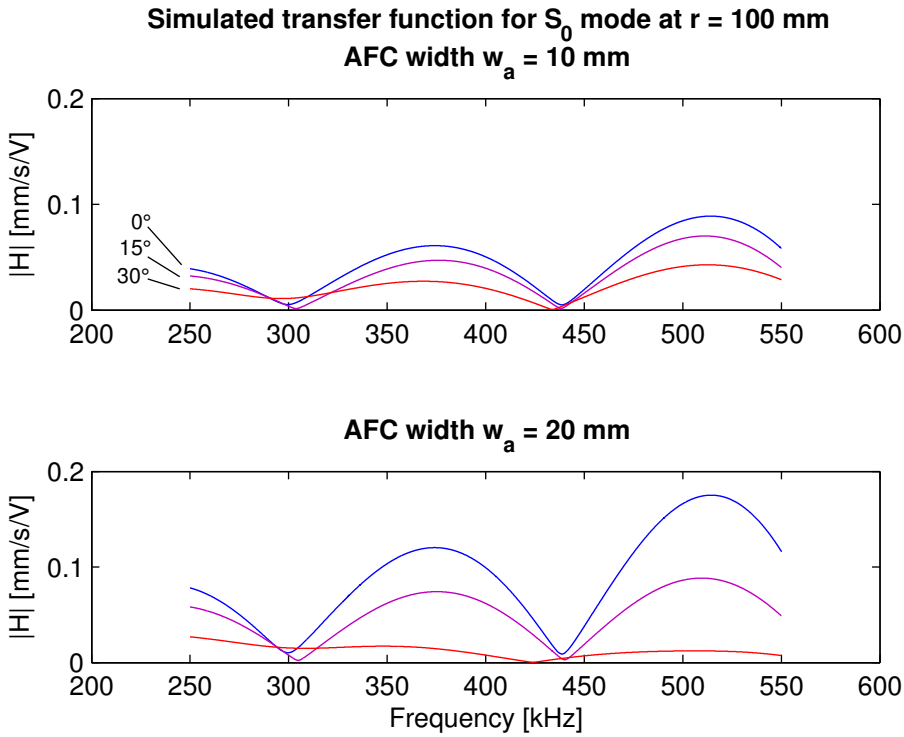

Figure 3.28: Simulated S_0 transfer functions of two AFCs used as emitter with an active width of 10 mm (top, 2DE1-3DE3) and 20 mm (bottom, 2DE1-3DE1). The surface velocities were recorded at $(r, \varphi) = (100, 0°\text{-}30°)$.

well as in the experiment. However, this consideration does not explain why the decrease of the amplitudes is more pronounced for higher frequencies. Therefore, it is essential to take also the width of the AFC into account.

To investigate the influence of the active width w_a on the resulting wave field, 3D simulations with $w_a = 20$ mm and 10 mm (2DE1-3DE1 and 2DE1-3DE3, respectively) were performed, while all other parameters remained constant. The resulting transfer functions for the S_0 mode at a distance of $r = 100$ mm are presented in Fig. 3.28 for the frequency range from 250 kHz to 550 kHz. The smaller the width, the smaller the amplitudes in general, which seems reasonable since a smaller area was excited. The frequencies for the minima and maxima remain constant. When looking at a given frequency but changing angles φ, it can be seen that the waves are more concentrated in the fiber direction for larger widths. Since the same effect could be obtained for increasing frequency, it can be concluded that the smaller the wavelength compared to the width of the AFC, the more pronounced is the focusing of the wave field in fiber direction. This is also the reason why at a given frequency the S_0 mode with its larger wavelength is spread over a larger angle than the A_0 mode.

This behavior can be illustrated again with a simplified consideration as depicted in Fig. 3.29. Forces along the active width w_a of the AFC are assumed. They act on the surface of the plate (y-z-plane) in fiber direction of the AFC and represent the

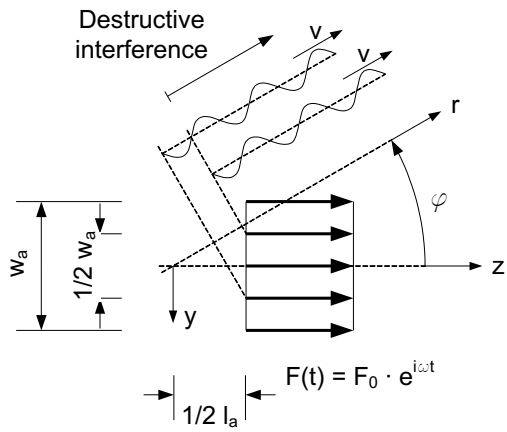

Figure 3.29: Simplified consideration of wavelength λ versus active width w_a of the AFC in arbitrary direction for harmonic excitation.

shear stresses generated along one of the AFC's edges during harmonic excitation. From a physical point of view the obtained wave field can be explained as the result from superpositions of an infinite number of single circular crested waves (Huygens principle), each starting at an infinitesimal point along the edge of the AFC. Since the waves start with similar phase, there will be certain directions where the resulting wave in the far field has minimal amplitude due to destructive interferences of all single waves. The factor describing this behavior is $\sin(k\frac{w_a}{2}\sin\varphi)/(k\sin\varphi)$ which is also included in the analytical solution of Raghavan and Cesnik [64]. The first minimum is given by $\sin\varphi = \frac{\lambda}{w_a}$, where λ is the wavelength. Thus, with increasing width or with decreasing wavelength – increasing frequency, respectively –, the respective angle decreases, i.e. the waves are more focused on the fiber direction. Qualitative comparisons of this behavior obtained from the simplified consideration with the results from simulations and experiments show good agreement. A more complete but still simplified excitation representing the forces transferred from a surface bonded AFC would be two line forces with opposite sign along both edges of the AFC within a distance equal to the active length l_a and corresponds to the approach of Raghavan and Cesnik [64]. However, they have not taken into account the influence of the surface bonded AFC.

Investigation of a Shortened AFC

To confirm the model with additional measurements with a transducer of different length, an AFC with standard design was shortened as described in Sec. 3.4.1. The length should be chosen between 10 mm and 31 mm in such a way that at one specific frequency an A_0 mode is excited preferably. For a first estimation of the required length, the theoretical model of Giurgiutiu [23] was considered. Fig. 3.30 shows the frequencies for the minima and maxima of the transfer functions for the S_0 and A_0 mode in function of the transducer length. The only solution below 450 kHz is at the length of 18.2 mm, where at 290 kHz a curve for a minimum of the S_0 mode

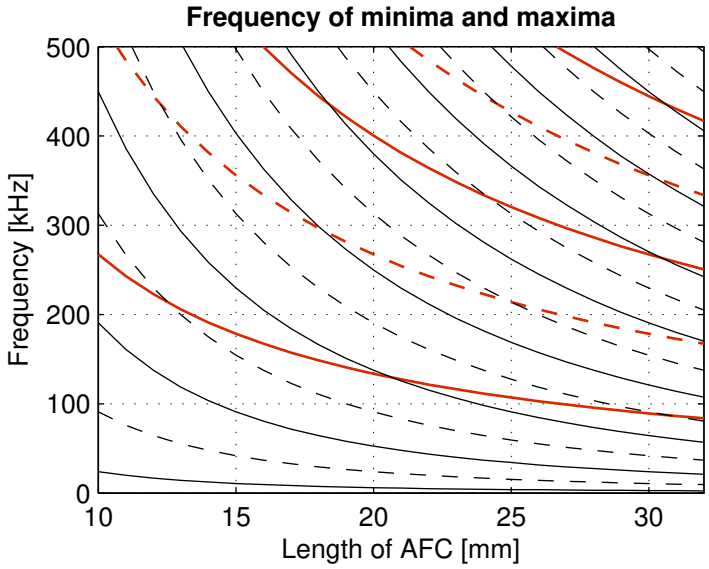

Figure 3.30: Frequencies of minima (dashed) and maxima (solid) in the transfer function of a surface bonded emitter for the S_0 (red) and A_0 mode (black) in function of the transducer length according to the model of Giurgiutiu [23] which neglects the influence of the emitter. The aluminum plate has a thickness of 1 mm.

crosses that one of a maximum of the A_0 mode. However, by comparing theoretical results for the standard AFC with the findings of the simulations and experiments presented above, one can estimate that an active length of 20 mm is better suited. The reason for this deviation is the presence of the AFC, which is neglected in the analytical model.

The AFC for the experiments (ExpE2) was shortened so that the total and the active length were $l_{tot} = 23$ mm and $l_a = 20$ mm, respectively, analogous to the standard AFC. Consequently, the effective active length in the experiment is expected to be slightly longer than 20 mm and hence the active length for the 2D and 3D simulations (2DE2-3DE2) is set to 21 mm. As predicted by simulations, the optimal frequency for emitting mainly the A_0 mode will be around 235 kHz.

Fig. 3.31 and 3.32 depict the results for the simulations and the experiments. The positions where the surface velocities were recorded are similar to the investigation of the standard AFC. The quasi-periodic variations in the A_0 transfer functions above 100 kHz are due to non perfectly separated wave packets. In general, the same findings as for the standard AFC can be stated for the shortened AFC. As expected from theory the frequencies for the minima and maxima in the transfer function are shifted to higher frequencies compared to the standard AFC. Further, a maximum for the A_0 mode coincides with a minimum for the S_0 mode at a frequency around 235 kHz as predicted by the simulation. Regarding the radiation around the AFC, it can be seen that the length of the AFC has no major influences on the focussing of the waves. Good correlation between the simulated and measured results could be achieved up to 470 kHz and 310 kHz for the S_0 and A_0 mode, respectively.

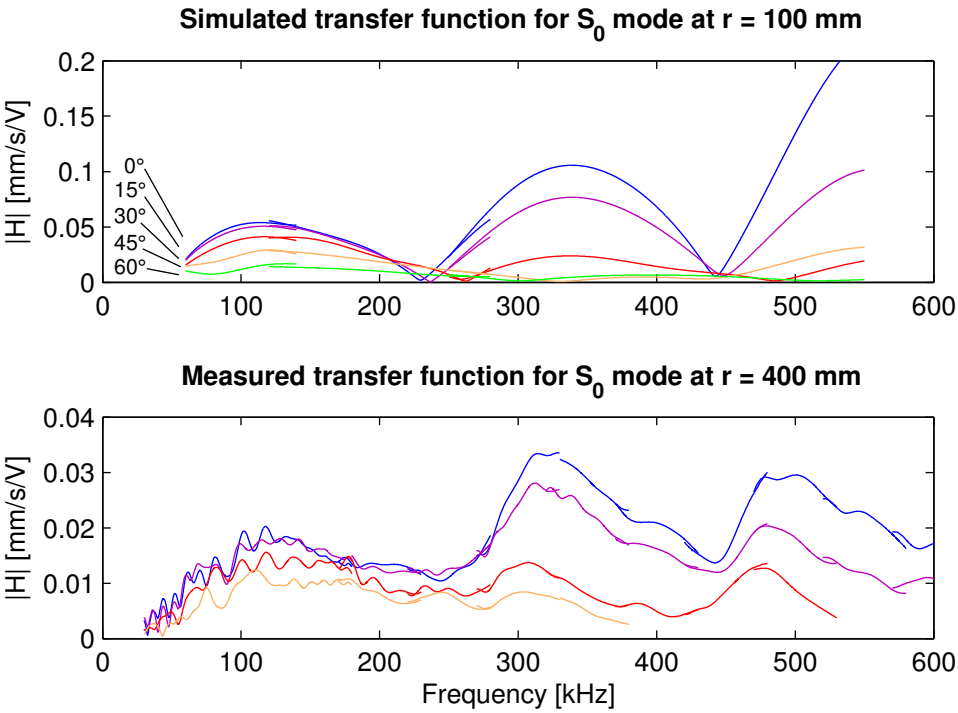

Figure 3.31: Simulated (top) and measured (bottom) transfer functions of the shortened AFC as emitter for the S_0 mode. The surface velocities were recorded at $(r, \varphi) = (100, 0°\text{-}60°)$ for the simulation and at $(r, \varphi) = (400, 0°\text{-}45°)$ for the experiment.

It can be concluded that beside the thickness and the material properties of the plate the length and the width of the AFC mainly define the characteristic of the wave field around the AFC. While the length is responsible for the occurrence of the minima and maxima in the transfer function in fiber direction due to interferences of waves excited at either end of the AFC, the width defines the radiation vs. the angle due to interferences of waves excited along one edge of the AFC. The reason for the strongly developed directionality of the wave field can further be attributed to the anisotropic behavior of the AFC, which leads to shear stresses concentrated mainly at two edges of the AFC and acting in the fiber direction of the AFC. The comparison of the simulated with the experimentally estimated results shows that the proposed simulation procedure is well suited for studying wave propagation phenomena caused by the excitation of surface bonded AFC.

3.5.2 AFC as Receiver

The AFC as receiver can be simulated only with the 2D model. Therefore, a comparison between the simulation and the experiment can only be given for the case when the incident wave propagates in fiber direction of the AFC. For other directions, only experimental results will be presented.

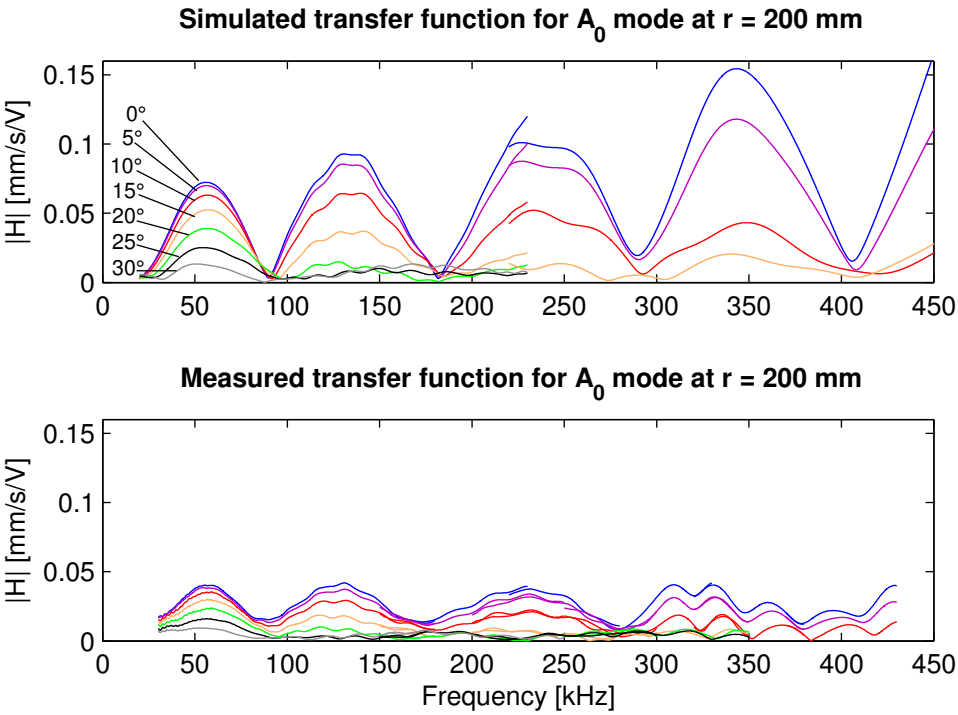

Figure 3.32: Simulated (top) and measured (bottom) transfer functions of the shortened AFC as emitter for the A_0 mode. The surface velocities were recorded at (r, φ) = (200, 0°-30°) for both, the simulation and the experiment.

Time Domain

Fig. 3.33 shows experimentally observed time histories of the voltage signal measured with the AFC and of the surface velocities measured with the laser interferometer for three different positions of excitation (ExpR1). The piezoceramic transducers used for excitation were located at a distance r = 200 mm from the AFC and in angles φ = 0°, 15° and 30° from the fiber direction of the AFC. The surface velocities were recorded in a distance of 200 mm from the excited emitter in a direction perpendicular to the straight line between the AFC and the respective emitter (see also Fig. 3.1). The excitation signal was a tone burst with a Hanning window with 5 cycles at a center frequency of 100 kHz and starting at t = 50 μs. The measurements were performed consecutively starting with the excitation by the emitter at φ = 0° which was then removed before exciting the next one. The piezoceramic transducers were able to excite both Lamb wave modes, the faster S_0 and the slower A_0 mode, as can clearly be seen in the laser measurements. The waves excited by each piezoceramic transducer had comparable amplitudes. It has to be mentioned that the IP component of the surface velocity of the A_0 mode is not necessarily reproduced correctly. The reasons for this are the relatively low phase velocity – and hence small wavelength – of the A_0 mode and small deviations of the positions of the two required laser measurements (even with the use of a Bauernfeind

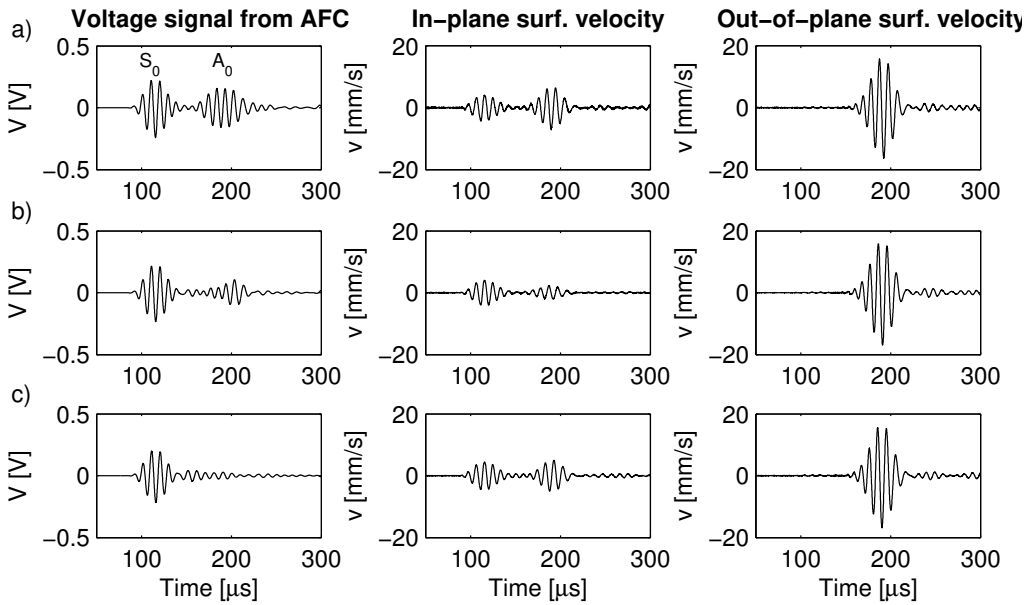

Figure 3.33: Measured voltage signal from the AFC as receiver (left diagrams) and IP (middle) and OoP (right) surface velocities at the corresponding point (see Fig. 3.1) measured with the laser interferometer. The excitation (5-cycle tone burst, Hanning window, center frequency of 100 kHz, starting at $t = 50$ μs) was achieved with piezoceramic transducers positioned at $(r, \varphi) = (200, 0°/15°/30°)$ (a-c).

prism), which leads to relatively large deviations for the calculated IP component. Theoretically, the IP surface velocity for the A_0 mode at 100 kHz is about three times smaller than the OoP component. Although the incoming waves at the AFC had similar amplitudes, the voltage signal of the AFC changed with changing incident angle. While the decrease for the S_0 mode was marginal for increasing angle, the amplitudes of the A_0 mode vanished almost for $\varphi = 30°$. This is similar to the findings for the AFC as emitter, where the S_0 mode is spread over a larger angle than the A_0 mode.

A comparison of simulated (2DR1) and experimentally measured (ExpR1) time histories for a S_0 mode is depicted in Fig. 3.34. The wave was excited at (r, φ) = (200, 0°), i.e. in fiber direction of the AFC, with a tone burst (5 cycles with a Hanning window) with a center frequency of 200 kHz and starting at $t = 50$ μs. Within the simulation, only the S_0 mode was excited, while in the experiment an A_0 mode would arrive after 130 μs. The simulated results were scaled so that the maximal amplitude of the IP surface velocity is equal to that one of the measurement. Further, the simulated data were time shifted so that the beginning of the simulated and measured S_0 mode coincides. It is noticeable that the frequency of the S_0 mode in the experiment seems to be slightly increased compared to the simulation. The reason for this is the piezoceramic transducer used for excitation. Due to the frequency content of the tone burst signal, the transducer was excited also in its planar resonance frequency at around 260 kHz. Thus, this frequency was

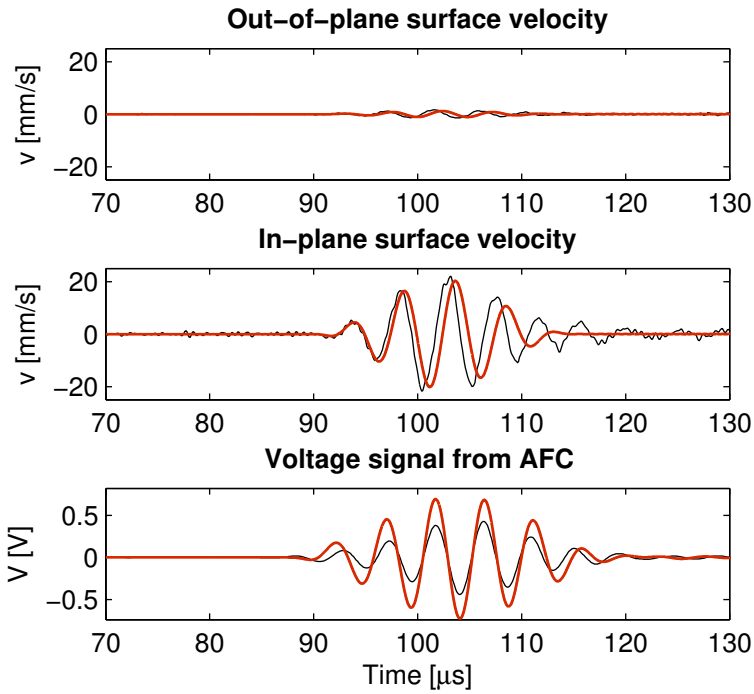

Figure 3.34: Simulated (red) and measured (black) IP (top) and OoP (middle) surface velocities and voltage signal from the AFC as receiver (bottom). The excitation (5-cycle tone burst, Hanning window, center frequency of 200 kHz, starting at $t = 50$ μs) was achieved with the piezoceramic transducer positioned at $(r, \varphi) = (200, 0°)$.

dominant in the excited wave pulse and, moreover, the pulse was elongated since the transducer was still vibrating for a few cycles after the electric excitation stopped. Good agreement was achieved regarding to the time and the form of the electric voltage signal. As for the AFC as emitter, the amplitudes within the simulation are overestimated. Again, the chosen material parameters for the AFC (in particular the elastic modulus E_{33} and the piezoelectric constant d_{33}) and the absence of the bonding layer and any energy dissipation in the simulations are responsible for this. Another source of error might be the piezoceramic transducers. Laser measurements around the excited transducers showed that the radiated wave fields were not exactly rotation-symmetric. Further, small phase shifts are attributed to differences between the distance from the piezoceramic transducer to the AFC and from the piezoceramic transducer to the point where the surface velocity was measured. The differences were estimated to be maximum 2 mm which corresponds to a difference in time of about 0.5 μs. Compared to the signal measured with the laser interferometer the noise level of the AFC signal is very low. Considering the simulated results, the wave pulse in the time history of the voltage signal is longer than the original incoming wave. The reasons are reflections and mode conversions at the edges of the AFC and the overlap of the two wave pulses measured when the incoming wave passes

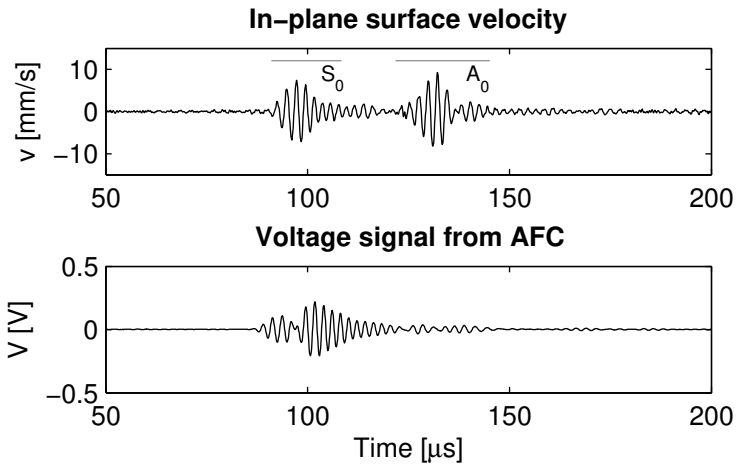

Figure 3.35: Measured IP surface velocity (top) and voltage signal from the AFC as receiver (bottom). The excitation (5-cycle tone burst, Hanning window, center frequency of 400 kHz, starting at $t = 50$ μs) was achieved with the piezoceramic transducer positioned at $(r, \varphi) = (200, 0°)$.

the AFC's edges (see text below). Since the incoming wave within the experiment has already more cycles, this effect can not be observed at this frequency.

Fig. 3.35 depicts the experimentally measured time history of the electric voltage while a S_0 mode is passing the AFC in its fiber direction. The excitation signal was a tone burst (5 cycles with a Hanning window) with a center frequency of 400 kHz and starting at $t = 50$ μs. As for the simulation (see example in Sec. 3.3.6), two wave packets can be obtained with a time shift of about 6 μs corresponding to the time needed by the wave to travel along the length of the AFC. From the measured IP surface velocity one can see that the incident wave pulse is elongated. The reason for it might be only weakly damped vibrations of the piezoceramic transducer which was used for excitation. This leads to an overlap of the two pulses in the electric voltage time history and thus to higher amplitudes of the second pulse. The pulses after 120 μs are then from the following A_0 mode and have relatively small amplitudes due to the poor sensitivity of the AFC at this frequency. The appearance of two wave packets seems reasonable since within a simplified consideration wherein the influence of the sensor on the wave field is neglected (see, e.g., [64]), the electric voltage would be proportional to the averaged IP surface strain over the sensor area, or the length of the sensor for the 2D case. The averaged strain over the entire length of a wave packet vanishes as long as the displacements before and behind the packet are equal to zero. Thus, if the wave packet is short enough compared to the AFC length, the electric potential vanishes as well when the entire wave packet is in between the two edges of the sensor and the wave packet is measured twice when passing the edges of the AFC. This can be observed whether an IDE is used (experiments) or not (simulations, see Sec. 3.3.6). In order to avoid such effects the sensor dimensions should be chosen as small as possible.

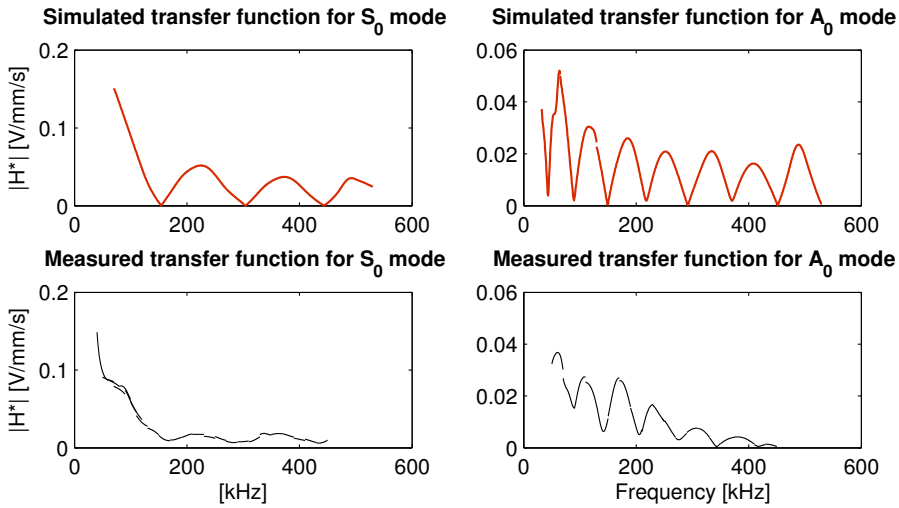

Figure 3.36: Simulated (upper diagrams) and measured (lower diagrams) transfer functions of the AFC as receiver for the S_0 mode (left diagrams) and A_0 mode (right diagrams). The excitation was achieved with the piezoceramic transducer positioned at $(r, \varphi) = (200, 0°)$.

Frequency Domain

A comparison between simulated (2DR1) and experimentally estimated (ExpR1) transfer functions is given in Fig. 3.36. The point of excitation was at (r, φ) = (200, 0°). As expected from theory [47], the transfer functions show minima and maxima due to the tuning effect. With decreasing frequencies the amplitudes increase and would theoretically end up in a maximum at zero frequency, where the wavelength to sensorlength ratio tends to infinity and the AFC would represent an ideal strain sensor. This can clearly be seen for the S_0 mode where the first maximum at 80 kHz as it was obtained for the AFC as emitter does not appear. It is mentioned here that within the experiment the lower limit of detectable frequencies given by the time constant of the applied measurement circuit was around 2 kHz (see page 52 in Sec. 3.4.2). Below this frequency the amplitudes would asymptotically decrease to zero. However, due to the long duration of the wave pulses at low frequencies and thus the overlaps with each other and with reflections from the boundaries of the plate, it was not possible with the used setup neither to measure nor to simulate useful data below 60 kHz and 50 kHz, respectively. Within the experimental results, some parts of the overall transfer function do not match with the neighbouring one. The reasons are the chosen window functions, not perfectly separated wave modes, and again a trigger rate which was chosen too high so contributions of reflected waves from the previous measurement were present particularly at lower frequencies.

As for the AFC as emitter the simulated transfer function for the S_0 mode agrees well with the measured one regarding the form of the curve and the frequencies of minima and maxima. For the A_0 mode the minima and maxima are slightly shifted to higher frequencies within the simulation. The reason might be the same as for the

AFC as emitter, namely the effective active length within the experiment which is something between the active length l_a and total length l_{tot}. It is noticeable that the amplitudes of the maxima of the measured A_0 transfer function decrease strongly with increasing frequency while for the simulation they remain almost constant. It is supposed that damping effects might be responsible for it.

It has to be mentioned that on the basis of this figure it is not possible to say whether the AFC is more sensitive to the S_0 or the A_0 mode because the IP and the OoP surface velocity has been taken into account to calculate the transfer function of the S_0 and A_0 mode, respectively. As reported in the literature ([47], [64]), it can be assumed that the AFC is mainly sensitive to the IP surface strain (in fiber direction). However, the IP surface velocity of the A_0 mode, which is related to the IP strain, is smaller than the OoP surface velocity (see also Fig. 2.2). By taking the IP surface velocity also for determining the transfer function of the A_0 mode would yield higher amplitudes than depicted here. Moreover, the amplitudes of the experimentally estimated S_0 transfer function are represented too small (around a factor of two) due to a poorly soldered connection between the AFC and the copper wire which was used for the electrical ground. The experiments have not been repeated because all piezoceramic transducers had already been removed. Hence, the results can only be compared qualitatively with the simulation.

The transfer behavior of the AFC for changing incident angles of the incoming wave was investigated only experimentally (ExpR1). The transfer functions for the angles $\varphi = 0°$, 15°, 30°, 45° and 90° to the fiber direction are shown in Fig. 3.37. Similar effects as for the AFC as emitter could be obtained.

- The amplitudes decreased with increasing angle φ due to the anisotropic behavior of the AFC, i.e. it was sensitive mainly to deformations (or strains) in its fiber direction. The decrease was less pronounced for the S_0 mode compared to the A_0 mode where the sensitivity was poor already for an angle of 30°. Perpendicular to the fiber direction both the S_0 and A_0 mode could still be measured for frequencies below 100 kHz although the amplitudes are rather small. The reason might be a weak coupling due to the transverse effect. Above 100 kHz the AFC was virtually not sensitive for both wave modes.

- The minima and maxima were shifted to higher frequencies for increasing angles. As a consequence, the amplitudes in the transfer function for the S_0 mode at frequencies around 150 kHz were higher at angles between 15° and 45° than for 0°.

- With increasing frequency, and thus with decreasing wavelength, the directionality of the receiving capabilities is more pronounced.

These effects can again be explained with a simplified consideration neglecting the influence of the AFC on the propagating wave in the plate and assuming that the voltage signal is proportional to the averaged IP surface strain in fiber direction over the AFC area. A plane wave field is assumed with the propagation direction r at an angle φ to the fiber direction of the AFC which corresponds to the z-direction

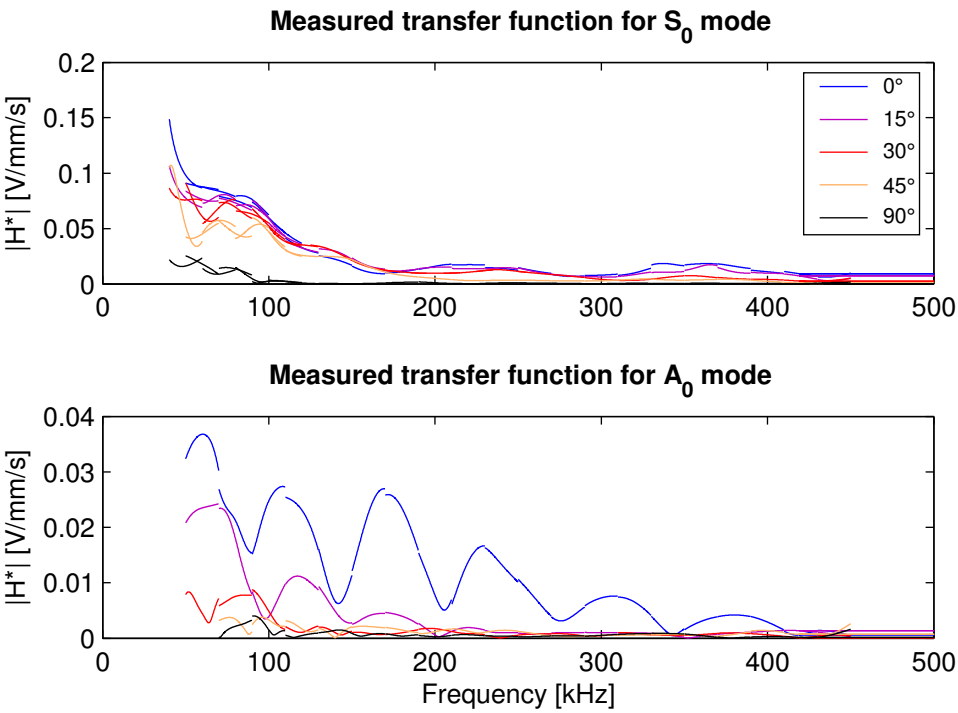

Figure 3.37: Measured transfer functions of the AFC as receiver for the S_0 mode (top) and the A_0 mode (bottom). for several incident angle. The excitation was achieved with the piezoceramic transducers positioned at $(r, \varphi) = (200, 0°\text{-}45°/90°)$.

(see Fig. 3.38). The variable of interest, here the IP strain in wave propagation direction, shall oscillate harmonically. By considering only the component in z-direction and integrating it over the rectangular active area of the AFC with the length l_a (in z-direction) and width w_a the following two terms can be obtained: $\sin(k\frac{l_a}{2}\cos\varphi)/(k\cos\varphi)$ and $\sin(k\frac{w_a}{2}\sin\varphi)/(k\sin\varphi)$. These terms are similar to those describing the wave field of the emitter (see Eq. (3.2)) except for the denominators $(k\cos\varphi)$ and $(k\sin\varphi)$. These denominators ensure that for frequencies decreasing to zero the amplitudes do not decrease to zero as well as it is the case for the transfer functions of the emitter. The first of the two terms is responsible for the minima and maxima in the transfer function and their shift with changing angle φ, while the second term describes the influence of the transducer's width to wavelength ratio on the directionally dependent receiving capabilities. An additional term is $\cos^2\varphi$ which is necessary for calculating the z-component of the IP surface strain. It causes the generally decreasing amplitudes with increasing angle. All three factors are also included in the analytical solution (see Eq. (3.3)) derived by Matt [47]. He additionally described the harmonic wave field with the exact solution for the surface strain of Lamb waves and took the constitutive relations for the AFC into account to solve for the electric voltage obtained at the electrodes. However, the influence of the AFC on the wave field and also the influence of the mechanical stresses within the AFC on the electrical quantities due to the coupled constitutive relations were

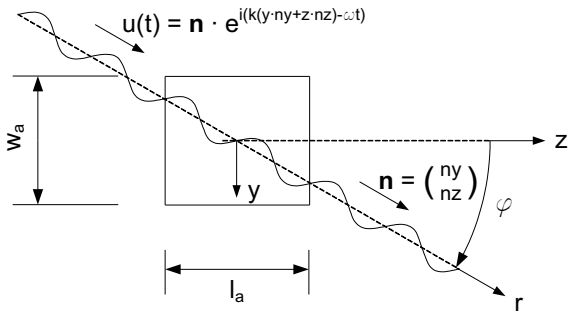

Figure 3.38: Simplified consideration of the AFC as receiver of a harmonic plane wave propagating in arbitrary direction.

not considered.

It can be concluded that similar effects as for the AFC as emitter were obtained. These are the typical minima and maxima in the transfer functions and the directionally dependent behavior. One difference between the emitter and the receiver is the transfer behavior at frequencies below the first minimum of the transfer function, where a maximum is theoretically reached at zero Hertz (see [38], [62]). Again, the simulation (performed only in fiber direction of the AFC) agreed well with the measurements.

3.6 Summary

The behavior of the AFC as emitter and receiver of elastic waves in isotropic plates was investigated. A model consisting of the plate and a surface bonded AFC was developed which allowed for simulating the process of exciting and sensing waves with the AFC. Additionally, experiments were performed. The wave field excited or measured by the AFC was observed free of contact with a laser interferometer. For both, the simulations and the experiments, transfer functions for the two fundamental Lamb wave modes (S_0 and A_0 modes) were determined to characterize the dynamic behavior of the AFC as emitter and receiver. The investigations showed that beside the Lamb wave modes the AFC also emits a SH mode in the considered frequency range. The transfer behavior is highly frequency and directionally dependent for the AFC as emitter as well as receiver. On the one hand the length and width of the AFC define the frequencies of minima and maxima in the transfer function – beside the wave propagation characteristic of the plate – as well as the concentration of the emitting and receiving capabilities on the fiber direction of the AFC. On the other hand the anisotropic material properties of the AFC enhance this directionality. Good qualitative and quantitative agreement between the simulated and experimentally measured results was achieved up to a frequency of 450 kHz.

Chapter 4

Application of AFCs for Damage Detection

4.1 Introductory Remarks

The suitablilty of AFCs as transducer elements for two different NDT methods for damage detection (first step of the damage identification process in SHM) is confirmed experimentally. The same AFCs are used as emitter and receiver in different frequency ranges. The structure to be monitored is an aluminum sandwich plate. Sandwich structures combine high bending stiffness with relatively low weight and are hence interesting for many different engineering applications. The plates used within this work consist of two aluminum face sheets and a hardfoam core. They are used in the transportation industry, e.g., for floor, wall, or roof constructions in trains or buses. It is known that one problem of such sandwich plates are delaminations between face sheet and core or failures (cracks or crushs) of the core material just underneath the bonding layer. These damages can be initialized by impacts or fatigue – often starting from structural features, e.g., embedded stiffeners between the two face sheets – and grow under cyclic loading.

Damage detection with acoustic NDT methods in an aluminum-hardfoam sandwich as used for the investigations presented here is not reported in the literature to the best knowledge of the author. More literature concerning this topic can be found for composite laminate-hardfoam or composite laminate-honeycomb sandwich plates (e.g., [4], [17], [42], [34], [90]) or aluminum-honeycomb sandwich plates (e.g., [68]) since these combinations have a wider range of applications for engineering structures. Nevertheless, the investigation of aluminum-hardfoam sandwich plates builds the first step toward more complex structures.

The two methods used for damage detection are the guided wave based method (GW method) and the electro-mechanical impedance method (EMI method). The former is a promising technique for monitoring large areas and detecting, locating, and evaluating different types of damage. The latter is interesting for the detection and a rough localization of a damage and can be further used for monitoring the transducer itself and its bonding to the structure. The two methods can be applied

for detecting different types of damages in the same structure. Wait et al. [84] used the GW method to identify cracks in aluminum plates and the EMI method to detect damages in connection joints. Thien et al. [79] adapted this approach to monitor steel pipes. Within both investigations MFCs were applied as transducer elements. Giurgiutiu et al. [27] used the EMI method to monitor the near field around the transducer and the GW method was used for larger areas. For both methods, they used conventional piezoceramic transducers. Hence, AFCs will be well-suited as well for being applied with both methods.

For the work presented here, damage detection means to obtain changes in a measured signal which can clearly be attributed to a damage of the specimen. Therefore, measurements were performed before and after a damage had been introduced. Since the experiments were carried out under laboratory conditions, it can be assumed that all other parameters which may influence the measurements remain constant, e.g., environmental conditions. Further signal processing and modelling which would be necessary in order to take such influences into account as well as to reach the next steps of the damage identification process in SHM (localization, evaluation of a damage) would go beyond the scope of this thesis. In order to estimate the reproducibility of the results, an artificial and reversible damage was introduced which allowed to reversibly switch between the undamaged and the damaged state.

4.2 Methods and Experimental Setup

4.2.1 Guided Wave Based Method

Guided or structural waves are elastic waves which propagate in wave guides such as plates or pipes. Their energy is guided within the boundaries of the structure and they can therefore propagate relatively long distances. Moreover, they are reasonably sensitive to damages located anywhere between the two boundaries since the waves produce stresses throughout the thickness [2] – as long as the frequencies are not too high since otherwise the waves would propagate only at the surfaces. For these reasons, guided waves (GW) are interesting for damage detection, particularly in SHM applications as the increasing number of publications in recent years indicates (e.g., [16], [21], [23], [34], [58], [75]). A review on GW based damage detection in composite structures can be found in [77].

The use of Lamb waves for NDT was first proposed by Worlton [89]. For damage detection it is required that the waves are sensitive to defects. Therefore, the interaction of the waves with different types of defects in plate-like metallic or composite structures was studied by several researchers (e.g., [2], [22], [41], [53], [68]). If a defect is present, the waves can be scattered, reflected, converted, attenuated, or shifted in phase. Depending on the defect type, certain wave modes may be better suited for detection due to stronger interaction with the damage. For delaminations between the face sheet and the core material of a sandwich structure (e.g., honeycomb plate), Rose [68] obtained that the amplitudes of the waves propagating in the face sheet were larger for the damaged then for the undamaged state since the

attenuation caused by the core was smaller.

Similar to classical ultrasonic testing, there are two general configurations for GW based damage detection, the pulse-echo and the pitch-catch configuration. For the former configuration only one transducer which is used as both emitter and receiver is needed and the reflected waves at defects are considered. For the latter two transducers are applied and the transmitted waves from the emitter to the receiver are evaluated. In a structure with a built-in SHM system the transducers are permanently attached to or embedded into the structure to be monitored. For monitoring large structures, several transducers might be connected to a sensor network where each transducer acts once as emitter and otherwise as receiver. Further, a permanently installed monitoring system allows for performing measurements throughout the life of the structure. Hence, measurements can be compared with a baseline (or reference) measurement carried out at the beginning of the monitoring period. With the assumption that changes in the measured signals are caused only by damages, the difference between the actual measurement and the baseline measurement can be considered. The determination of the difference allows for eliminating signal features from any existing structural components and enables the GW method to be applied also to more complex structures than plates or pipes.

Important factors for GW based damage detection are the properties of the monitored structure, type and coupling of the transducers, types of excitation signals, optimal sensor location, sensor validation, and signal processing ([85], [74]). The structure which is used for the investigations presented here is an aluminum sandwich plate. To find out its properties concerning wave propagation and damage interaction, preliminary investigations were performed (Sec. 4.4). Beside AFCs, also MFCs and piezoceramic transducers were applied since these are commercially available. The transducers were permanently mounted on the surface of the specimen. In order to determine the optimal length of the AFCs/MFCs, the findings from the characterization of the AFC (Chap. 3) are used. The considered frequencies were between 40 kHz and 440 kHz which is a reasonable range for Lamb wave based damage detection and for the application of AFCs although the A_0 mode within a 1 mm thick aluminum plate is highly dispersive in this region. Only simple signal processing was performed (see below) since only changes in the measured signals caused by a damage should be observed. Other aspects such as sensor validation, reliability, or environmental influences would go beyond the scope of this thesis.

Setup

The experimental setup is shown in Fig. 4.1. Except for the use of the laser interferometer, the setup and the instruments were the same as those used for the investigation of the AFC as receiver (see Sec. 3.4.2 for details). The excitation signal was generated as a vector with discrete values with sufficiently high resolution in time in a computer with LabVIEW® and uploaded via GPIB to the function generator which converted the vector into an analogue voltage signal with an amplitude of 1 V or 2 V. The signal was amplified by a factor of 100:1 before being guided to the piezoelectric transducer used as emitter. To monitor the amplified excitation

signal it was additionally sent through a voltage divider. Both the signal sent to the emitter and the signal from the receiver were visualized by an oscilloscope and digitized either with the NI-card or the oscilloscope, both triggered by the function generator. The sampling frequency was set to 10 MHz and the record length to 5'000 or 10'000 samples. In order to minimize random errors each measurement was repeated 100 times with a trigger rate of 50 Hz. The data were averaged before being saved on the computer.

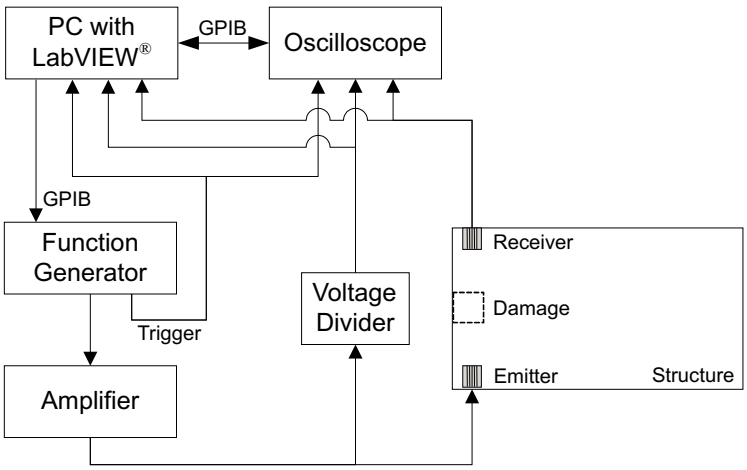

Figure 4.1: Schematics of the experimental setup for the investigations with the GW method.

As excitation signal, a sinusoidal tone burst with 5 cycles modulated with a Hanning window was used due to its limited frequency content in spite of its short duration. Measurements were consecutively performed with increasing center frequencies from 50 kHz to 400 kHz in steps of 50 kHz or from 40 kHz to 440 kHz in steps of 20 kHz. In order to control the whole measurement procedure – including the generation of the excitation signal, the data acquisition, and data storage –, the same LabVIEW®-routine as used for the characterization of the AFC (see Sec. 3.4.2) is used.

Processing

As already obtained in the experiments for the characterization of the AFC used as receiver, the voltage signal measured with the piezoelectric transducer was superposed by a sinusoidal voltage signal with a frequency of 50 Hz caused by the power supply of the measurement instruments and induced over the electrical ground. Since the duration of the recorded signal was much shorter than the period of the disturbance, the signal seemed to be superposed with a linear function. Therefore, every measured signal was corrected by subtracting its linear regression curve before further signal processing.

Beside considering the corrected time histories before and after a damage occurred, the difference of these two signals were determined in order to point out the

changes caused by the damage. Since the difference of the time signals is sensitive to phase shifts between the two signals, e.g., caused by temperature shifts [16], the envelope function, based on the Hilbert transform, was calculated for all considered time histories. For a better comparison with the amplitudes of other measurements, the time signal was additionally transformed with conventional FFT techniques into the frequency domain and the amplitude spectrum of the discrete Fourier transform (DFT) was plotted. Before the transformation, a Tukey window was superposed on the time signal for extracting the time sequence of interest. The FFT was performed with 2^{18} points although the record length was much shorter (zero padding, see Sec. 3.2.4 for details). All signal processing was carried out with MATLAB®.

4.2.2 Electro-Mechanical Impedance Method

Impedance denotes the ratio between input and output of a system. The mechanical impedance of a structure is hence defined as the ratio between a harmonic excitation, e.g., an external force acting on the structure, and the structural response, e.g., the velocity at an arbitrary point of the structure, in the stationary state. It includes therefore mass, damping, boundary conditions, stiffness and spatial location and it is a frequency dependent complex number. A structural damage will yield changes in the stiffness and damping characteristics of the structure and hence affects its mechanical impedance. For the electro-mechanical impedance methode (EMI method) the same piezoelectric transducer bonded to the structure is used for exciting the structure as well as for measuring its response [44]. Due to the electromechanical coupling of piezoelectric material, changes in the mechanical impedance of the structure can be observed by monitoring the electrical impedance of the bonded transducer and by comparing this to a baseline impedance measurement. The frequency dependent complex electrical impedance of an electrical device is defined as the ratio between the applied, alternating electrical voltage and the resulting current in the stationary state. The former is needed for the excitation while the latter contains the response of the coupled transducer-structure-system and hence informations about the mechanical impedance of the structure.

The use of electro-mechanical impedance measurements with bonded piezoelectric elements for SHM was first proposed and theoretically investigated by Liang et al. [44] and subsequently developed in particular by the groups around Liang and Rogers (e.g., [78]), Park and Inman (e.g., [59], [57], [61], [73]), and Giurgiutiu (e.g., [25], [26]). An overview on piezoelectric impedance-based health monitoring is given in [60]. Liang et al. [44] described a one-dimensional coupled electromechanical model consisting of an axial PZT transducer which is attached on one end to a single degree-of-freedom spring-mass-damper system and fixed on the other end. The electrical admittance, which is the inverse of the electrical impedance, is then given by

$$Y(\omega) = i\omega a \left(\bar{\varepsilon}_{33}^{\sigma} - \frac{Z_S(\omega)}{Z_S(\omega) + Z_P(\omega)} d_{3x}^2 \bar{Y}_{xx}^E \right) \tag{4.1}$$

where a is a geometry constant for the PZT, $\bar{\varepsilon}_{33}^{\sigma}$ is the complex dielectric constant

of the PZT element at constant stress, Z_S and Z_P are the mechanical impedance of the structure and the PZT element, respectively, d_{3x} is the piezoelectric constant, and $\bar{Y}_{xx}^E$ is the complex Young's modulus of PZT at constant electric field. For the EMI method it is assumed that the mechanical and electrical properties of the PZT remain constant over the period of monitoring. Hence, as shown in Eq. (4.1), changes in the mechanical impedance Z_S of the structure uniquely affects the electrical admittance (or impedance) of the bonded PZT element. Consequently, changes in the electrical admittance can be attributed to structural damages. The electrical admittance is primarily capacitve since PZT is a dielectric and the imaginary part of the admittance is dominant ($Y = i\omega a\bar{\varepsilon}_{33}^{\sigma}$, where $a\bar{\varepsilon}_{33}^{\sigma}$ corresponds to the capacitance of the PZT). However, the dielectric constant $\bar{\varepsilon}_{33}^{\sigma}$ shows relatively large temperature dependence and, therefore, the real part of the admittance (or impedance) is mainly used for monitoring applications [60]. Further, changes in the mechanical impedance of the structure are more distinctly exhibited in the resistive portion (real part) of the electrical impedance of the PZT element [60]. The imaginary part, on the other hand, is more sensitive to changes in the properties and the coupling of the PZT element [27]. The EMI method typically utilizes frequencies in the tens to hundreds of kilohertz range. With increasing frequency the sensing region of the transducer decreases but the sensitivity to smaller defects increases [60].

The electrical impedance signature of the transducer bonded to the structure will contain resonance peaks of the coupled transducer-structure system. In order to reduce the contributions of the transducer behavior, a non-resonant transducer is well suited for the EMI method. By using an AFC which is permanently bonded to the structure, the strong coupling leads to a non-resonant behavior which is dominated by the dynamics of the structure. Further, the coupling enhances the energy transfer from the transducer to the structure and vice versa. This is important in order to excite the structure and to measure its response.

The application of the EMI method with surface bonded AFCs for damage detection in various model structures such as composite plates or bonded joints has already been investigated at Empa (e.g., [5]). It has been shown that AFCs are generally suitable for this purpose. Hence, no preliminary investigations were necessary as for the GW method.

Setup

In order to simultaneously measure the voltage and the current over an electrical impedance Z, here the piezoelectric transducer bonded to the structure, a resistor R in series with the impedance Z was used [5] (see Fig. 4.2). With the measured voltage over the resistor R, the current through it, which is equal to the current through the impedance Z, could be calculated. For recording a spectrum, the impedance was measured stepwise at changing frequencies. At each step a harmonic voltage $V_{ex}(t)$ was applied and the two voltage signals $V_R(t) = Ri(t)$ and $V_Z(t)$ were recorded. The whole measurement procedure (generation of the excitation signal, measurement, and storage) was performed and controlled with LabVIEW® installed on a computer and for the digitization of the voltage signals to be measured an analog-digital

converter with two channels for simultaneous recording (type NI PCI-6115 from National Instruments) was used. In order to determine the complex impedance for each frequency, amplitude and phase of the two digitized voltage signals relative to each other were calculated in LabVIEW® with a process similar to the principle of a lockin amplifier. Several, usally three, measurements were averaged to yield one data point, each containing the frequency, the real and imaginary part of the complex impedance. The measurement system, which was developed at Empa before this project has started, allowed for measuring the electrical impedance in the range between about 100 Hz and about 2 MHz with excitation voltages up to 5 V. The electrical impedance of the test setup including the cables (except for the short contact wires of the piezoelectric elements) was determined separately and accounted for.

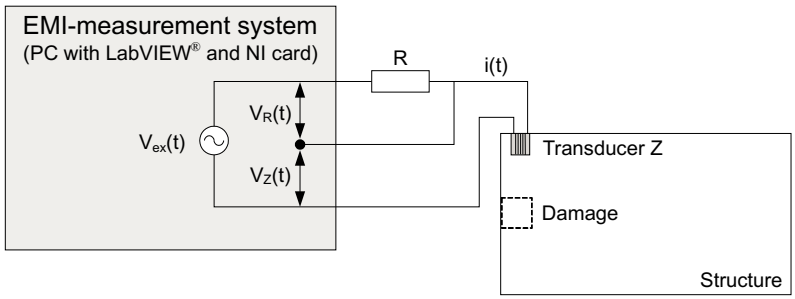

Figure 4.2: Schematics of the experimental setup for the investigations with the EMI method.

Processing

The impedance spectra is plotted as real and imaginary parts, Re(Z) and Im(Z), of the complex impedance Z. Since for damage detection the real part is of major interest (see above), only this part was considered. Beside the measured spectra before and after a damage occurred, the difference between the two spectra was determined and plotted to emphasize the changes. No further analyis was performed since it should only be demonstrated that changes caused by a damage were observable. The signal processing was carried out with MATLAB®.

4.3 Materials

4.3.1 Test Specimen

The structure to be monitored was an aluminum sandwich plate. It consisted of aluminum face sheets with a thickness of 0.9 mm or 1 mm. The core material was a hardfoam (C70.55 from Alcan Airex AG, Sins, Switzerland) with a thickness of 30 mm. The face sheets and the core material were compounded under pressure with a two component adhesive (Collano A 2112 from Collano Adhesives AG, Sempach,

Switzerland). Several plates with different dimensions were used. A quadratic plate (indicated as Pl-A) with the dimensions of 1,400 mm × 1,400 mm × 31.8 mm with two 0.9 mm thick face sheets on each side of the core was produced by Alcan Airex AG, Sins, Switzerland. Other plates with smaller dimensions (see text below) were produced at Empa and consisted of the core material and one 1 mm thick face sheet bonded to one side of the core.

4.3.2 Transducers

Three types of transducers were used. For the preliminary investigations piezoceramic disc transducers (type PZ26 from Ferroperm-Piezoceramics, Denmark) with a polarization through the thickness were applied since they are cheap and commercially available. The dimensions are 10 mm in the diameter and 1 mm in the thickness for all elements used for this part of the thesis. They are permanently bonded and electrically contacted as already described in the previous chapter (see Sec. 3.4.1). For one test series two shortened MFCs with an active length of l_a = 16.5 mm were used (designated to MFC-1 and MFC-2) since MFCs were commercially available and, hence, cheaper than the hand made AFCs. They were cut from a commercially available MFC (type M-8528-P1 from Smart Material GmbH, Dresden, Germany) with an active area of 50 mm × 20 mm. The length of the shortened MFC has been chosen in order to get a maximum for the A_0 and a minimum for the S_0 mode in the transfer functions at a frequency of 300 kHz when the MFC is bonded on a 0.9 mm thick aluminum plate although it was bonded on the sandwich plate. However, as shown in the next section, the transfer behavior is approximately similar. For the final experiment two AFCs (designated as AFC-4 and AFC-5) with standard design were shortened to an active length of l_a = 20 mm which yielded a maximum for the A_0 mode and a minimum for the S_0 mode at a frequency of about 235 kHz when the AFC is bonded on a 1 mm thick aluminum plate. In order to minimize the discrepancy between the predicted and the effective transfer behavior caused by the effective active length of the AFC (see page 60 in Sec. 3.5.1), the total length l_{tot} has been set to 21 mm. A total length equal to the active length was not possible without damaging the electrodes. The procedure of cutting, bonding (permanently), and contacting the MFC/AFC is essentially described in Sec. 3.4.1. The dimensioning process for the MFC/AFC is described on page 67 in Sec. 3.5.1.

4.4 Preliminary Investigations on a Sandwich Plate

Experiments were performed to separately investigate some aspects of wave propagation and damage detection in a sandwich plate. The investigations are guided by the following questions:

- What kinds of wave modes propagate in a sandwich plate as described above?
- How do delaminations affect the waves propagating in such a plate?

- How can artificial and reversible delaminations produced and how realistic are these artificial damages?
- How can the directionally and frequency dependent emitting and receiving capabilities of AFC be used in a profitable way?

4.4.1 Wave Propagation

The wave propagation in the aluminum sandwich plate was investigated experimentally and numerically. For the experiments a piezoceramic disc transducer was bonded to the center of the quadratic plate (Pl-A). The transducer was excited with a tone burst (5 cycles with a Hanning window) with specific center frequencies between 50 kHz and 400 kHz. The peak-to-peak amplitude of the amplified excitation signal was around 400 V. The radial IP and OoP component of the surface velocity at several points at increasing distance from the transducer were measured with the laser interferometer (see Sec. 3.4.2 for details) on either side of the sandwich plate. For the measurements, the plate was mounted vertically with cords fixed at the two upper corners to achieve virtually free boundary conditions.

Simulations were performed with the help of the 2D model presented in the previous chapter. The model was extended with the core material which was added underneath the aluminum plate with the surface bonded piezoelectric element. The core material was assumed to be linear elastic, isotropic, and homogeneous (elastic modulus E = 69 MPa, Poisson's ratio $\nu = 0.4$, density $\rho = 60$ kg/m^3, according to the manufacturer's data sheet). The bonding layer between plate and core was neglected as well as the face sheet on the opposite side of the core and any energy dissipation. Further, to simplify matters, the same piezoelectric element as already programmed for the investigation of the AFC was used, i.e. the polarization is along the plate instead of perpendicular to it and the material parameters are equal to those of the AFC. However, the dimensions were adjusted to those of the piezoceramic transducer used within the experiment. It is mentioned that for the 2D model a plane strain state in a cartesian coordinate system was assumed, i.e. the piezoelectric element and the plate are infinitely wide along the direction perpendicular to the cross section represented by the model. On the other hand, the situation in the experiment in which piezoceramic discs were applied is rotation-symmetric. For all these reasons a comparison of the simulation with the experiment can only be done qualitatively.

Fig. 4.3 depicts the total displacements in the cross section through the aluminum face sheet and the core material 60 μs after excitation with a center frequency of 100 kHz. A faster and a slower wave packet can be seen in the aluminum plate. In spite of the presence of the hardfoam the waves are approximately equal to the S_0 and A_0 Lamb wave modes in a plate with traction-free boundaries. This is reasonable since the acoustic impedance (density times wave velocity) for the aluminum is more than hundred times higher than for the hardfoam, i.e. most energy is reflected at the interface like at a free boundary. In the core material bulk waves appear since the core's thickness is much larger than the wavelengths ($\lambda_{core} \ll d_{core}$). Each Lamb wave mode which propagates in the face sheet excites P and SV waves in the

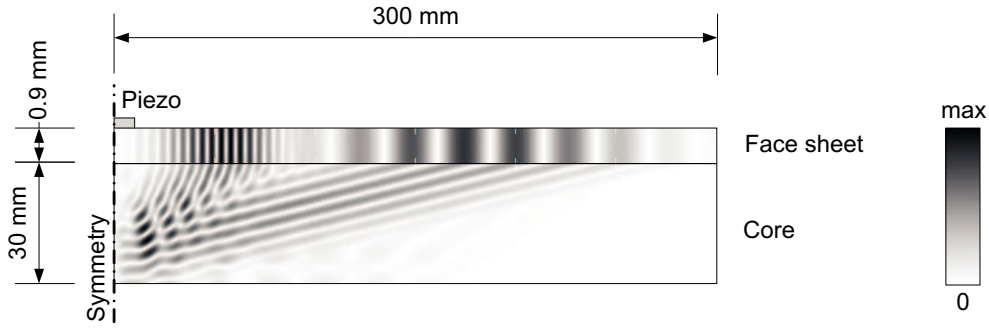

Figure 4.3: Total displacements calculated with the 2D model in a cross section through the aluminum face sheet and the core material 60 μs after initiation of the excitation (5-cycle tone burst, Hanning window, center frequency of 100 kHz). The thicknesses are enlarged for better visualization.

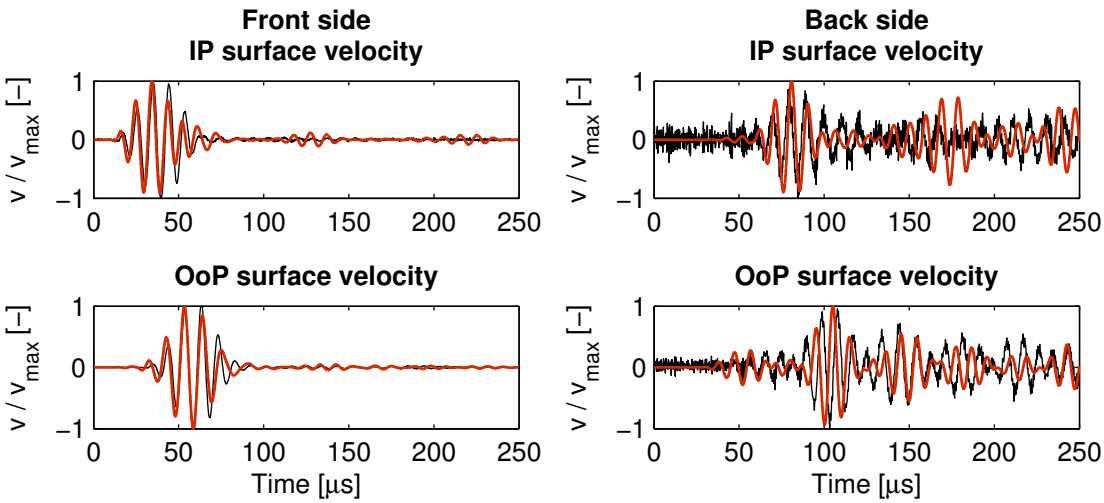

Figure 4.4: Simulated (red) and measured (black) IP (upper diagrams) and OoP (lower diagrams) surface velocities on the front (left diagrams) and back (right diagrams) side of the plate, normalized by the maximal amplitude of each dataset. For the simulation, the data for the back side correspond to the velocities at the lower free surface of the core material, while for the experiment they correspond to those at the free surface of the lower face sheet. The velocities were recorded in a distance of 50 mm from the transducer used for excitation (5-cycle tone burst, Hanning window, center frequency of 100 kHz).

core. The obtained wave field within the core can be explained with the Huygen's principle.

It is expected that similar to the upper face sheet Lamb wave modes would be developed also in the lower face sheet as soon as the bulk waves within the core reach the lower interface. But again only little energy would be transmitted to the aluminum plate due to the mismatch in acoustic impedance. Although the lower face sheet is not modeled, a qualitative comparison with experimental results

is given in Fig. 4.4. The time histories for the IP and OoP velocity, normalized by the maximal amplitude of each dataset, were recorded in a radial distance of 50 mm from the excitation point and on both sides of the sandwich plate. For the simulation, the velocity on the lower free surface of the core material is presented. On the front side the first wave packet with mainly IP components corresponds to the S_0 mode, followed by the A_0 mode with mainly OoP components. Results from the simulation and from the experiment are in good agreement. On the back side the situation is much more complex but still good agreement is achieved. The retardation corresponding to the time needed by the wave to travel through the core can easily be seen in both, the simulation and the experiment. This confirms the results from the simulation. It has to be mentioned that for the measured time histories shown in Fig. 4.4 the maximal amplitudes of the IP and OoP surface velocities measured on the back side are about 13 and 50 times, respectively, smaller than on the front side. This explains also the signal-to-noise ratio which is poorer on the back side.

One can conclude that for a sandwich plate as used here and in a frequency range where the core's thickness is much larger than the lengths of the wave within the core material ($\lambda_{core} \ll d_{core}$) the waves propagate mainly in the face sheet where the excitation was applied. Only little energy is transmitted to the core material. The waves within the face sheet are approximately equal to Lamb waves, and no wave modes through the whole thickness of the sandwich plate exist in the considered frequency range. Consequently, the findings as presented in the former chapter, particularly the transfer functions, are approximately valid also for the sandwich plate as used for this part of the work.

4.4.2 Damage Detection

Several series of measurements with the GW method on the quadratic sandwich plate (Pl-A) were carried out in order to examine the effect of delaminations between face sheet and core material on the wave propagation. The delaminations were achieved mechanically by punching a 1 mm thick and 12 mm or 50 mm wide steel sheet between plate and core, starting from the edge of the sandwich plate. This allows for measuring the reference state without any damage and, hence, for obtaining changes in the measured signals after the damage is introduced. The wave pulses were excited and measured with the help of surface bonded piezoceramic disc transducers or MFCs in a pitch-catch configuration. Laser measurements were additionally performed which allows for observing free of contact the propagating waves at any point on the plate surface. For the measurements, the plate was mounted vertically either by hanging it up with the two cords fixed at the corners or by putting it down on the floor on one edge and leaning it against a table for stabilisation. Pieces of hardfoam were positioned between the plate and the floor or the table, respectively, to minimize the influence of the supporting points. Moreover, the plate was positioned in such a way that the supporting points were as far away from the delamination and transducers as possible. Since the findings were similar

for all measurement series, the results of two series are presented here for illustrating the behavior.

Delamination Detection with Piezoceramic Transducers

Two piezoceramic disc transducers (10 mm in diameter, 1 mm in thickness, designated as P1 and P2) were bonded on the front side of the sandwich plate at a distance of 50 mm from one of the plate's edges. The distance between the two transducers was 300 mm (see Fig. 4.5). All other boundaries of the plate were far away so that reflections could not interfere with the waves of interest. First, measurements at several frequencies as described in Sec. 4.2.1 were carried out for recording the baseline. Then, a delamination in a distance of 200 mm from the transducer P1 and with an area of nominal 10 mm × 150 mm was introduced just underneath the front face sheet with the help of the 12 mm wide steel sheet (damage state 1, DS-1). Repeated measurements have been performed before and after the delamination was extended with the 50 mm wide steel sheet to an area of nominal 50 mm × 150 mm (DS-2).

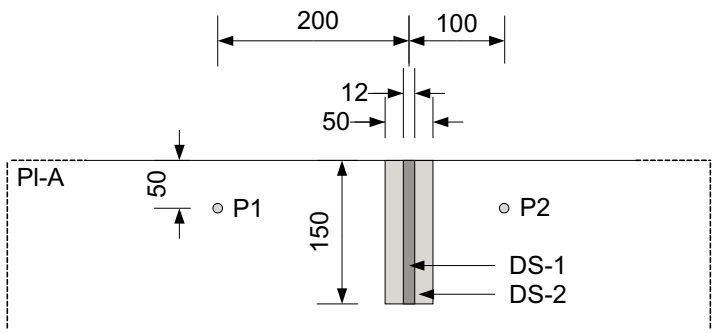

Figure 4.5: Schematic arrangement (dimensions in [mm]) for the delamination detection in the aluminum sandwich plate with piezoceramic transducers.

Fig. 4.6 shows in the upper diagram the envelopes before (baseline) and after the first delamination step. Since the differences between the two time signals is relatively small, only the time history of the undamaged state is depicted for better visualization. The excitation signal (5-cycle tone burst, 300 kHz, 400 V peak-to-peak, Hanning window, starting at $t = 50$ μs) was applied to the transducer P1, while transducer P2 was used as receiver. The first measured pulse at 50 μs appeared due to electro-magnetic coupling over the electrical ground (aluminum plate for both transducers) and should be ignored. The wave packet arriving at 110 μs corresponds the S_0 mode. There are much more cycles than within the excitation signal which can be attributed to vibrations of the emitting transducer, whose first planar resonance frequency was near below the center frequency of the excitation signal. The excitation of the planar resonance with mainly IP deformations explains also why the A_0 mode which arrives at 160 μs has much smaller amplitudes than the S_0 mode. The diagram in the middle shows the difference of the two measured time signals. It indicates that changes were observable for both wave modes. The

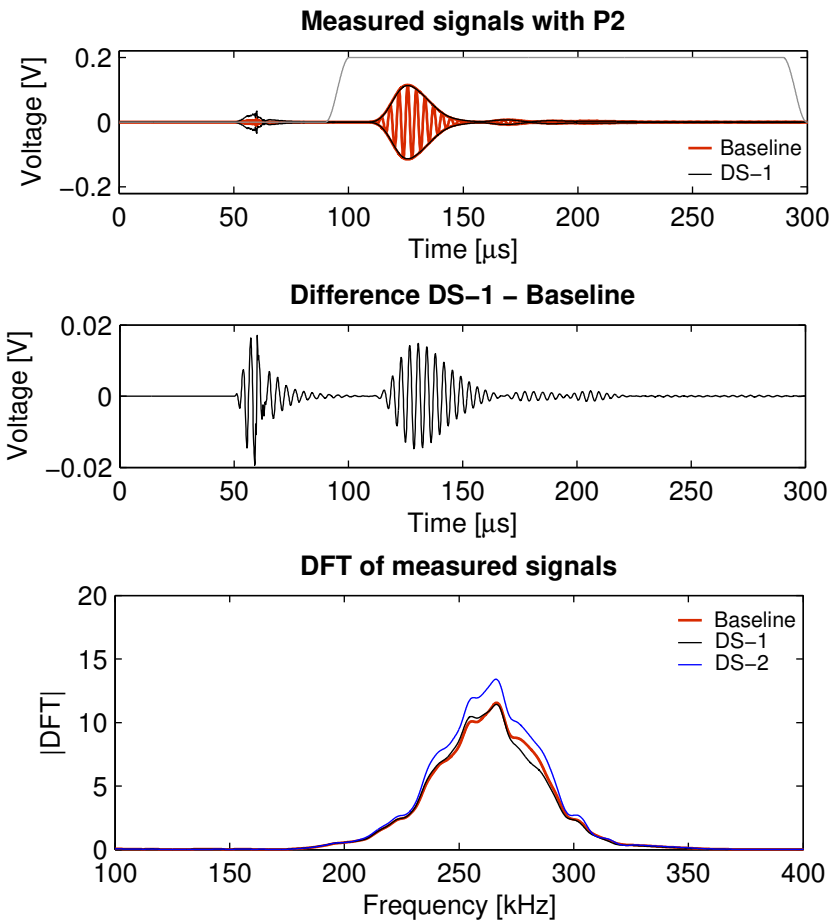

Figure 4.6: Results of the measurements with the disc transducer P2: time history and envelopes of the undamaged state (red) and envelopes of the damage state DS-1 (black) and the time window used for calculating the DFTs (top); the difference of the two time signals (middle); and the amplitude spectra of the DFTs for all damage states (bottom). Transducer P1 was used for excitation (5-cycle tone burst, Hanning window, center frequency of 300 kHz, starting at $t = 50$ μs). The pulse at 50 μs appeared due to electro-magnetic coupling over the electrical ground and should be ignored.

differences within the S_0 mode seem to be relatively large although the amplitudes in the measured signals are almost equal. The reason for this are small phase shifts which may have been caused by the damage or by even small variations in the room temperature; a temperature difference of 2°C which is in a realistic range leads to a time shift of approximately 0.03 μs (estimated as described in [16]). This is in the range of the time shift between the measured signals. Therefore, for all results presented below, the respective measurements were carried out in a relative short time period so the temperature can be assumed to be constant. To emphasize the changes in the amplitudes one can consider the differences of the envelopes or the amplitude spectrum of the DFT. The lower diagram depicts the DFTs of the time signals of the damage-free state and the two damaged states. The time window used for the calculation of the DFT was set from 90 μs to 300 μs, i.e. both wave modes were included. Although the center frequency of the excitation was at 300 kHz, the main peak is around 260 kHz which corresponds to the planar resonance frequency of the emitter and the receiver. The changes from the baseline to the first damage state are small and vary over the respective frequency range. While for frequencies around 250 kHz the amplitudes are increased after the delamination compared to the baseline, the amplitudes decrease for frequencies around 280 kHz. However, for the extended delamination the amplitudes increased significantly over the whole frequency range. This seems reasonable since less energy is transmitted to the core when a delamination right underneath the face sheet is present. Similar results were presented by Rose for a honeycomb structure [68].

By looking also at the evaluations at other frequencies and at the results of additional measurement series (not shown) it turned out that the amplitudes of both wave modes increase compared to the baseline as long as the waves propagate over the delaminated area. This effect seems to be more pronounced for frequencies above 200 kHz and for larger delaminated area. This is reasonable since the ratio of the damage size to the wavelength is larger. Significant changes in the signals will be only obtained if the delaminations were introduced underneath the face sheet where the transducers were placed. Delaminations on the opposite side of the core could not be detected by these transducers. This is reasonable since virtually no energy is transmitted through the core material. Further, scattering effects, reflections, or mode conversions at the defect could not be observed with the setup and measurement procedure used for the experiments presented here. However, it can not be concluded that such effects are not present.

Some of the measurements were also performed with reduced voltage amplitudes of the excitation signal. The same results could be obtained even if the emitter is excited with only 10 V instead of 200 V like for the experiments presented above.

Delamination Detection with MFC

The arrangement of two MFCs (MFC-1 and MFC-2) in a pitch-catch configuration and the delaminated area is given in Fig. 4.7. The MFC were positioned at a distance of 200 mm from the defect which was located in the middle of one edge of the quadratic sandwich plate (Pl-A). The fibers of the MFC were oriented in

an angle of 45° to the edge of the plate in such a way that the waves emitted in fiber direction were reflected at the boundary of the plate and propagated then in fiber direction of the receiver. Other boundaries were sufficiently far away so that unwanted reflections did not disturb the wave packets of interest. The MFC had an active length of 16.5 mm which resulted in a maximum and minimum in the transfer function of the S_0 and A_0 mode, respectively, at 300 kHz for the 0.9 mm thick face sheet. This was chosen in order to excite mainly the A_0 mode which is much more focused on the fiber direction than the S_0 mode. The delamination underneath the plate with the surface bonded MFCs was introduced in four steps. First, the 12 mm wide steel sheet was punched into the bonding layer between face sheet and core up to a depth of 50 mm (DS-1) and later to 100 mm (DS-2). Then, the wider steel sheet was used to widen the delamination to 50 mm again up to a depth of 50 mm (DS-3) and later to 100 mm (DS-4). Before and after each damage state measurements were performed as described in Sec. 4.2.1. For comparison, piezoceramic disc transducers (designated as P3 and P4) were used with the same arrangement and measurement procedure but on another edge of the sandwich plate (Pl-A).

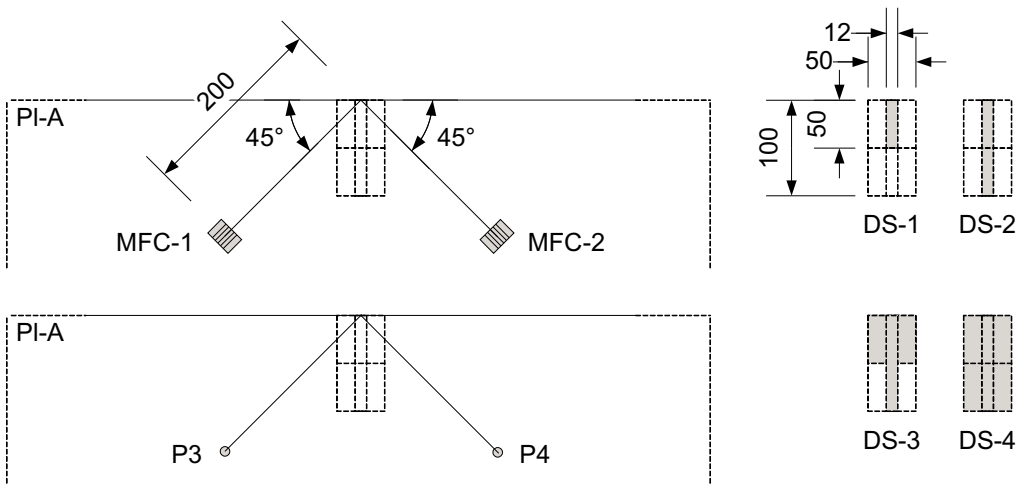

Figure 4.7: Schematic arrangement (dimensions in [mm]) for the delamination detection in the aluminum sandwich plate with MFCs.

After glueing the first MFC, laser measurements were carried out for investigating the emitting capabilities of the MFC and for determining the undisturbed surface velocity at the position where the second MFC would be placed. Transfer functions for the S_0 and A_0 mode as described in Chap. 3) were estimated. For this, the MFC was excited with tone burst signals (5 cycles within a Hanning window) at varying center frequencies and the IP and OoP surface velocities at a distance of 100 mm in fiber direction from the center of the MFC were measured. Reflections from the boundary of the sandwich plate prevent from measuring the undisturbed transfer functions, however, a minimum of the S_0 mode and a maximum of the A_0 mode at a frequency of 300 kHz could be observed (see App. D.1). In spite of the maximum in the transfer function at 300 kHz, the emitted A_0 mode was virtually not

detectable with the laser interferometer at the position of the second MFC because it was damped out almost completely after propagating over a distance of 400 mm and being reflected at the boundary (see App. D.2). The S_0 mode had also small amplitudes which was expected due to the minimum in the transfer function. By way of contrast, the waves, in particular the S_0 mode, excited by the piezoceramic transducer (P3) at the same frequency could still be measured in a distance of 400 mm. This seems reasonable since the resonance of the disc transducer leads to larger deformations during electrical excitation and thus to higher amplitudes of the emitted waves. For all these reasons the data were evaluated at 100 kHz instead of 300 kHz. Diagrams of the laser measurements at the position of the receiver are presented in App. D.2.

Fig. 4.8 shows the results of the measurements from MFC-1 to MFC-2 and from P3 to P4 for different damage steps. The emitter (MFC-1 or P3) was excited with a tone burst (5 cycles with a Hanning window) at a center frequency of 100 kHz and with a peak-to-peak amplitude of around 400 V. The excitation started at $t = 50$ μs. The time signal in the upper diagrams was recorded with the receiver (MFC-2 and P4) for the damage state DS-2. The envelopes are drawn for the damage states DS-2 and DS-3. The diagrams in the middle show the difference of the time signals of DS-2 and DS-3. However, the DFTs in the lower diagram are given for the baseline and the damage state DS-4. The DFTs were calculated from the time signals within a time window from 100 μs to 390 μs, i.e. all wave modes are included which explains the appearance of several peaks in the spectra (constructive or destructive interferences of the wave packets with each other).

The well marked wave packets measured with the piezoceramic transducer P4 correspond one after the other to the direct S_0 mode (arrival time $t = 105$ μs) which also overlapped with the S_0 mode reflected from the boundary of the plate ($t = 125$ μs), to the direct A_0 mode ($t = 220$ μs approximately), and to the reflected A_0 mode ($t = 290$ μs approximately). The waves after 370 μs are then reflections from other boundaries of the plate. The reflected S_0 and A_0 mode are also indicated in the difference of the time signals where relatively large changes due to the delamination can be seen in the corresponding time range. From the results for all damage states, it was obtained that the deeper the delamination the more affected were the waves which propagated on the direct path.

Two major differences between the measurements with the disc transducer and the MFC can be obtained. First, there is an additional well marked wave packet within the time signal from MFC-2 with maximal amplitudes at $t = 170$ μs. On the one hand, this wave packet might be attributed to the reflected S_0 mode which should have larger amplitudes due to the directionally dependent emitting and receiving capabilities of the MFC than the reflected S_0 mode measured with the disc transducer. On the other hand, the additional wave packet might be the SH_0 mode which was emitted by the MFC-1 at an oblique angle to its fiber direction, propagated toward the receiver on the direct path, and theoretically arrived there at $t = 140$ μs. Second, the direct A_0 mode as expected has much smaller amplitudes when excited and measured with the anisotropic MFC than with the disc transducers.

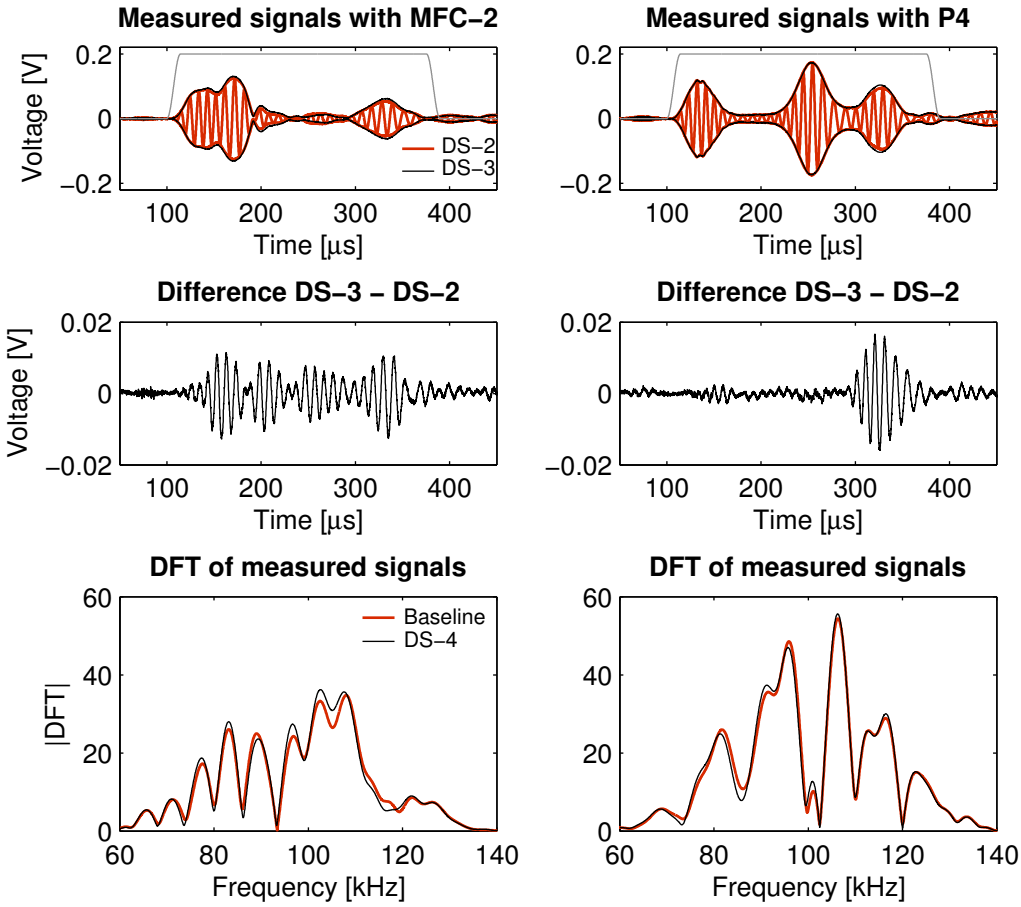

Figure 4.8: Results of the measurements with the MFC-2 (left diagrams) and the disc transducer P4 (right diagrams): time histories and envelopes for the damage state DS-2 (red) and envelopes of DS-3 (black) and the time window used for calculating the DFTs (top); the difference of the two time signals (middle); and the amplitude spectra of the DFTs (bottom) for the undamaged state (red) and damage state DS-4 (black). MFC-1 and disc transducer P3 was used for excitation (5-cycle tone burst, Hanning window, center frequency of 100 kHz, starting at $t = 50$ μs).

Regarding the difference of the time signals from the MFC-2, it can be seen that it varies significantly also between 190 μs and 300 μs, i.e. within the time range between the reflected S_0 and A_0 modes. The causes for these changes and why they are more pronounced for the MFC are not obvious. One possibility might be converted wave modes from the boundary and/or the delaminated area which are better detected by the MFC than by the disc transducer and which are more affected by changes in the specimen.

One can say that relative to the total emitted energy more energy is emitted toward and received from the damaged area when MFCs are applied than when disc transducers are used. Therefore, the relative variations in the signals measured with the MFC should be theoretically more pronounced. This seems to be confirmed when looking to the lower diagrams of Fig. 4.8 where the DFTs for the baseline and the damage state DS-4 are depicted. The difference between the two DFTs – an increase in the amplitudes for most frequencies – is much larger for the measurement with the MFCs than for that with the disc transducers. However, it must be mentioned that not the same delamination was measured with the two transducer types, i.e. differences in the introduced delaminations might lead to similar findings. Hence, with the results from this investigation it is not possible to conclude whether the application of the MFC with its directionally dependent behavior or of the disc transducers with its rotation-symmetric behavior is advantageous. For a quantitative comparison of the performance of different transducer types, it is therefore essential to be able to introduce artificial damages in a reproducible and reversible way.

4.4.3 Reversible Delamination

It is known from the investigation of the wave propagation in the sandwich plate that no wave modes through the whole thickness of the plate exist in the considered frequency range ($\lambda_{core} \ll d_{core}$) and that only little energy is transmitted through the core material. Hence, for this type of sandwich, for the wave which propagates in one of the face sheets it does not matter whether the other face sheet is present or not. Therefore, one can consider a specimen consisting of only one face sheet and the core material. That enables a better access to the core material not limited to the edges of the plate.

For the wave within the face sheet a delamination between the face sheet and the core material is in a simplified manner comparable to a change in the boundary conditions from an interface to a free surface. For having access to the lower boundary of the face sheet a specimen was produced with a small section without permanently bonded hardfoam (see Fig. 4.9). The missing element was then reversibly coupled to the face sheet with a couplant which enables the stress transfer between face sheet and hardfoam. For simulating a delamination one could remove the hardfoam element, clean both planes from the couplant, and reinsert the element. The lack of couplant sufficiently inhibited the transfer of energy between the face sheet and the core. It is assumed that the adhesive which is used for permanently bonding the

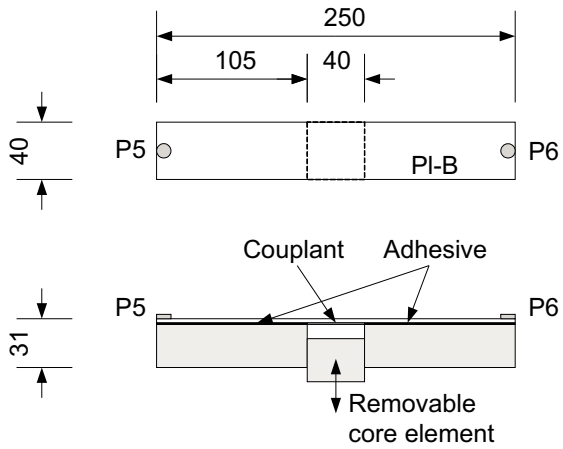

Figure 4.9: Schematic arrangement (dimensions in [mm]) for the detection of reversible delaminations in the aluminum sandwich.

face sheet with the core material transfers both normal and shear stresses. Hence, the couplant has to be incompressible as well as viscous. Measurements with several couplants showed that honey is best suited due to the easy handling, low price and because it can be washed away with water. When applying the couplant one has to make sure that the layer is as thin as possible to minimize its influence, in particular the damping. For smoothing the rough surface of the hardfoam one side of the element which was meant for contacting the face sheet was covered with a thin layer of the same adhesive as used for permanently bonding. During the curing process of the adhesive the element was pressed on a Teflon foil which was lying on a plane. The Teflon allowed for removing the element easily. This procedure resulted in an even and smooth surface on one side of the core element.

Several measurement series with the GW method were carried out in order to investigate the proposed method for producing artificial and reversible delaminations. The results of one series are presented here. The specimen consisted of an aluminum face sheet and a hardfoam core with a thickness of 1 mm and 30 mm, respectively. Piezoceramic disc transducers were used in a pitch-catch configuration. For the measurements, the plate was simply put on a table with the face sheet upwards.

The removable core element (40 mm $\times$ 40 mm) of the specimen (250 mm $\times$ 40 mm, designated as Pl-B) was in the middle of the specimen's length. The transducers (designated as P5 and P6) were positioned at either end of the plate (see also Fig. 4.9). After measurements with and without couplant (honey) the core element was glued permanently into the gap with the same adhesive as used for bonding the other parts of the core. The measurement was repeated before a delamination with the same dimensions as before was mechanically introduced by punching a steel sheet between face sheet and core. A comparison between the time histories measured with the reversibly (with couplant) and permanently (with adhesive) coupled core element and with a reversible (without couplant) and irreversible (mechanically damaged) delamination is given in Fig. 4.10. The transducer P5 was excited with a tone burst (5 cycles with a Hanning window, starting at $t = 50$ μs) at a center

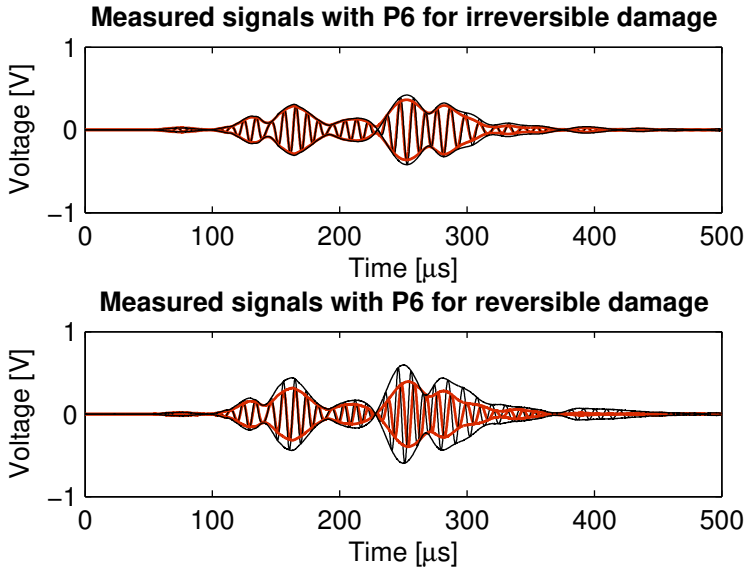

Figure 4.10: Results of the measurements with the disc transducer P6: time histories and envelopes for the undamaged (red) and damaged state (black) for the irreversible case (top) and the reversible case (bottom). The disc transducer P5 was used for excitation (5-cycle tone burst, Hanning window, center frequency of 100 kHz, starting at $t = 50$ μs).

frequency of 100 kHz and a peak-to-peak amplitude of around 200 V while P6 was used as receiver.

It can be seen that the delamination causes an increase of the amplitudes of all present wave modes as it was also obtained in the measurements presented before. However, the differences between the undamaged and damaged state are larger for the reversible delamination than for the irreversible one. The reason for this might be on the one hand the couplant which leads to a higher damping than the permanent bonding layer and on the other hand the free surface of the artificial delamination which represents an idealized debonding with less damping than a more realistic damage. Nevertheless, the changes within the situation with the reversible damage are qualitatively comparable with the other ones.

4.4.4 Conclusion

From the preliminary investigations the following conclusions can be made:

- Within an aluminum sandwich plate (as used for the experiments presented here) the waves propagate mainly in the face sheet where the excitation was applied. The waves behave like Lamb waves. No wave modes through the whole thickness of the sandwich plate exist in the considered frequency range.

- Delaminations between face sheet and core material lead to changes in the measurement signals and thus they are virtually detectable. It was obtained

that the waves which propagate over the delaminated area had higher amplitudes compared to the undamaged case. This effect was more pronounced for higher frequencies and for larger delaminations.

- Delaminations can be artificially produced by reversibly coupling and decoupling the face sheet and the core material with a coupling agent, namely honey.
- The use of MFC leads to changed measured signals in a pitch-catch configuration compared to measurements with piezoceramic transducers, in particular when the fiber directions of the two MFCs are in an oblique angle to each other. The special emitter and receiver characteristics of AFC/MFC can yield more difficult signal interpretation which can be considered as a drawback.

4.5 Final Experiment

The findings of the preliminary investigations had been used for the conception of the final experiment. Within this investigation artificial and reversible delaminations in an aluminum sandwich plate were detected with the help of AFCs which were used as emitter and receiver for both the GW method and the EMI method. For comparison, the same measurements were carried out with piezoceramic disc transducers. The experimental setups and the materials are described in details in Sec. 4.2 and 4.3, respectively, additional informations are given below.

4.5.1 Arrangement and Measurement

The specimen (designated as Pl-C) consisting of one 1 mm thick aluminum face sheet and a 30 mm thick hardfoam core had a length of 500 mm and a width of 250 mm. A rectangular delaminated area (50 mm × 50 mm) was located in the center of each smaller edge of the plate (see Fig. 4.11). Two AFCs (AFC-4 and AFC-5) with an active length l_a of 20 mm and two piezoceramic transducers (designated as P7 and P8) with a diameter of 10 mm were positioned in the corners of the face sheet so that on each side of a delamination the similar transducer type was present. The AFCs were glued with the fiber direction oriented along the width of the plate and as close as possible to the edges of the plate. The removable hardfoam elements with one smoothed surface (see Sec. 4.4.3 for details) was reversibly coupled to the face sheet with honey. For the measurements, the plate was simply put on a table with the face sheet upwards.

For the measurements with the GW method waves were sent from one AFC to the other and vice versa or from one piezoceramic transducer to the other and vice versa. Tone bursts (5 cycles with a Hanning window) at several center frequencies between 40 kHz and 440 kHz were used as excitation signal. The peak-to-peak amplitude of the voltage signals sent to the emitter was around 200 V. For the EMI method an initial measurement between 100 Hz and 500 kHz was carried out to determine the frequency range of interest. The range was then set from 20 kHz to 120 kHz where most peaks in the spectra of the real part of the impedance Z were obtained. The

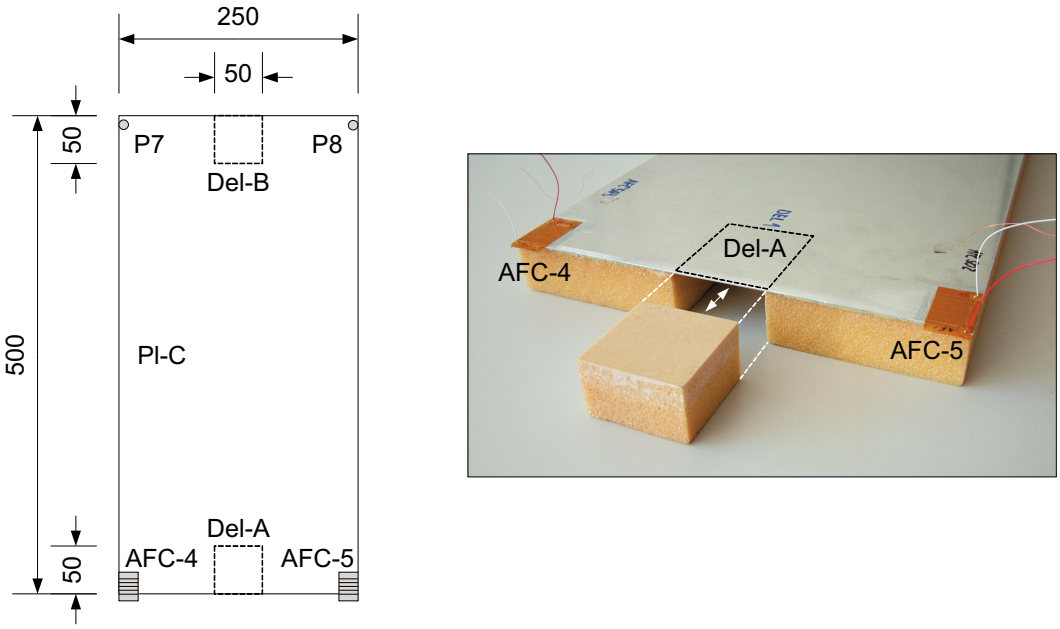

Figure 4.11: Schematic arrangement (dimensions in [mm]) for the delamination detection in the aluminum sandwich plate with AFCs (left) and a picture of the specimen with the removable core element.

impedance was measured at two hundred stepwise increased frequencies within the defined frequency range. This results in a frequency resolution of 500 Hz. During each single measurement at a constant frequency the transducer is harmonically excited with a voltage signal with an amplitude of 2 V.

Several measurements with both the GW method and the EMI method were performed consecutively for changing damage states. Tab. 4.1 gives an overview of the measurements. The artificial delamination corresponds to the case without (wo) couplant while the undamaged state is achieved with (w) the application of the couplant. All damage states were generated and measured at least twice. The data from the measurements with the GW method were also used to estimate the transfer function from transducer to transducer within the frequency range used.

4.5.2 Results and Discussion

GW method

The active length of the AFCs was set to 20 mm which resulted in a maximum in the transfer function for the A_0 mode and a minimum for the S_0 mode at 235 kHz when the AFC is bonded on a 1 mm thick aluminum plate. By looking at the measured transfer functions for the shortened AFC as presented in the previous chapter (see Fig. 3.31 and 3.32 on page 69 and 70, respectively), it can be seen that at a frequency of 280 kHz the transfer function of the A_0 mode has a minimum, while that one of the S_0 mode has non zero amplitudes. Thus, at this frequency a S_0 mode

Symbol	Del-A	Del-B	GW method (pitch-catch)	EMI method
	with/without couplant		Transducer-No.	Transducer-No.
M0	wo	wo	4→5, 5→4, 7→8, 8→7, 4→7, 4→8, 7→4, 7→5	4, 5, 7, 8
M1a	w	wo	4→5, 5→4	4, 5
M1b	wo	w	7→8, 8→7	7, 8
M2	wo	wo	4→5, 5→4, 7→8, 8→7	4, 5, 7, 8
M3a	w	wo	4→5, 5→4, 7→8, 8→7	4, 5, 7, 8
M3b	wo	w	4→5, 5→4, 7→8, 8→7	4, 5, 7, 8
M4	wo	wo	4→5, 5→4, 7→8, 8→7	4, 5, 7, 8

Table 4.1: Overview of measurements performed for the delamination detection with AFCs.

should be excited preferably. The measurement of the overall transfer functions from AFC to AFC for both wave modes confirmed this behavior. However, the optimal frequency for mainly exciting the A_0 mode was found at 220 kHz instead of 235 kHz. This discrepancy of 6.4% might be attributed to slight differences between the wave velocities within the sandwich plate and the aluminum plate. The measured overall transfer functions for both transducer pairs are presented in App. D.3. For the further evaluations, only the data from the measurements at 220 kHz and 280 kHz were considered.

Fig. 4.12 shows the time histories measured with AFC-5, while AFC-4 was excited with a tone burst at a center frequency of 220 kHz and 280 kHz. The signals and their envelopes for both the undamaged (M3a) and damaged (M2) state are given as well as the difference of the two signals. Considering the S_0 mode which arrived at $t = 91$ μs it can be seen that the amplitudes are much smaller for the measurement at 220 kHz than at 280 kHz. However, they could still be measured. The same could be obtained for the A_0 mode (arrival time $t = 141$ μs) at 280 kHz where the transfer function for the A_0 mode had a minimum. The reason for this is the frequency content of the excitation signal (sinusoidal tone burst modulated with a Hanning window). The width of the principal lobe in the frequency domain is $\frac{4}{n}f$ where n is the number of cycles of the modulated sinusoid with the frequency f. Hence, a wave mode is excited even if the center frequency of the excitation signal coincides with a minimum in its transfer function, but the wave form seems to be disturbed. By increasing the number of the cycles of the excitation signal which would lead to a smaller band width, better results would be achieved. However, the duration of the wave modes would increase as well and the two modes would not be separated in the measured time signal anymore.

Although the A_0 mode was excited and measured at a maximum in its transfer function at 220 kHz, the amplitudes were relatively small compared to the S_0 mode. The reasons for this might be on the one hand the damping, which is higher for the A_0 mode than for the S_0 mode [76]. On the other hand, the emitting and

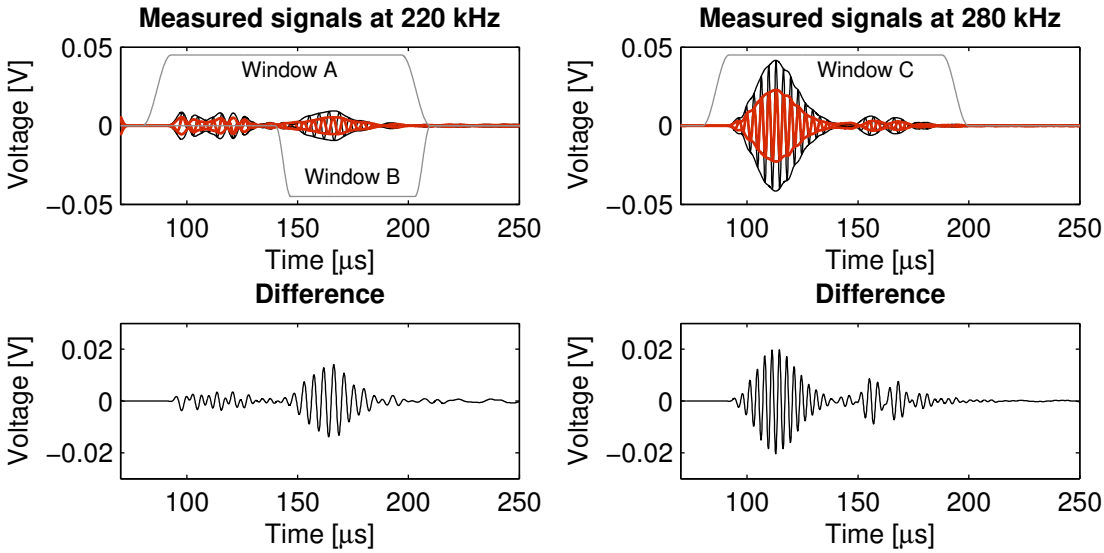

Figure 4.12: Results of the measurements with AFC-5: time histories and envelopes for the undamaged (red) and damaged state (black) and the time window used for calculating the DFTs (top); and the difference of the two time signals (bottom). AFC-4 was used for excitation (5-cycle tone burst, Hanning window, starting at t = 50 μs) at 220 kHz (left diagrams) and 280 kHz (right diagrams).

receiving capabilities are poorer for the A_0 mode in particular when the AFC is used as receiver due to the much smaller wavelength compared to the length of the AFC. At 280 kHz, however, the amplitudes of the preferably excited and measured S_0 mode were much higher than those of the A_0 mode.

It is noticeable that for 280 kHz the S_0 mode wave packet had much more cycles than the excitation signal. This is caused by the superpositions of the four excited S_0 wave packets; on either end of the AFC two packets were excited whereas each of them propagated in the opposite direction. Due to the reflection of the wave packets at the boundary of the plate, which coincides with one end of the AFC, all four packets propagated in the same direction but with a relative time delay. The same could be obtained for the receiver since the incident wave (and after the respective time also its reflection) was measured when it passed the edges of the AFC. For 280 kHz where the wavelength of the S_0 mode is around two third of the length of the AFC, the emitted wave packet theoretically has eight cycles and the measured signal even eleven cycles. It is mentioned that for the arrangement as used here it was necessary to place the AFC next to the plate's edge. Otherwise, the emitted waves can destructively interfere with their reflections.

Considering the time histories and the difference between them for the undamaged and damaged state, one can see that both wave modes were affected by the presence of the delamination and that the amplitudes were increased for the damaged state. This can also be obtained in the DFTs (see Fig. 4.13) of the time histories measured at 220 kHz and 280 kHz for the undamaged (M1a and M3a) and damaged states (M0, M2 and M4). The DFTs were calculated by applying different

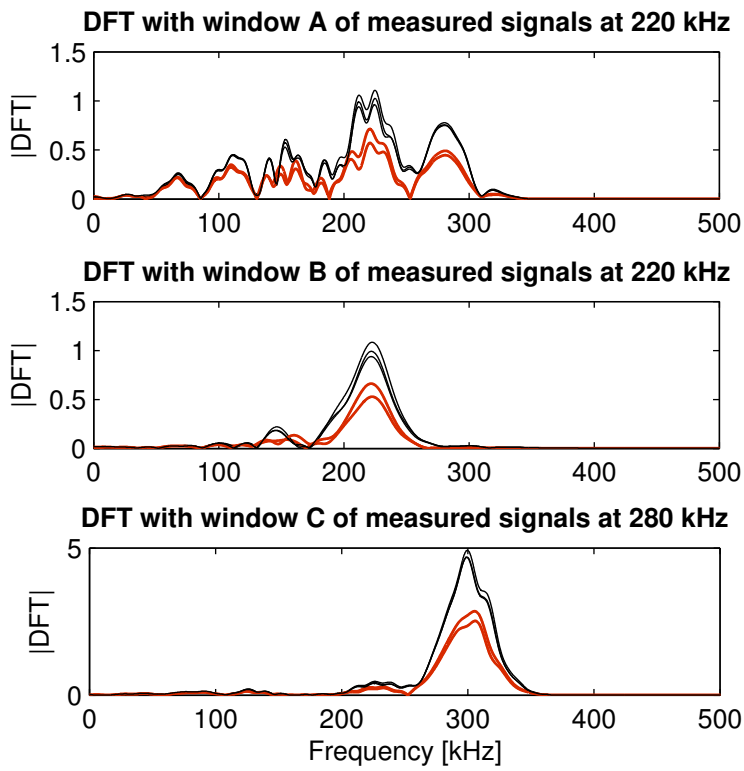

Figure 4.13: Results of repeated measurements with the AFC-5: amplitude spectra of the DFTs for the undamaged (red) and damaged states (black) calculated with different time windows as shown in Fig. 4.12. AFC-4 was used for excitation (5-cycle tone burst, Hanning window) at 220 kHz (upper two diagrams) and 280 kHz (bottom).

time windows. For the DFTs at 220 kHz in the upper diagram both wave modes were taken into acount (time window from 80 μs to 210 μs), for the DFTs in the middle only the A_0 mode was considered (140-210 μs). The DFTs at 280 kHz in the lower diagram includes again both wave modes (80-200 μs). Although the DFTs for the same damage state varies, there is a clear change between the two states in all three diagrams. This indicates that the proposed method for producing artificial delamination allows for switching between the two damage states with reproducible results.

A comparison of the two upper diagrams – one depicts the DFTs including both modes, the other the DFTs including only the A_0 mode – shows the influence of the S_0 mode on the DFT. The two major peaks of the DFTs taken from the A_0 mode are almost within the frequency range of the excitation whose main lobe is between 132 kHz and 308 kHz, and the minima at 170 kHz and 280 kHz correspond to minima in the A_0 transfer function. This is reasonable since the depicted DFT results from the multiplication of the DFT of the excitation with the A_0 transfer functions in the frequency domain of both the emitter as well as the receiver and with a term describing the propagation behavior of the waves [81].

However, there are more peaks within the DFTs taken from both modes. Within the frequency range of the excitation's main lobe a minimum at 250 kHz which corresponds to a minimum in the S_0 transfer function appeared and the minimum at 280 kHz disappeared due to the superposition with the S_0 mode. The minima at 44 kHz and 88 kHz correspond to the side lobes of the DFT of the excitation signal. However, the peaks below 132 kHz are much more pronounced. This can be explained again with the multiplication in the frequency domain of the transfer functions of the involved processes. However, for the emitting and receiving process both the S_0 and the A_0 transfer function has to be taken into account. Since the S_0 transfer function for the emitter has a maximum at 120 kHz and that for the receiver has much larger amplitudes below than above its first minimum at around 235 kHz, waves are emitted and, particularly, also measured at lower frequencies.

The situation for the measurement at 280 kHz (see lower diagram) is similar except that the peak at 300 kHz which corresponds to a maximum in the measured S_0 transfer function is much higher due to the shifted frequency range of the excitation signal (main lobe between 168 kHz and 392 kHz). The influence of the A_0 mode is small since the minima of the A_0 transfer function (90 kHz, 170 kHz and 280 kHz) can not be seen in the depicted DFTs.

Fig. 4.14 shows the results of the similar test series but measured with the piezoceramic transducer P8 while P7 was excited at 280 kHz. The time histories of the undamaged and damaged state (M3b and M2, respectively) and the DFTs taken from both modes (80-210 μs) are depicted for all repeated measurements (M1b, M3b; and M0, M2, M4, respectively). As already could be seen in the preliminary investigations (see Sec. 4.4.2), the S_0 mode is dominant due to the excitation near beside the planar resonance frequency of the disc transducer (around 260 kHz). Thus, the maximum in the DFTs occurs not at the center frequency of the excitation. The smaller peaks result from the overlap of the two wave modes in the time histories. Measurements at frequencies up to 400 kHz showed that the transfer behavior is poor above 300 kHz. Further, there is a relatively large deviation between the two measurements of the undamaged state (M1b and M3b), which might be attributed to variations in the couplant layer. However, the differences between the undamaged and damaged state are still distinctly recognizable.

The comparison with the investigations with the AFC shows that the signals measured with the piezoceramic transducers have amplitudes which are one order of magnitude higher. The reason for this might be the relation between the diameter of the disc transducers to the length of the wave propagating in the plate. For the frequency of 280 kHz, the diameter is around half of the wavelength. Thus, the transfer behavior is almost optimal not only for the emitter – maximum amplitudes in the S_0 transfer function – but also for the receiver – high amplitudes for frequencies below the first minimum.

For the case where the delamination was introduced at the opposite edge regarding to the used transducer pair (measurement M3b for the AFC and M3a for the disc transducer, not shown), changes which could be clearly assigned to the introduced damage were obtained only for frequencies around 100 kHz and only within the

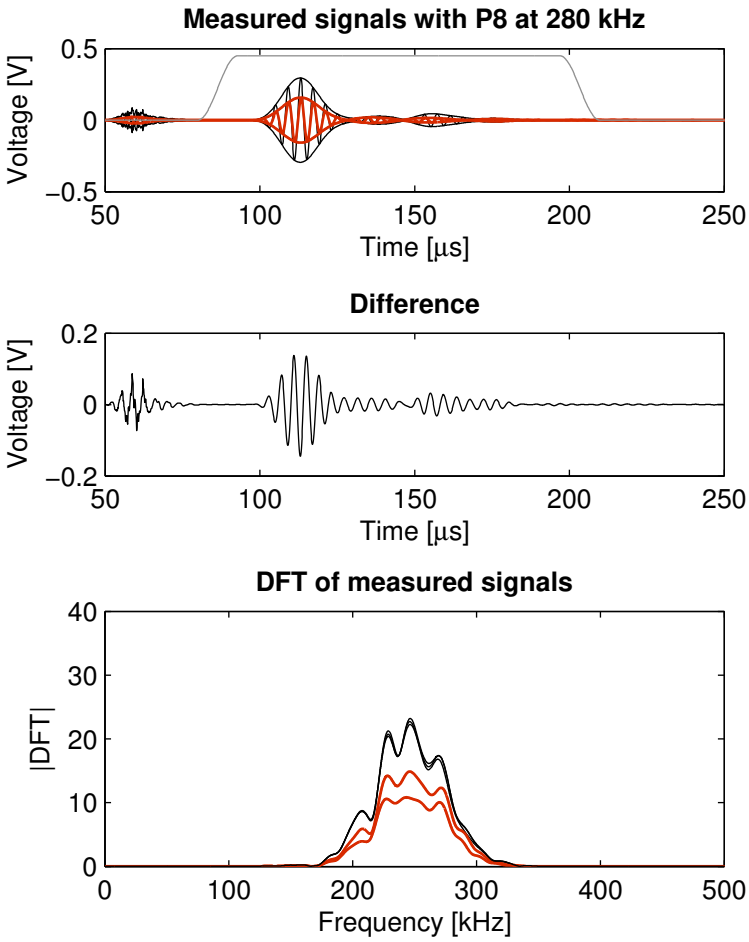

Figure 4.14: Results of the measurements with the disc transducer P8: time histories and envelopes for the undamaged (red) and damaged state (black) and the time window used for calculating the DFTs (top); the difference of the two time signals (middle); and the amplitude spectra of the DFTs for repeated measurements (bottom). Transducer P7 was used for excitation (5-cycle tone burst, Hanning window, center frequency of 280 kHz, starting at $t = 50$ μs).

measurements with the disc transducers. The first can be explained by the damping which increases with increasing frequency. Hence, the reflections from the opposite edge could not be measured anymore at higher frequencies. The second is due to the directionally dependent behavior of the AFC which prevent it from emitting waves toward and receiving waves from the damaged area.

EMI method

The electro-mechanical impedance was measured with all four transducers, however, the results of AFC-4 and of piezoceramic transducer P7 only are presented since the results from the other elements are almost equal. Fig. 4.15 depicts the real part of the impedance for both transducer types and for two different damage states (M2 and M3a for the AFC and M3b for the piezoceramic transducer) as well as the difference of the real parts between the two damage states, which emphasize the changes due to the delamination. The general form of the curve differs for the two transducer types. This is reasonable since the curve is defined by several factors, e.g., the capacitance or the dynamics of the transducer which are both also defined by its design and dimensions. However, more interesting are the small peaks which occur due to resonances within the system consisting of both the plate and the surface bonded transducer. These peaks are more pronounced for the AFC than for the disc transducer and occur in a different frequency range (between 45 kHz and 75 kHz for the AFC and between 30 kHz and 60 kHz for the disc transducer). The reason for this might be the differences in the transfer behavior which lead to the excitation of different vibration modes depending on the used transducer type.

Comparing the impedance spectra for the two damage states, it can easily be seen that the peaks within the mentioned frequency range were affected by the damage, namely, the peaks became more pronounced with the introduction of the delamination. This is reasonable since the damping of the sandwich plate decreases when a delamination is present. This is also confirmed by the findings of the investigations with the GW method where the amplitudes of the propagating waves were increased as well compared to the undamaged state. The changes due to the delamination were larger for the AFC than for the disc transducer as it is shown in the lower diagram. Further, the shift between the two measured impedance spectra for the AFC (see upper diagram) results in a deviation from zero in the curve of the difference over the whole frequency range. The shift which was also observed within other measurements might be caused by the measurement system itself, by variations in the connection between measurement system and transducer, or by even small shifts in the room temperature. Nevertheless, the changes in the small peaks due to the damage can clearly be seen. Since the peaks and changes of them could be captured in the measurements, the frequency resolution of 500 Hz was sufficiently accurate. No well marked changes were obtained for both transducer types when the damage was introduced at the opposite edge of the plate. The reason for this might be the small amplitudes of the excitation of only 2 V in combination with the damping, which prevent the plate from vibrating in appropriate modes.

Except for the mentioned shifts the measured spectra were well reproduced when

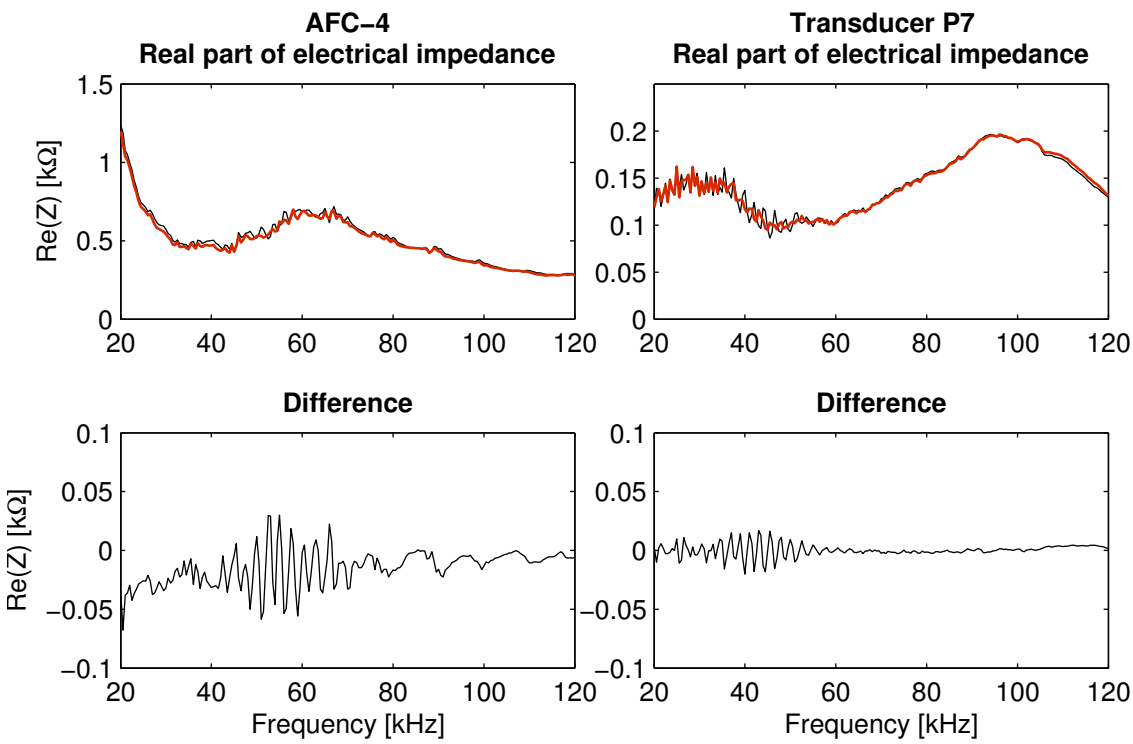

Figure 4.15: Results of the measurements with the AFC-4 (left diagrams) and the disc transducer P7 (right diagrams) from 20 kHz to 120 kHz with a frequency resolution of 500 Hz: Spectra of the real part of the electrical impedance (top) for the undamaged (red) and damaged state (black) and the difference of the two spectra (bottom).

switching between the two damage states. Moreover, the measurements with the same transducer types showed the same behavior with peaks at the same frequencies, which also confirmed that all transducers were well bonded to the plate. Consequently, the obtained changes in the impedance spectra can clearly be attributed to the presence of the delamination.

4.6 Summary

The wave propagation in an aluminum-hardfoam sandwich plate and the influence of a delamination between face sheet and core on the waves was investigated first. It turned out that in the considered frequency range ($\lambda_{core} \ll d_{core}$) the waves propagate mainly within the face sheet and only little energy is transmitted through the core. Further, a delamination leads to increasing amplitudes of the waves which propagate over the delaminated area compared to the undamaged case. A method was proposed which allows for producing artificial and reversible delaminations and hence for switching between undamaged and damaged states with reproducible results. Finally, AFCs were successfully applied for detecting artificial delaminations with two different methods, the GW method and the EMI method.

Chapter 5

Conclusions and Outlook

5.1 Characterization of AFC

The dynamic behavior of an AFC which is surface bonded to an isotropic plate was investigated and transfer functions for both the AFC as emitter and as receiver of elastic waves propagating in the plate were determined. A numerical model was developed which describes the electro-mechanical behavior and the transducer-structure interaction and, hence, which allows for simulating both processes, emitting and receiving propagating waves. The time dependent 3D displacement field around an AFC used as emitter can be calculated with the proposed simulation procedure. The results of the experimental investigations show good agreement with the simulations not only qualitatively but also quantitatively. The behavior of AFCs with two different lengths was accurately predicted by the model from about 60 kHz to 450 kHz for the S_0 mode and from 30 kHz to 300 kHz for the A_0 mode which corresponds to a transducer's length to wavelength ratio of 0.5 to 3 and of 1.5 to 5, respectively.

The proposed model is suitable for the investigation of the coupled dynamic behavior of AFCs and hence can be used for dimensioning elements with specific transfer characteristics. However, to obtain accurate results within the simulation the material parameters of the AFC must be known, in particular, the elastic modulus E_{33} and the piezoelectric constant d_{33}, both for the fiber direction, since their influence on the simulated results is significant. Further, the length of the AFC within the simulation has to be chosen between the active and the total length of the AFC in order to account for the stress distribution between AFC and structure.

As known from literature the shear stresses between transducer and structure during excitation are concentrated at the edges of the transducer. Due to the anisotropic material properties of the AFC waves are mainly excited at the two ends of the fibers. This is comparable with the receiver which detects the waves only when they pass one of these two edges. This leads to unwanted effects if the wavelength is much smaller than the length of the AFC and if only short wave packets are considered, namely the excitation and detection of two wave packets instead of one. In order to avoid this effect, the AFC should be as small as possible

compared to the wavelengths, in particular when it is used as sensor. However, the smaller the AFC, the smaller its capacitance and hence the more attention must be paid to appropriate measurement technique. A charge amplifier may then be better suited than an oscilloscope.

The radiation of waves with an AFC and its sensitivity to incoming waves are highly frequency and directionally dependent. Both, emitting and receiving capabilities are enhanced in the fiber direction of the AFC. On the one hand, the anisotropic material properties of the AFC lead to shear stresses between the electrically excited AFC and the structure which are oriented in fiber direction as well as to a sensitivity particularly for strains in fiber direction – the transverse piezoelectric effect is small and, as seen in the experiments, negligible above 100 kHz. On the other hand, the length and width of the AFC in relation to the length of the wave which propagates in the plate are responsible for the frequency dependence (e.g., the occurrence of minima and maxima in the transfer function) and the directionality. This shows that the dynamic behavior of the permanently bonded AFC is dominated by the dynamics of the structure and, hence, always both components must be considered for determining the transfer characteristic of the transducer. Due to the relation to the wavelength, the transfer behavior differs for each wave mode making it even more complex. Moreover, the anisotropy of the AFC leads to the excitation not only of Lamb wave modes but also of SH modes within the plate. According to the principle of reciprocity [38], it must hence be assumed that the AFC as receiver is also sensitive for these wave modes.

The complexity of the wave field when AFCs are used for excitation restricts the range of applications and must be taken into account already during designing a SHM system with AFCs. Particularly, the use of AFCs in a transducer network in order to monitor large areas can be problematic since there might be sectors which are out of the sensitivity range of the monitoring system. Nevertheless, the directionality, i.e. the radiation of the energy in mainly one direction, can also have a favorable effect on the performance of a system in specific applications, e.g., if AFC are used in combination with anisotropic structures, if single critical points whose positions are known should be monitored, or if unwanted reflections or noise signals from uninteresting directions must be avoided.

5.2 Application of AFC

AFCs were successfully applied for damage detection (first step of the damage identification process in SHM) in an aluminum sandwich plate with the guided wave based method as well as with the electro-mechanical impedance method. The AFC was used as emitter and receiver of elastic waves and as transducer for exciting and simultaneously measuring vibrations. The findings of the characterization were used for dimensioning and positioning the transducer elements.

As stated before, the coupled AFC-structure transfer behavior is most important and must be known to obtain useful and interpretable results. The strong coupling leads to a virtually non-resonant behavior of the surface bonded AFC. However,

there are several frequencies with maximum transduction. Therefore, the AFC can be used in different frequency ranges and is hence interesting as transducer element for different methods and combinations of them. The strong coupling and the dominant dynamics of the structure are advantageous for the use of AFC with the EMI method. Furthermore, the thin planar size as well as the conformability to even biaxially curved surfaces – and therefore its better robustness to brittle failures compared to a piezoceramic transducer – make the AFC suitable particularly for SHM applications.

The investigation presented here showed that once the optimal length of the AFC has been determined with the help of the model, an AFC with standard design can be shortened by simply cutting it to the required length. For the final experiment with the GW method, the length was chosen so that at one frequency the A_0 mode and at another one the S_0 mode was excited preferably. However, it was not possible to excite only a single wave mode, i.e. to achieve a perfect mode selection. The reason for this is the time limited excitation signal whose frequency content is within a certain frequency range and not equal to one single frequency. Nevertheless, it is possible to control the ratio between the amplitudes of the two excited Lamb wave modes. In contrast to this, the EMI method works with harmonic excitations or in other words, the excitation contains one single frequency. Theoretically, if an eigenfrequency of the structure coincides with a minimum in the transfer function of the AFC, the corresponding eigenmode will not become developed and hence no peak will be present in the impedance spectrum.

The wave propagation in an aluminum sandwich plate and the interaction of the waves with face sheet-core delaminations was investigated. With the experimental setup used here virtually no scattering effects due to the delamination were obtained. This seems reasonable since the the main wave guide – the aluminum plate – is not damaged itself. The lack of scattered waves may complicate a localization of the damage (second step of the damage identification process in SHM), particularly, with the triangulation method which is based on an arrival time lag between the wave propagating on the direct path between emitter and receiver and the scattered wave from the damage.

The aluminum sandwich plate as used in this work is well suited for being monitored with wave based methods since the waves can travel long distances and the propagation is well defined. It would be worthwhile to investigate plates made of anisotropic composite face sheets or of honeycomb cores since such plates have a wider range of applications. However, the wave propagation characteristic would be much more complex which complicates the monitoring process.

Both methods used for damage detection are based on a comparison of an actual measurement with a reference measurement and a difference is then attributed to a damage of the structure. However, there might be other reasons for changes within the measured signals than a structural damage. Environmental exposure, e.g., temperature variations, can cause changes in the wave propagation characteristics. Moreover, a failure or a debonding of the transducers themselves will yield differences between actual and baseline measurement. For a reliable damage detec-

tion system, it is important to investigate such aspects. The use of the methods without baseline is only possible, if the variations caused by the application of various AFCs and by the bonding layer are smaller than those caused by a damage or if they can clearly be distinguished from the others. However, a large amount of transducers is needed to be tested in advance in order to get the required statistical informations.

5.3 Outlook

In the following, some aspects and ideas for future work are listed which may be important to make a further step toward a SHM system with AFC as transducer elements.

- In order to use the numerical model for a wider range of different structures, two modifications are proposed. First, absorbing boundary conditions should be implemented which allows for reducing the structure's dimensions within the model and hence the computational time without the difficulties of reflected waves. Second, the isotropic properties of the structure can be replaced by anisotropic properties. This would allow for simulating the wave propagation in structures made of composite materials such as glass or carbon fiber reinforced plastics which are of particular interest for SHM applications.

- The AFC with its IDE seems to be ideal for a partition of the active area in two sections with different lengths (see [70]) by simply dividing the outer part of the IDE at the required position and electrically isolating the two parts from each other. One section of the AFC can be tuned for optimal excitation and the other – smaller one – can be used as sensor. This concept would have the advantage that the electrode used for relatively high voltage excitation is not connected with the sensitive electronic parts used for measuring. Further, emitter and receiver can be optimized separately which enhance the overall transfer behavior from one AFC to another. This is useful in an application where each element is used as both emitter and receiver. If one section is not used as sensor, it can be used as emitter with different transfer characteristics than the other part.

- Moreover, in order to enhance the modal selectivity achieved with the AFC, it may be worthwhile to tune the dimensions of the IDE to the length of the propagating wave such as it is done for conventional surface acoustic wave transducers (e.g., [50], [66]). However, it would not be possible anymore to perform the polarization process with the aid of the IDE since a uniform instead of an alternating polarization is required.

- A possibility to profit from the directionally dependent behavior of the AFC would be a combination of an AFC with a piezoceramic disc transducer whose sensitivity is rotation-symmetric. If both transducers measure the same incident wave, additional informations about the direction of the wave can be

extracted from the difference between the amplitudes of the two signals. The application of several elements would enhance the probability of correct localization of, e.g., an impact or other acoustic emission sources. For monitoring large areas, the number of required sensors could theoretically be reduced.

- The presented procedure used for the characterization of the AFC as emitter or receiver is applicable to other piezoelectric transducers. This would allow for quantitatively comparing the different elements in their fundamental function over a wide frequency range. The results would be helpful for the selection of appropriate transducers for specific applications.

- Although the use of the SH mode is of less interest for damage detection, the sensitivity of the AFC to these wave modes should be investigated next because SH modes are present in the wave field when an AFC is used as emitter and they could be generated due to mode conversion even if no SH modes were excited.

- Since AFCs are relatively new and suitable for SHM systems, the investigation of their long-term reliability under realistic environmental conditions is of great importance. Furthermore, the use of the EMI method for monitoring the transducer itself and its bonding to the structure should be investigated. This includes to determine the effects on the impedance spectrum caused by fractures of the piezoceramic fibers, failures of the AFC or parts of it, or partial debonding of the transducer.

- The wave-damage interaction would be worthwhile to investigate in detail in order to find appropriate approaches for locating and evaluating (second and third step of the damage identification process, respectively) delaminations in a sandwich plate or any defects in other structures with the GW method.

- Beside all mentioned aspects concerning wave propagation phenomena and the AFC itself, it is also important to give attention to the signal processing if the next steps of the damage identification process should be reached.

Appendix A

Material Parameters

For all simulations presented in this work, the following material parameters were used.

AFC			
Stiffness at constant electric field	c_{11}	[GPa]	10.65
	c_{12}	[GPa]	4.352
	c_{13}	[GPa]	4.816
	c_{33}	[GPa]	24.09
	c_{44}	[GPa]	3.100
Piezoelectric constants	e_{31}	[C/m^2]	-0.764
	e_{33}	[C/m^2]	7.363
	e_{15}	[C/m^2]	1.457
Relative dielectric constants	ε_{11}	[-]	833
	ε_{33}	[-]	755
Density	ρ	[kg/m^3]	4700

Table A.1: Material parameters for an AFC as used for the simulation. The parameters were derived from those presented in Tab. 2.1.

Aluminum			
Elastic modulus	E	[GPa]	68.9
Poisson's ratio	ν	[-]	0.33
Density	ρ	[kg/m^3]	2700

Table A.2: Material parameters for aluminum.

Core material			
Elastic modulus	E	[MPa]	69
Poisson's ratio	ν	[-]	0.4
Density	ρ	[kg/m^3]	60

Table A.3: Material parameters according to the manufacturer's data sheet for the core material (C70.55 from Alcan Airex AG, Sins, Switzerland) as used for the sandwich plates.

Appendix B

Overview of Performed Investigations

		Plate			AFC					
	Symbol	l_P	w_P	d_P	l_a	w_a	d_{AFC}	l_{tot}	w_{tot}	No.
2D model										
Emitter	**2DE1**	1500	-	1	31	-	0.3	31	-	-
	2DE2	1500	-	1	21	-	0.3	21	-	-
Receiver	**2DR1**	700	-	1	31	-	0.3	31	-	-
3D model										
Emitter	**3DE1**	500	300	1	31	20	-	-	-	-
	3DE2	500	300	1	21	20	-	-	-	-
	3DE3	500	300	1	31	10	-	-	-	-
Receiver	-	-	-	-	-	-	-	-	-	-
Experiment										
Emitter	**ExpE1**	1500	1500	1	31	20	0.3	34	40	1, 2
	ExpE2	1500	1500	1	20	20	0.3	23	40	3
Receiver	**ExpR1**	1500	1500	1	31	20	0.3	34	40	2

Table B.1: Overview of geometric dimensions (in [mm], without symmetries) of the system consisting of the AFC and the plate.

	Simulation	Experiment
Emitter: positions of measurement (r, φ ($\Delta\varphi$)) ([mm],[°])		
S_0	(200, 0°)	(200, 0°)
	(100, 0°-75° (15°))	(400, 0-60° (15°))
A_0	(200, 0°)	(200, 0°-30°)
	(200, 0°-30° (5°))	(400, 0-30° (5°))
Receiver: positions of excitation (r, φ ($\Delta\varphi$)) ([mm],[°])		
S_0	(200, 0°)	(200, 0°-45° (15°))
A_0	(200, 0°)	(200, 0°-45° (15°))

Table B.2: Overview of positions of measurement and excitation for the determination of the transfer function of the AFC as emitter and receiver.

Signal type	Frequency [kHz]	Cycles [-]	Duration [μs]	Amplitude [V]	Range for TF [kHz]
Simulation Emitter					
Sinus (tone burst)	50	3.5	-	-	30-70
Sinus (tone burst)	100	3.5	-	-	60-140
Sinus (tone burst)	200	3.5	-	-	120-280
Sinus (tone burst)	400	3.5	-	-	250-550
Linear sweep	5-250	-	150	-	20-230
Linear sweep	200-450	-	60	-	220-430
Linear sweep	400-650	-	50	-	420-630
Simulation Receiver					
Sinus (tone burst)	50	5	-	-	32-65
Sinus (tone burst)	100	5	-	-	65-130
Sinus (tone burst)	200	5	-	-	130-270
Sinus (tone burst)	400	5	-	-	270-530
Experiment Emitter					
Linear sweep	5-200	-	150	1.5	$\hat{\gamma} \geq 0.95$
Linear sweep	150-250	-	100	1.5	$\hat{\gamma} \geq 0.95$
Linear sweep	200-300	-	100	1	$\hat{\gamma} \geq 0.95$
Linear sweep	250-350	-	80	1	$\hat{\gamma} \geq 0.95$
Linear sweep	300-400	-	80	1	$\hat{\gamma} \geq 0.95$
Linear sweep	350-450	-	60	0.8	$\hat{\gamma} \geq 0.95$*
Linear sweep	400-500	-	60	0.8	$\hat{\gamma} \geq 0.95$*
Linear sweep	450-550	-	60	0.8	$\hat{\gamma} \geq 0.95$*
Linear sweep	500-600	-	60	0.5	$\hat{\gamma} \geq 0.95$*
Linear sweep	550-650	-	50	0.5	$\hat{\gamma} \geq 0.95$*
Linear sweep	600-700	-	50	0.5	$\hat{\gamma} \geq 0.95$*
Linear sweep	650-750	-	50	0.4	$\hat{\gamma} \geq 0.95$*
Linear sweep	700-800	-	50	0.4	$\hat{\gamma} \geq 0.95$*
Linear sweep	750-850	-	50	0.4	$\hat{\gamma} \geq 0.95$*
Sinus (tone burst)	various	5	-		-
Experiment Receiver					
Sinus (tone burst)	40	5	-	2	30-50
Sinus (tone burst)	60	5	-	2	50-70
...	...	...	...	...	...
Sinus (tone burst)	440	5	-	2	430-450

Table B.3: Overview of excitation signals used for the determination of the transfer functions.
*Due to poor signal-to-noise ratio for a few measurements, the frequency ranges were extended to the range where the coherence was higher than 0.8 (see Fig. C.2).

Appendix C

Additional Figures from the Characterization

C.1 AFC as emitter

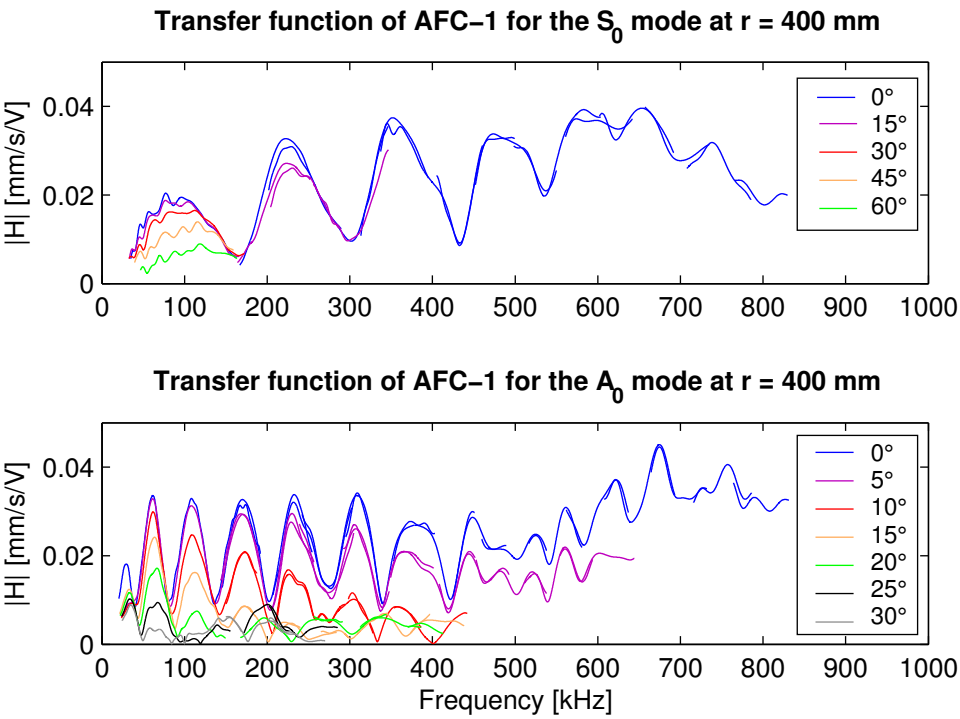

Figure C.1: Measured transfer functions of AFC-1 ($l_a = 31$ mm) used as emitter for the S_0 mode (top) and the A_0 mode (bottom). The surface velocities were measured at $(r, \varphi) = (400, 0°\text{-}60°)$ and $(r, \varphi) = (400, 0°\text{-}30°)$, respectively.

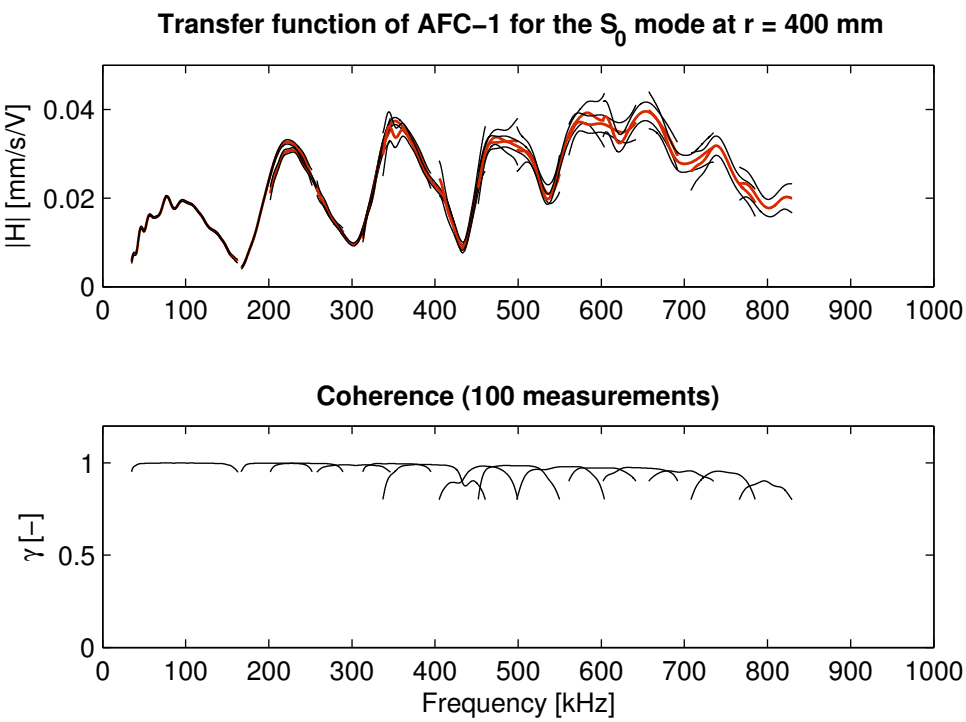

Figure C.2: Measured S_0 transfer function of AFC-1 used as emitter (top, red) with the estimated confidence interval $\hat{s}$ for $\alpha = 99\%$ (top, black) and the estimated coherence function $\hat{\gamma}$ (bottom) for hundred repeated measurements. The surface velocities were measured at $(r, \varphi) = (400, 0°)$. Due to poor signal-to-noise ratio, the frequency ranges for some particular transfer functions were extended to the range where the coherence was higher than 0.8 instead of 0.95.

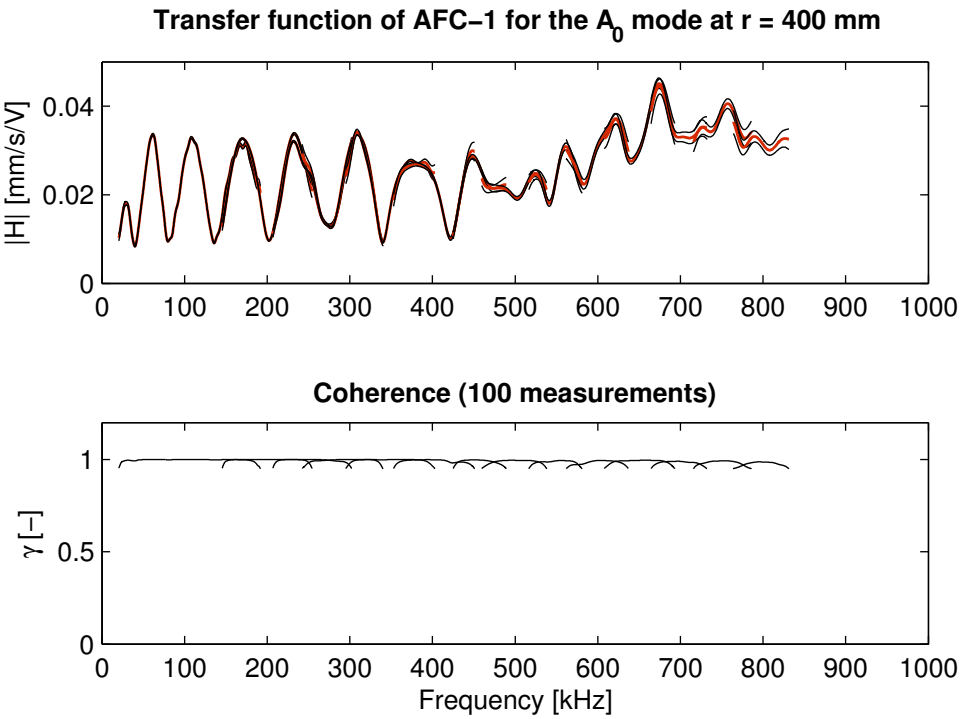

Figure C.3: Measured A_0 transfer function of AFC-1 used as emitter (top, red) with the estimated confidence interval $\hat{s}$ for $\alpha = 99\%$ (top, black) and the estimated coherence function $\hat{\gamma}$ (bottom) for hundred repeated measurements. The surface velocities were measured at $(r, \varphi) = (400, 0°)$.

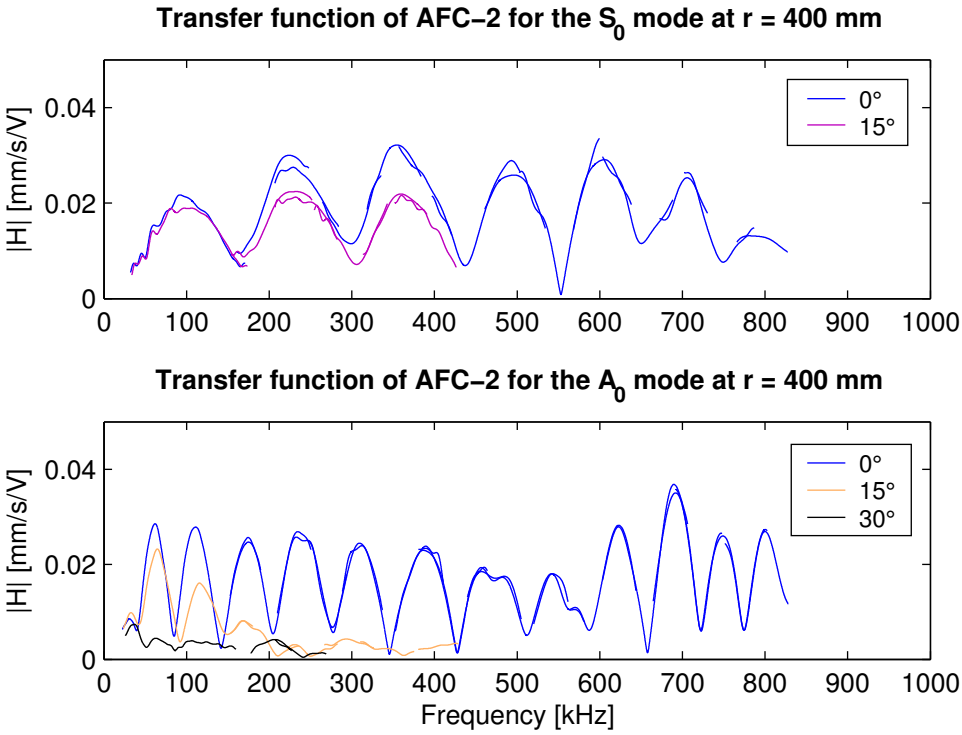

Figure C.4: Measured transfer functions of AFC-2 ($l_a = 31$ mm) used as emitter for the S_0 mode (top) and the A_0 mode (bottom). The surface velocities were measured at $(r, \varphi) = (400, 0°\text{-}15°)$ and $(r, \varphi) = (400, 0°\text{-}30°)$, respectively.

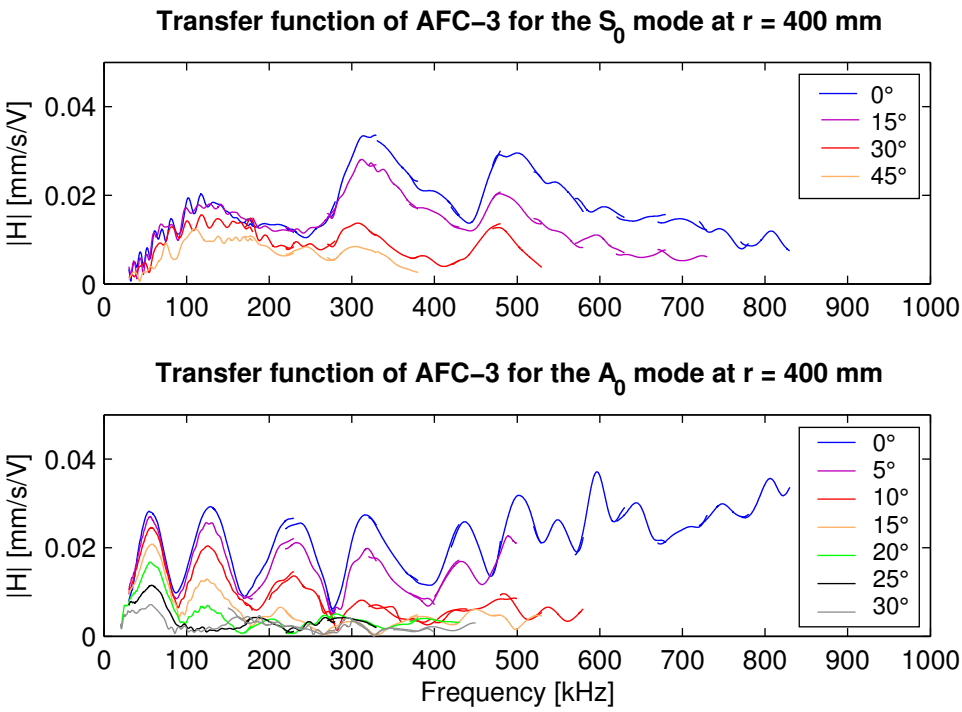

Figure C.5: Measured transfer functions of the shortened AFC-3 ($l_a = 20$ mm) used as emitter for the S_0 mode (top) and the A_0 mode (bottom). The surface velocities were measured at $(r, \varphi) = (400, 0°\text{-}60°)$ and $(r, \varphi) = (400, 0°\text{-}30°)$, respectively.

C.2 AFC as receiver

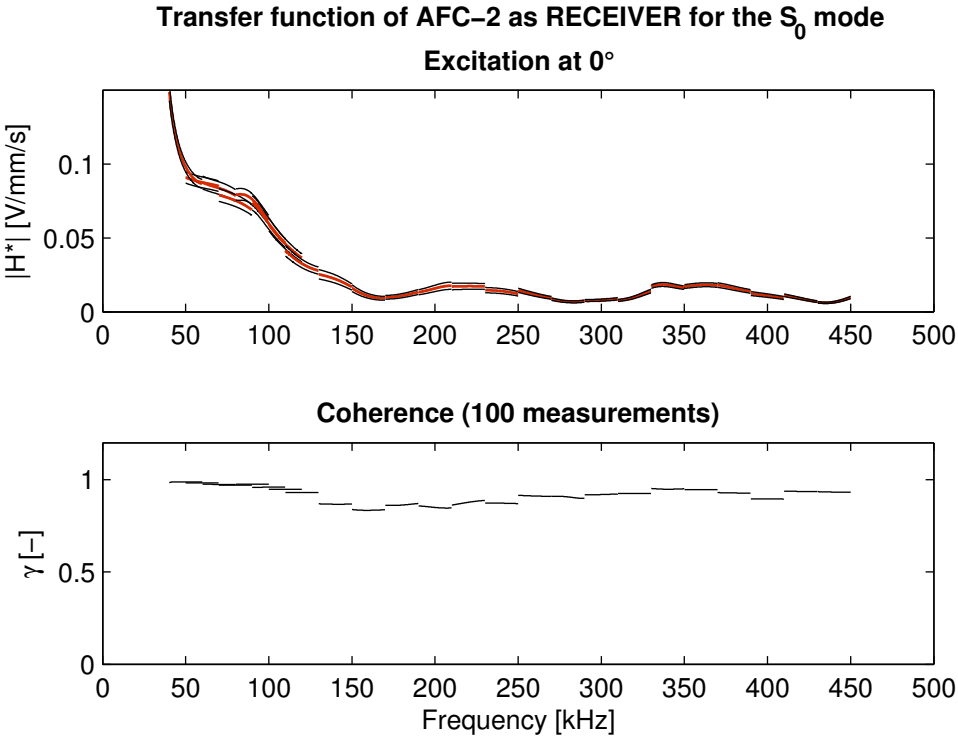

Figure C.6: Measured S_0 transfer function of AFC-1 used as receiver (top, red) with the estimated confidence interval $\hat{s}$ for $\alpha = 99\%$ (top, black) and the estimated coherence function $\hat{\gamma}$ (bottom) for hundred repeated measurements. The excitation was achieved with the piezoceramic transducer positioned at $(r, \varphi) = (200, 0°)$.

Appendix D

Additional Figures from the Application

D.1 Transfer Function of an MFC

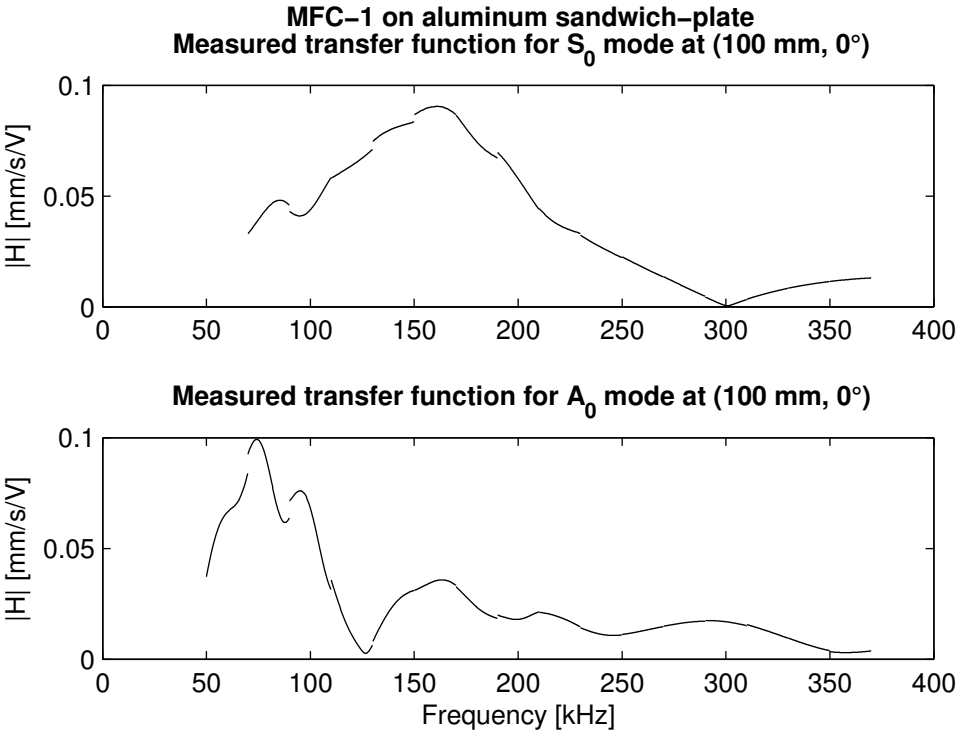

Figure D.1: Measured transfer functions of MFC-1 (l_a = 16.5 mm) used as emitter for the S_0 mode (top) and A_0 mode (bottom). The surface velocities were measured at $(r, \varphi) = (100, 0°)$. The procedure to determine the transfer function was similar to the one presented in Chap. 3.

D.2 Time signals excited and measured with MFCs and disc transducers

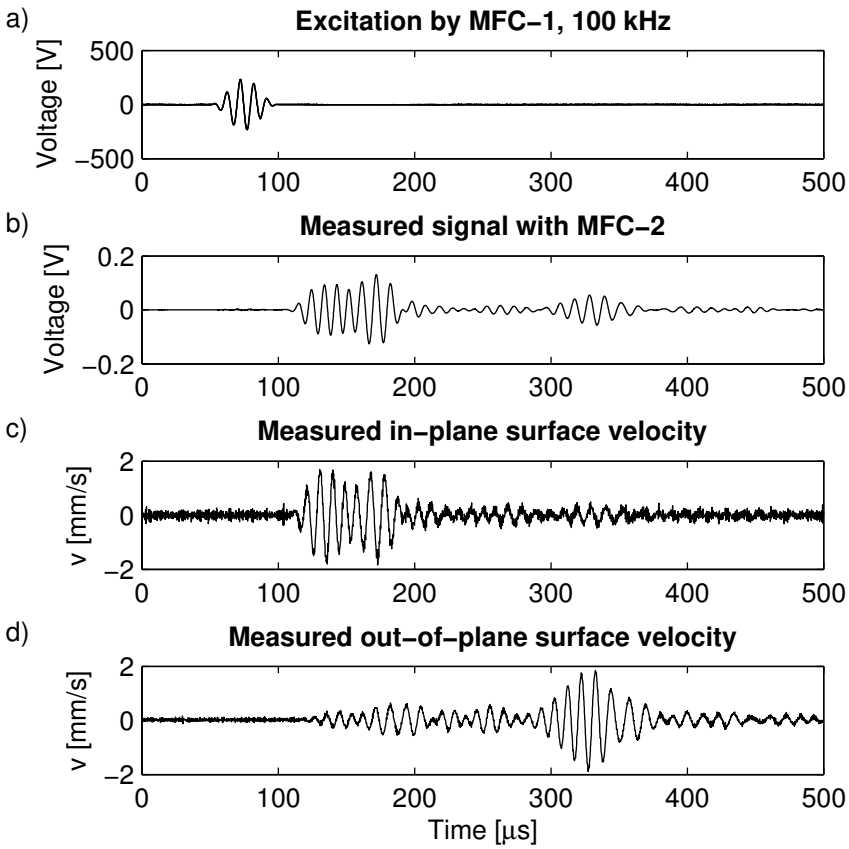

Figure D.2: a) Time histories of the voltage signal used for exciting (5-cycle tone burst, Hanning window, center frequency of 100 kHz) the MFC-1 (top); b) voltage signal measured with MFC-2; c) IP and d) OoP surface velocities measured with the laser interferometer at the position of MFC-2.

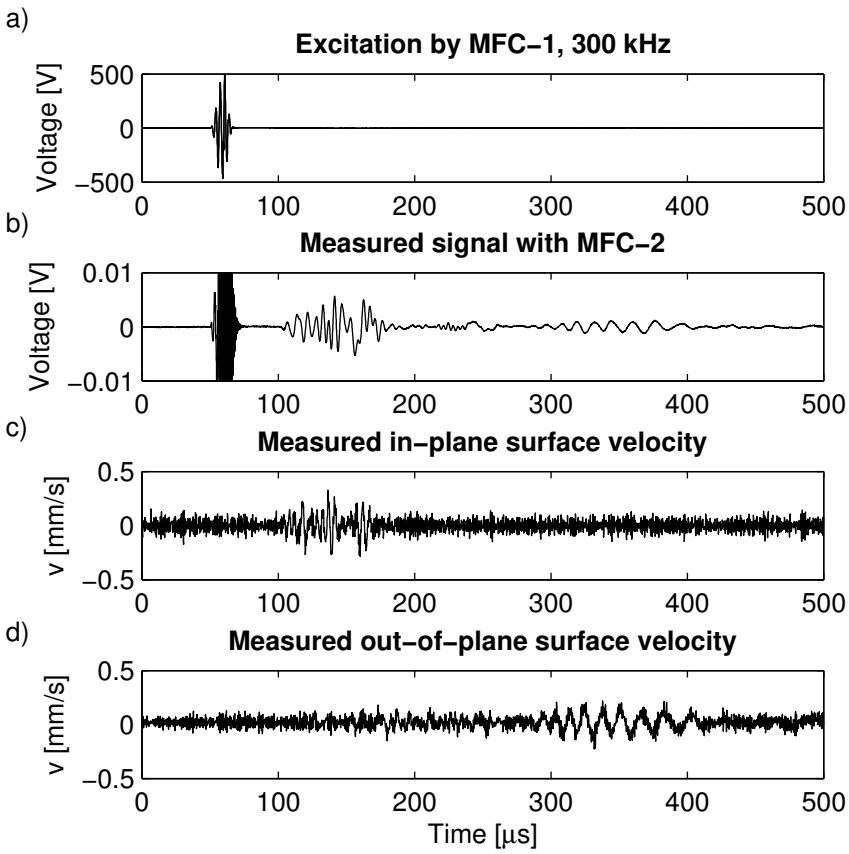

Figure D.3: a) Time histories of the voltage signal used for exciting (5-cycle tone burst, Hanning window, center frequency of 300 kHz) the disc transducer MFC-1 (top); b) voltage signal measured with MFC-2; c) IP and d) OoP surface velocities measured with the laser interferometer at the position of MFC-2.

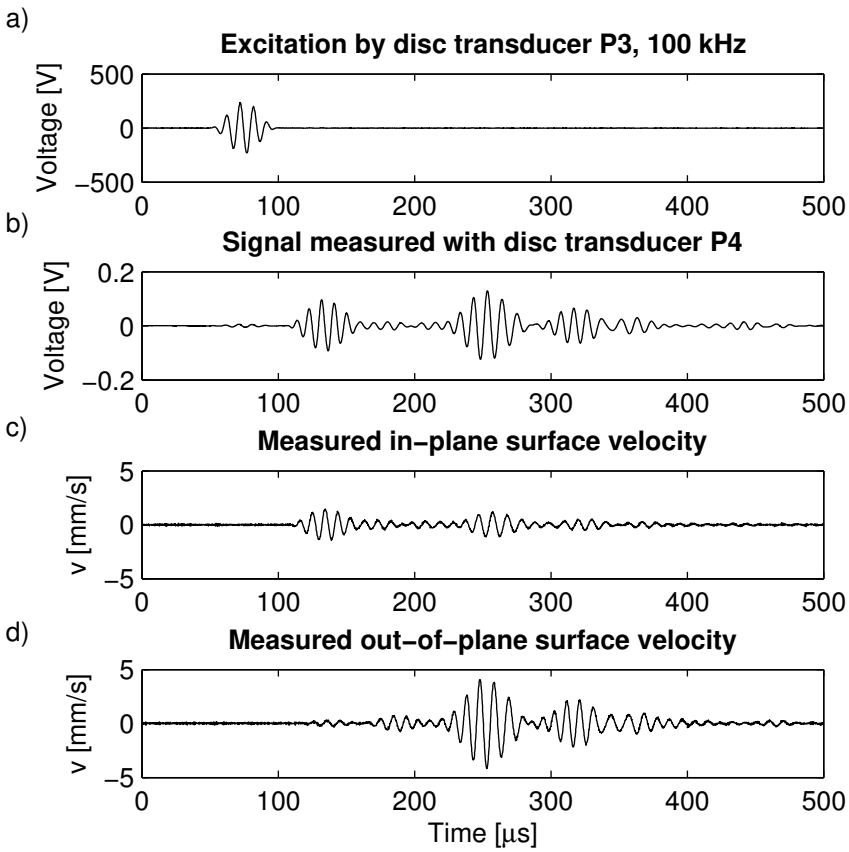

Figure D.4: a) Time histories of the voltage signal used for exciting (5-cycle tone burst, Hanning window, center frequency of 100 kHz) the disc transducer P3 (top); b) voltage signal measured with P4; c) IP and d) OoP surface velocities measured with the laser interferometer at the position of P4.

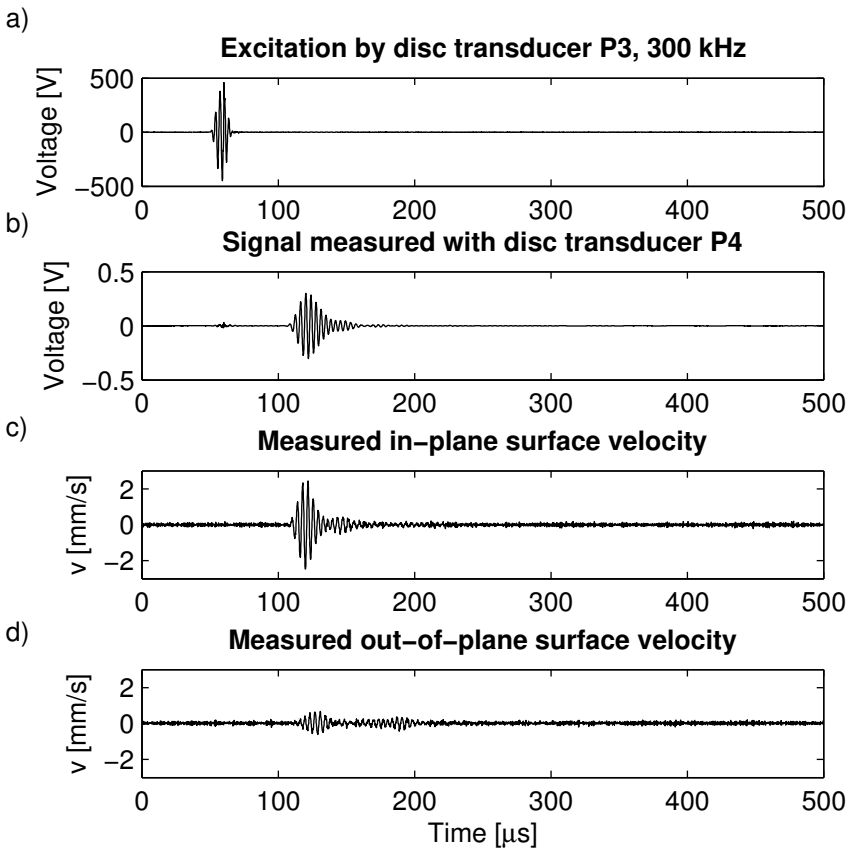

Figure D.5: a) Time histories of the voltage signal used for exciting (5-cycle tone burst, Hanning window, center frequency of 100 kHz) the disc transducer P3 (top); b) voltage signal measured with P4; c) IP and d) OoP surface velocities measured with the laser interferometer at the position of P4.

D.3 Transfer functions from transducer to transducer

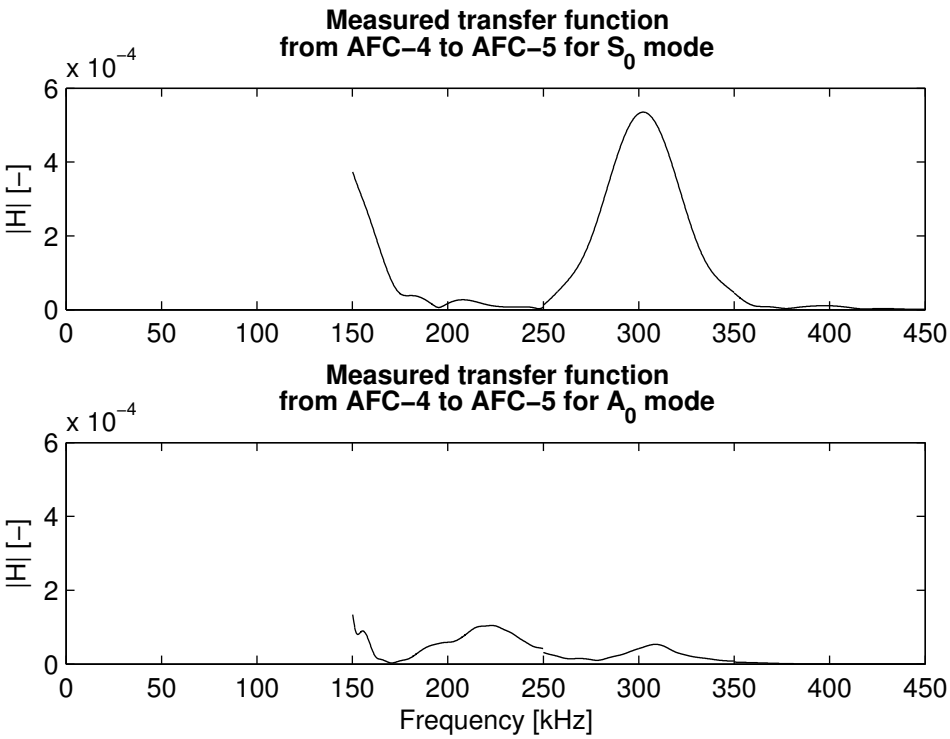

Figure D.6: Measured transfer functions from the AFC-4 to the AFC-5 ($l_a = 20$ mm for both) for the S_0 mode (top) and A_0 mode (bottom).

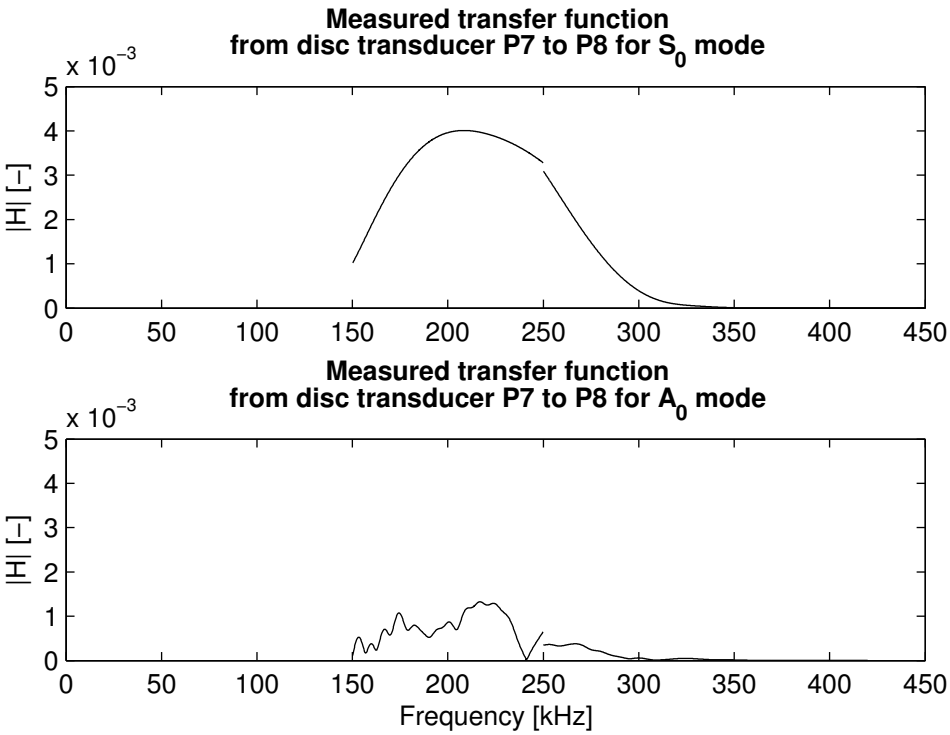

Figure D.7: Measured transfer functions from the disc transducer P7 to P8 (diameter of 10 mm for both) for the S_0 mode (top) and A_0 mode (bottom).

Bibliography

[1] Achenbach, J. D. *Wave propagation in elastic solids*, vol. 16 of *North-Holland Series in Applied Mathematics and Mechanics*. North-Holland publishing company, Amsterdam, 1973.

[2] Alleyne, D. N., and Cawley, P. The interaction of Lamb waves with defects. *IEEE Transactions on Ultrasonics Ferroelectrics and Frequency Control 39*, 3 (1992), 381–397.

[3] Auld, B. A. *Acoustic fields and waves in solids*, vol. 1 and 2. Wiley, New York, 1990.

[4] Balageas, D., Bourasseau, S., Dupont, M., Bocherens, E., Dewynter Marty, V., and Ferdinand, P. Comparison between non-destructive evaluation techniques and integrated fiber optic health monitoring systems for composite sandwich structures. *Journal of Intelligent Material Systems and Structures 11*, 6 (2000), 426–437.

[5] Barbezat, M., Birchmeier, M., Santschi, Y., and Brunner, A. J. Damage detection in fiber-reinforced laminates using impedance testing with piezoelectric active fiber composite elements. In *Proceedings of International Conference on Adaptive Structures and Technologies, ICAST* (Paris, France, 2005), M. Bernadou, J. Cagnol, and R. Ohayon, Eds., DEStech Publications, Inc., pp. 109–116.

[6] Barbezat, M., Brunner, A. J., Huber, C., and Flüeler, P. Integrated active ciber composite elements: Characterization for acoustic emission and acousto-ultrasonics. *Journal of Intelligent Material Systems and Structures 18*, 5 (2007), 515–525.

[7] Bathe, K.-J. *Finite element procedures*. Prentice-Hall International, London [etc.], 1996.

[8] Bendat, J. S., and Piersol, A. G. *Random Data: analysis and measurement procedures*. Wiley-Interscience, New York, 1971.

[9] Bent, A. A., and Hagood, N. W. Piezoelectric fiber composites with interdigitated electrodes. *Journal of Intelligent Material Systems and Structures 8*, 11 (1997), 903–919.

[10] Birchmeier, M., Brunner, A. J., Paradies, R., and Dual, J. Experimental characterization of active fiber composites used as piezoelectric transducers for emitting and receiving lamb waves in plate-like structures. In *Proceedings of International Conference on Advanced Technology in Experimental Mechanics 2007* (Fukuoka, Japan, 2007), JSME. paper no. OS17-2-2.

[11] Birchmeier, M., Brunner, A. J., Paradies, R., and Dual, J. Acitve fiber composites for exciting and sensing structural waves in plate-like structures. In *Proceedings of 4th European Workshop on Structural Health Monitoring* (Krakow, Poland, 2008), T. Uhl, W. Ostachowicz, and J. Holnicki-Szulc, Eds., DEStech Publications, Inc., pp. 422–429.

[12] Birchmeier, M., Gsell, D., Juon, M., Brunner, A. J., Paradies, R., and Dual, J. Active fiber composites for the generation of Lamb waves. *Ultrasonics 49*, 1 (2009), 73–82.

[13] Brunner, A. J., Barbezat, M., Huber, C., and Flueler, P. H. The potential of active fiber composites made from piezoelectric fibers for actuating and sensing applications in structural health monitoring. *Materials and Structures 38*, 279 (2005), 561–567.

[14] Brunner, A. J., Birchmeier, M., Melnykowycz, M. M., and Barbezat, M. Piezoelectric fiber composites as sensor elements for structural health monitoring and adaptive material systems. *Journal of Intelligent Material Systems and Structures 20*, 9 (2009), 1045–1055.

[15] Crawley, E. F., and de Luis, J. Use of piezoelectric actuators as elements of intelligent structures. *AIAA Journal 25*, 10 (1987), 1373–1385.

[16] Croxford, A. J., Wilcox, P. D., Drinkwater, B. W., and Konstantinidis, G. Strategies for guided-wave structural health monitoring. *Proceedings of the Royal Society A-Mathematical Physical and Engineering Sciences 463*, 2087 (2007), 2961–2981.

[17] Diamanti, K., Soutis, C., and Hodgkinson, J. M. Lamb waves for the non-destructive inspection of monolithic and sandwich composite beams. *Composites Part A-Applied Science and Manufacturing 36*, 2 (2005), 189–195.

[18] Farrar, C. R., and Worden, K. An introduction to structural health monitoring. *Philosophical Transactions of the Royal Society A-Mathematical Physical and Engineering Sciences 365*, 1851 (2007), 303–315.

[19] Fellinger, P., Marklein, R., Langenberg, K. J., and Klaholz, S. Numerical modeling of elastic-wave propagation and scattering with EFIT - elastodynamic finite integration technique. *Wave Motion 21*, 1 (1995), 47–66.

[20] Fromme, P. Defect detection in plates using guided waves. Diss. ETH No. 14397, ETH Zürich, 2001.

[21] Fromme, P. Health monitoring of plate structures using guided waves. In *Health Monitoring of Structural and Biological Systems 2008* (San Diego, California, USA, 2008), T. Kundu, Ed., vol. 6935, SPIE. paper no. 69350W-10.

[22] Fromme, P., and Sayir, M. B. Detection of cracks at rivet holes using guided waves. *Ultrasonics 40*, 1-8 (2002), 199–203.

[23] Giurgiutiu, V. Lamb wave generation with piezoelectric wafer active sensors for structural health monitoring. In *Smart Structures and Materials 2003: Smart Structures and Integrated Systems* (San Diego, CA, USA, 2003), A. M. Baz, Ed., vol. 5056, SPIE, pp. 111–122.

[24] Giurgiutiu, V., Bao, J., and Zhao, W. Piezoelectric wafer active sensor embedded ultrasonics in beams and plates. *Experimental Mechanics 43*, 4 (2003), 428–449.

[25] Giurgiutiu, V., and Zagrai, A. N. Characterization of piezoelectric wafer active sensors. *Journal of Intelligent Material Systems and Structures 11*, 12 (2000), 959–976.

[26] Giurgiutiu, V., and Zagrai, A. N. Embedded self-sensing piezoelectric active sensors for on-line structural identification. *Journal of Vibration and Acoustics-Transactions of the ASME 124*, 1 (2002), 116–125.

[27] Giurgiutiu, V., Zagrai, A. N., and Bao, J. Piezoelectric wafer embedded active sensors for aging aircraft structural health monitoring. *Structural Health Monitoring 1*, 1 (2002), 41–61.

[28] Greve, D. W., Neumann, J. J., Nieuwenhuis, J. H., Oppenheim, I. J., and Tyson, N. L. Use of Lamb waves to monitor plates: experiments and simulations. In *Smart Structures and Materials 2005: Sensors and Smart Structures Technologies for Civil, Mechanical, and Aerospace Systems* (San Diego, CA, USA, 2005), M. Tomizuka, Ed., vol. 5765, SPIE, pp. 281–292.

[29] Gsell, D. Nicht axialsymmetrische Wellenausbreitung in anisotropen zylindrischen Strukturen. Diss. ETH No. 14733, ETH Zürich, 2002.

[30] Gsell, D., Leutenegger, T., and Dual, J. Modeling three-dimensional elastic wave propagation in circular cylindrical structures using a finite-difference approach. *Journal of the Acoustical Society of America 116*, 6 (2004), 3284–3293.

[31] Harris, F. J. On the use of windows for harmonic analysis with the discrete Fourier transform. *Proceedings of the IEEE 66*, 1 (1978), 51–83.

[32] Hoffmann, R. *Grundlagen der Frequenzanalyse*, 2nd ed., vol. 620 of *Kontakt & Studium*. expert verlag, Renningen, Germany, 2005.

[33] Kehlenbach, M. Integrierte Sensorik zur Schädigungserkennung in Faserverbundstrukturen für die Luftfahrt. Diss. D 17, Technische Universität Darmstadt, 2003.

[34] Kessler, S. S., Spearing, S. M., and Soutis, C. Damage detection in composite materials using Lamb wave methods. *Smart Materials and Structures 11*, 2 (2002), 269–278.

[35] Kornmann, X., Huber, C., Barbezat, M., and Brunner, A. J. Active fiber composites: sensors and actuators for smart composites and structures. In *Proceedings of 11th European Conference on Composite Materials, ECCM-11* (Rhodes, Greece, 2004). paper no. B047.

[36] Kostek, S., and Randall, C. J. Modeling of a piezoelectric transducer and its application to full-wave-form acoustic logging. *Journal of the Acoustical Society of America 95*, 1 (1994), 109–122.

[37] Lamb, H. On waves in an elastic plate. *Proceedings of the Royal Society A-Mathematical Physical and Engineering Sciences 93* (1917), 114–128.

[38] Lanza di Scalea, F., Matt, H., and Bartoli, I. The response of rectangular piezoelectric sensors to Rayleigh and Lamb ultrasonic waves. *Journal of the Acoustical Society of America 121*, 1 (2007), 175–187.

[39] Lanza di Scalea, F., Matt, H., Bartoli, I., Coccia, S., Park, G., and Farrar, C. Health monitoring of UAV wing skin-to-spar joints using guided waves and macro fiber composite transducers. *Journal of Intelligent Material Systems and Structures 18*, 4 (2007), 373–388.

[40] Lee, B. C., and Staszewski, W. J. Modelling of Lamb waves for damage detection in metallic structures: Part I. wave propagation. *Smart Materials and Structures 12*, 5 (2003), 804–814.

[41] Lee, B. C., and Staszewski, W. J. Modelling of Lamb waves for damage detection in metallic structures: Part II. wave interactions with damage. *Smart Materials and Structures 12*, 5 (2003), 815–824.

[42] Lestari, W., and Qiao, P. Z. Damage detection of fiber-reinforced polymer honeycomb sandwich beams. *Composite Structures 67*, 3 (2005), 365–373.

[43] Leutenegger, T. Detection of defects in cylindrical structures using a time reverse numerical simulation method. Diss. ETH No. 14833, ETH Zürich, 2002.

[44] Liang, C., Sun, F. P., and Rogers, C. A. Coupled electro-mechanical analysis of adaptive material systems-determination of the actuator power consumption and system energy transfer. *Journal of Intelligent Material Systems and Structures 5* (1994), 12–20.

[45] Liu, T. R., Veidt, M., and Kitipornchai, S. Modelling the input-output behaviour of piezoelectric structural health monitoring systems for composite plates. *Smart Materials and Structures 12*, 5 (2003), 836–844.

[46] Martin, S. A., and Jata, K. V. Finite element simulation of Lamb wave generation with bonded piezoelectric transducers. In *Proceedings of 6th International Workshop on Structural Health Monitoring* (Stanford CA, USA, 2007), F.-K. Chan, Ed., DEStech Publications, Inc., pp. 841–850.

[47] Matt, H. M. Structural diagnostics of CFRP composite aircraft components by ultrasonic guided waves and built-in piezoelectric transducers. Los Alamos National Laboratory, PhD Thesis No. LA-14319-T, 2006.

[48] Matt, H. M., and Lanza di Scalea, F. Macro-fiber composite piezoelectric rosettes for acoustic source location in complex structures. *Smart Materials and Structures 16*, 4 (2007), 1489–1499.

[49] Melnykowycz, M., Kornmann, X., Huber, C., Barbezat, M., and Brunner, A. J. Performance of integrated active fiber composites in fiber reinforced epoxy laminates. *Smart Materials and Structures 15*, 1 (2006), 204–212.

[50] Monkhouse, R. S. C., Wilcox, P. D., and Cawley, P. Flexible interdigital PVDF transducers for the generation of Lamb waves in structures. *Ultrasonics 35* (1997), 489–498.

[51] Moulin, E., Assaad, J., Delebarre, C., and Osmont, D. Modeling of Lamb waves generated by integrated transducers in composite plates using a coupled finite element-normal modes expansion method. *Journal of the Acoustical Society of America 107*, 1 (2000), 87–94.

[52] Moulin, E., Grondel, S., Baouahi, M., and Assaad, J. Pseudo-3d modeling of a surface-bonded Lamb wave source (l). *Journal of the Acoustical Society of America 119*, 5 (2006), 2575–2578.

[53] Nagy, P. B., and Adler, L. Nondestructive evaluation of adhesive joints by guided-waves. *Journal of Applied Physics 66*, 10 (1989), 4658–4663.

[54] Nieuwenhuis, J. H., Neumann, J. J., J., Greve, D. W., and Oppenheim, I. J. Generation and detection of guided waves using pzt wafer transducers. *IEEE Transactions on Ultrasonics, Ferroelectrics and Frequency Control 52*, 11 (2005), 2103–2111.

[55] Nitzsche, F., Müller, M.-A., and Paradies, R. Characterization of active fiber composites for sensor applications. In *Proceedings of 17th International Conference on Adaptive Structures and Technologies* (Taipei, Taiwan, 2006), pp. 246–256.

[56] Paradies, R., and Melnykowycz, M. Numerical stress investigation for piezoelectric elements with a circular cross section and interdigitated electrodes. *Journal of Intelligent Material Systems and Structures 18*, 9 (2007), 963–972.

[57] Park, G., Cudney, H. H., and Inman, D. J. Impedance-based health monitoring technique for massive structures and high-temperature structures. In *Smart Structures and Materials 1999 Conference* (Newport Beach, CA, 1999), R. O. Claus and W. B. Spillman, Eds., pp. 461–469.

[58] Park, G., Farrar, C. R., Lanza di Scalea, F., and Coccia, S. Performance assessment and validation of piezoelectric active-sensors in structural health monitoring. *Smart Materials and Structures 15*, 6 (2006), 1673–1683.

[59] Park, G., Kabeya, K., Cudney, H. H., and Inman, D. J. Impedance-based structural health monitoring for temperature varying applications. *JSME International Journal Series A-Solid Mechanics and Material Engineering 42*, 2 (1999), 249–258.

[60] Park, G., Sohn, H., Farrar, C. R., and Inman, D. J. Overview of piezoelectric impedance-based health monitoring and path forward. *The Shock and Vibration Digest 35*, 6 (2003), 451–463.

[61] Peairs, D. M., Park, G., and Inman, D. J. Simplified modeling for impedance-based health monitoring. *Key Engineering Materials 293-294* (2005), 643–650.

[62] Raghavan, A., and Cesnik, C. E. S. Modeling of piezoelectric-based Lamb wave generation and sensing for structural health monitoring. In *Smart Structures and Materials 2004: Sensors and Smart Structures Technologies for Civil, Mechanical, and Aerospace Systems* (San Diego, CA, USA, 2004), vol. 5391, SPIE, pp. 419–430.

[63] Raghavan, A., and Cesnik, C. E. S. Finite-dimensional piezoelectric transducer modeling for guided wave based structural health monitoring. *Smart Materials and Structures 14*, 6 (2005), 1448–1461.

[64] Raghavan, A., and Cesnik, C. E. S. 3-d elasticity-based modeling of anisotropic piezocomposite transducers for guided wave structural health monitoring. *Journal of Vibration and Acoustics-Transactions of the ASME 129*, 6 (2007), 739–751.

[65] Ricon, Y. G. U., Segovia, F. J. C., and de Espinosa Freijo, F. M. Lamb waves generation on thin plates using piezocomposites. *Journal of the European Ceramic Society 27*, 13-15 (2007), 4147–4151.

[66] Ristic, V. M. *Principles of acoustic devices.* Wiley, New York, 1983.

[67] Rose, J. L. *Ultrasonic waves in solid media.* Cambridge University Press, Cambridge, UK, 1999.

[68] Rose, J. L. Guided wave nuances for ultrasonic nondestructive evaluation. *IEEE Transactions on Ultrasonics, Ferroelectrics and Frequency Control 47*, 3 (2000), 575–583.

[69] Rose, L. R. F., and Wang, C. H. Mindlin plate theory for damage detection: Source solutions. *Journal of the Acoustical Society of America 116*, 1 (2004), 154–171.

[70] Salas, K. I., and Cesnik, C. E. S. Design and characterization of the CLoVER transducer for structural health monitoring. In *Proceedings of 4th European Workshop on Structural Health Monitoring* (Krakow, Poland, 2008), T. Uhl, W. Ostachowicz, and J. Holnicki-Szulc, Eds., DEStech Publications, Inc., pp. 447–454.

[71] Schubert, F. Numerical time-domain modeling of linear and nonlinear ultrasonic wave propagation using finite integration techniques – theory and applications. *Ultrasonics 42* (2004), 221–229.

[72] Schulz, M. J., Sundaresan, M. J., Ghoshal, A., and Pai, P. F. Active fiber composites for structural health monitoring. In *Smart Structures and Materials 2000: Active Materials: Behavior and Mechanics* (Newport Beach, CA, USA, 2000), vol. 3992, SPIE, pp. 13–24.

[73] Sodano, H. A., Park, G., and Inman, D. J. An investigation into the performance of macro-fiber composites for sensing and structural vibration applications. *Mechanical Systems and Signal Processing 18*, 3 (2004), 683–697.

[74] Staszewski, W. J., Boller, C., and Tomlinson, G. R., Eds. *Health monitoring of aerospace structures: Smart sensor technologies and signal processing.* John Wiley & Sons, Ltd, Chichester, 2004.

[75] Staszewski, W. J., Lee, B. C., Mallet, L., and Scarpa, F. Structural health monitoring using scanning laser vibrometry: I. Lamb wave sensing. *Smart Materials and Structures 13*, 2 (2004), 251–260.

[76] Staszewski, W. J., Lee, B. C., and Traynor, R. Fatigue crack detection in metallic structures with Lamb waves and 3D laser vibrometry. *Measurement Science and Technology 18*, 3 (2007), 727–739.

[77] Su, Z. Q., Ye, L., and Lu, Y. Guided Lamb waves for identification of damage in composite structures: A review. *Journal of Sound and Vibration 295*, 3-5 (2006), 753–780.

[78] Sun, F. P., Chaudhry, Z., Liang, C., and Rogers, C. A. Truss structure integrity identification using PZT sensor-actuator. *Journal of Intelligent Material Systems and Structures 6* (1995), 134–139.

[79] Thien, A. B., Chiamori, H. C., Ching, J. T., Wait, J. R., and Park, G. The use of macro-fibre composites for pipeline structural health assessment. *Structural Control and Health Monitoring 15* (2008), 43–63.

[80] Tressler, J. F., Alkoy, S., and Newnham, R. E. Piezoelectric sensors and sensor materials. *Journal of Electroceramics 2*, 4 (1998), 257–272.

[81] Veidt, M., Liu, T. R., and Kitipornchai, S. Experimental investigation of the acousto-ultrasonic transfer characteristics of adhesively bonded piezoceramic transducers. *Smart Materials and Structures 9*, 1 (2000), 19–23.

[82] Veidt, M., Liu, T. R., and Kitipornchai, S. Flexural waves transmitted by rectangular piezoceramic transducers. *Smart Materials and Structures 10*, 4 (2001), 681–688.

[83] Viktorov, I. A. *Rayleigh and Lamb waves.* Plenum, New York, 1967.

[84] Wait, J. R., Park, G., Sohn, H., and Farrar, C. R. Plate damage identification using wave propagation and impedance methods. In *Conference on Health Monitoring and Smart Nondestructive Evaluation of Structural and Biological Systems III* (San Diego, CA, USA, 2004), T. Kundu, Ed., vol. 5394, SPIE, pp. 53–65.

[85] Wilcox, P. D., Dalton, R. P., Lowe, M. J. S., and Cawley, P. Mode and transducer selection for long range lamb wave inspection. In *3rd International Conference on Damage Assessment of Structures (DAMAS 99)* (Dublin, Ireland, 1999), M. D. Gilchrist, J. M. DulieuBarton, and K. Worden, Eds., pp. 152–161.

[86] Wilcox, P. D., Lowe, M., and Cawley, P. The effect of dispersion on long-range inspection using ultrasonic guided waves. *NDT&E International 34*, 1 (2001), 1–9.

[87] Wilkie, W. K., Bryant, R. G., High, J. W., Fox, R. L., Hellbaum, R. F., Jalink, J. A., Little, B. D., and Mirick, P. H. Low-cost piezocomposite actuator for structural control applications. In *Smart Structures and Materials 2000: Industrial and Commercial Applications of Smart Structures Technologies* (Newport Beach, CA, USA, 2000), vol. 3991, SPIE, pp. 323–334.

[88] Worden, K., Farrar, C. R., Manson, G., and Park, G. The fundamental axioms of structural health monitoring. *Proceedings of the Royal Society A-Mathematical Physical and Engineering Sciences 463*, 2082 (2007), 1639–1664.

[89] Worlton, D. C. Experimental confirmation of lamb waves at megacycle frequencies. *Journal of Applied Physics 32*, 6 (1961), 967–971.

[90] Yang, M. J., and Qiao, P. Z. Modeling and experimental detection of damage in various materials using the pulse-echo method and piezoelectric sensors/actuators. *Smart Materials and Structures 14*, 6 (2005), 1083–1100.

Curriculum Vitae

Marcel Birchmeier

Born on June 14, 1976 in Rüti/ZH, Switzerland
Citizen of Rapperswil/SG, Switzerland

Education

2005 - 2009	Doctoral studies at the Laboratory of Mechanical Systems Engineering of the Empa Dübendorf and at the Institute of Mechanical Systems of the ETH Zürich
1998 - 2003	Studies at the Department of Civil, Environmental and Geomatic Engineering of the ETH Zürich Graduation with the degree Dipl. Bau.-Ing. ETH
1991 - 1996	Kantonsschule Pfäffikon/SZ, Switzerland Graduation with a matura, type C
1989 - 1991	Sekundarschule Rapperswil/SG
1983 - 1989	Primarschule Rapperswil/SG

Practical experience

2006 - 2007	Institute of Mechanical Systems of the ETH Zürich, teaching assistance
Okt. - Dec. 2004	Ingenieurbüro für Verkehrsplanung IBV Hüsler AG, Zürich, temporary employment
2000 - 2003	Institute of Mechanical Systems of the ETH Zürich, tutorial assistance
1999 - 2005	Credit Suisse, Zürich, Supply Management, part-time employment

List of Publications

Barbezat, M., Birchmeier, M., Santschi, Y., and Brunner, A. J. Damage detection in fiber-reinforced laminates using impedance testing with piezoelectric active fiber composite elements. In *Proceedings of International Conference on Adaptive Structures and Technologies, ICAST* (Paris, France, 2005), M. Bernadou, J. Cagnol, and R. Ohayon, Eds., DEStech Publications, Inc., pp. 109–116.

Birchmeier, M., Brunner, A. J., Paradies, R., and Dual, J. Active fiber composites as orthotropic piezoelectric transducers for structural health monitoring applications: experimental approach. In *Proceedings of 9th Cansmart Meeting - International Workshop on Smart Materials and Structures* (Toronto, Ontario, Canada, 2006), G. Akhras, Ed., pp. 203–212.

Brunner, A. J., Birchmeier, M., and Barbezat, M. Piezoelectric active fiber composites as acoustic emission sensors for structural integrity monitoring of adaptive material systems. In *Proceedings of 6th International Symposium on Advanced Acoustic Emission and Ultrasonic and/of New Materials* (Shibuya, Tokyo, Japan, 2006), AAUM, pp. 25–32.

Birchmeier, M., Brunner, A. J., Paradies, R., and Dual, J. Experimental characterization of active fiber composites used as piezoelectric transducers for emitting and receiving Lamb waves in plate-like structures. In *Proceedings of International Conference on Advanced Technology in Experimental Mechanics 2007* (Fukuoka, Japan, 2007). JSME. paper no. OS17-2-2.

Birchmeier, M., Brunner, A. J., Paradies, R., and Dual, J. Acitve fiber composites for exciting and sensing structural waves in plate-like structures. In *Proceedings of 4th European Workshop on Structural Health Monitoring* (Krakow, Poland, 2008), T. Uhl, W. Ostachowicz, and J. Holnicki-Szulc, Eds., DEStech Publications, Inc., pp. 422–429.

Birchmeier, M., Gsell, D., Juon, M., Brunner, A. J., Paradies, R., and Dual, J. Active fiber composites for the generation of Lamb waves. *Ultrasonics 49*, 1 (2009), 73–82.

Brunner, A. J., Birchmeier, M., Melnykowycz, M. M., and Barbezat, M. Piezoelectric fiber composites as sensor elements for structural health monitoring and adaptive material systems. Journal of Intelligent Material Systems and Structures 20, 9 (2009), 1045–1055.

Birchmeier, M., Brunner, A. J., and Dual, J. Characterization of active fiber composites as emitter and receiver of elastic waves in plates. Journal publication, in preparation.

Birchmeier, M., Brunner, A. J., and Dual, J. Active fiber composites for damage detection in sandwich plates with wave and vibration based methods. Journal publication, in preparation.